Precision irrigation management through thermal and multispectral remote sensing: An integration of sensing systems and analytical techniques

by

Manoj Gadhwal

B.S., Punjab Agricultural University, India, 2016
M.S., Punjab Agricultural University, India, 2018

AN ABSTRACT OF A DISSERTATION

submitted in partial fulfillment of the requirements for the degree

DOCTOR OF PHILOSOPHY

Carl and Melinda Helwig Department of Biological and Agricultural Engineering
Carl R. Ice College of Engineering

KANSAS STATE UNIVERSITY
Manhattan, Kansas

2023

Abstract

Irrigation water management starts with quantifying irrigation prescriptions based on crop water requirements at a spatial scale. For determining the water requirement of the plants, canopy temperature-dependent crop water stress could provide a potential solution. The use of a small unmanned aerial system (sUAS) with a thermal infrared (TIR) camera has long been established as an effective method of measuring plant canopy temperatures at a spatial scale. However, concerns still exist about the accuracy of these systems in collecting canopy temperatures and estimating crop water stress. The overall goal of this research is to assess high spatial resolution crop water stress in a corn field and evaluate UAS-based thermal imagery's capacity to provide precise canopy temperature. As a part of this study, the capacity and feasibility of UAV-based imagery to detect infield crop health variability were also evaluated against aircraft and satellite imagery.

To analyze the effects of flying altitude and camera view angle on thermal infrared imagery, thermal cameras with different focal lengths (9 mm, 13 mm, and 19 mm) were flown at different altitudes (30 m, 50 m, and 70 m). The orthomosaics generated from images were examined for the accuracy of the corn-canopy temperature sensing, ability to differentiate between hot and cold surfaces, ease of image stitching, geometric accuracy, image quality, and spatial resolution. The results indicated that a canopy temperature map of crops with a temperature error of less than 2° C from the actual canopy temperature can be produced with the combination of appropriate camera focal length, altitude, and image calibration techniques. A narrow-angle thermal camera flying at low altitudes (<50 m) was found to be the least suitable combination for corn canopy temperature sensing. The most appropriate combination for temperature estimation

of corn canopies was with a 13 mm focal length camera flying at an altitude of 50 m above ground level.

To quantify corn's crop water stress index (CWSI), images were collected using a thermal camera and a multispectral camera mounted on a Matrice 100 sUAS, over a four acres corn field divided into three irrigation levels (50%, 75%, and 100% irrigation level). Field-specific water stress baselines were developed and used in CWSI quantification to consider the effect of the instant local environment. High-resolution precise crop water stress maps developed from thermal images were capable of inter-row and intra-row detection of corn water stress. The vegetative indices significantly explained variation in crop water stress, with NDRE (Normalized Difference Red Edge index) having the highest R^2 value of 0.8 and NDVI (Normalized Difference Vegetation Index) having an R^2 value of 0.7. Field-measured leaf water potential also significantly affected water stress but showed a weaker correlation with R^2 values of 0.6. Overall results from this study showed that the combination of thermal imaging and NIR imaging could be utilized to determine accurate crop water stress on the spatial scale for irrigation water management and scheduling.

A comparative assessment of UAS (Matrice-100), aircraft (Ceres Imaging), and satellite (Landsat-8) imagery to detect infield crop health variability for the implementation of a precision irrigation system was also accomplished. Spatial maps of canopy temperature and NDVI were developed using the images from different imaging platforms and analyzed for capacity to capture water requirements and crop health accurately. UAV imagery outperformed the other two platforms by providing the highest number of pixels and variations in temperatures and NDVI values to represent a given target area. Moderate and low spatial resolution imagery from aircraft (1-1.5 m/pixel) and satellite (30 m/pixel) was limited in detecting inter-row variability and outputting the average pixels of the crop canopy and inter-row space. Whereas high-resolution

UAV imagery (1.5 cm/pixel – 6 cm/pixel) precisely distinguished inter-row gap from plants and provided crop-only pixels without mixing with background soil. UAV imagery and aircraft imagery remains competitive in detecting crop variability between two nozzles of an irrigation pivot. UAV imagery was much more sensitive and precise in detecting minute changes as compared to other platforms. Satellite imagery was limited in capturing the variations at this small scale.

In summary, this study provided an appropriate combination of camera focal length and flying altitude to accurately and efficiently estimate canopy temperature and crop water stress in corn. Methods were developed to precisely detect inter and intra-row crop water stress and health variability using low-altitude high-resolution UAV imagery. Detailed insight into the capacity of different remote sensing platforms was provided to detect crop health variability in small-scale farms and implement crop irrigation management based on crop canopy temperatures.

Precision irrigation management through thermal and multispectral remote sensing: An integration of sensing systems and analytical techniques

by

Manoj Gadhwal

B.S., Punjab Agricultural University, India, 2016
M.S., Punjab Agricultural University, India, 2018

A DISSERTATION

submitted in partial fulfillment of the requirements for the degree

DOCTOR OF PHILOSOPHY

Carl and Melinda Helwig Department of Biological and Agricultural Engineering
Carl R. Ice College of Engineering

KANSAS STATE UNIVERSITY
Manhattan, Kansas

2023

Approved by:

Major Professor
Dr. Ajay Sharda

Copyright

Abstract

Irrigation water management starts with quantifying irrigation prescriptions based on crop water requirements at a spatial scale. For determining the water requirement of the plants, canopy temperature-dependent crop water stress could provide a potential solution. The use of a small unmanned aerial system (sUAS) with a thermal infrared (TIR) camera has long been established as an effective method of measuring plant canopy temperatures at a spatial scale. However, concerns still exist about the accuracy of these systems in collecting canopy temperatures and estimating crop water stress. The overall goal of this research is to assess high spatial resolution crop water stress in a corn field and evaluate UAS-based thermal imagery's capacity to provide precise canopy temperature. As a part of this study, the capacity and feasibility of UAV-based imagery to detect infield crop health variability were also evaluated against aircraft and satellite imagery.

To analyze the effects of flying altitude and camera view angle on thermal infrared imagery, thermal cameras with different focal lengths (9 mm, 13 mm, and 19 mm) were flown at different altitudes (30 m, 50 m, and 70 m). The orthomosaics generated from images were examined for the accuracy of the corn-canopy temperature sensing, ability to differentiate between hot and cold surfaces, ease of image stitching, geometric accuracy, image quality, and spatial resolution. The results indicated that a canopy temperature map of crops with a temperature error of less than 2° C from the actual canopy temperature can be produced with the combination of appropriate camera focal length, altitude, and image calibration techniques. A narrow-angle thermal camera flying at low altitudes (<50 m) was found to be the least suitable combination for corn canopy temperature sensing. The most appropriate combination for temperature estimation

of corn canopies was with a 13 mm focal length camera flying at an altitude of 50 m above ground level.

To quantify corn's crop water stress index (CWSI), images were collected using a thermal camera and a multispectral camera mounted on a Matrice 100 sUAS, over a four acres corn field divided into three irrigation levels (50%, 75%, and 100% irrigation level). Field-specific water stress baselines were developed and used in CWSI quantification to consider the effect of the instant local environment. High-resolution precise crop water stress maps developed from thermal images were capable of inter-row and intra-row detection of corn water stress. The vegetative indices significantly explained variation in crop water stress, with NDRE (Normalized Difference Red Edge index) having the highest R^2 value of 0.8 and NDVI (Normalized Difference Vegetation Index) having an R^2 value of 0.7. Field-measured leaf water potential also significantly affected water stress but showed a weaker correlation with R^2 values of 0.6. Overall results from this study showed that the combination of thermal imaging and NIR imaging could be utilized to determine accurate crop water stress on the spatial scale for irrigation water management and scheduling.

A comparative assessment of UAS (Matrice-100), aircraft (Ceres Imaging), and satellite (Landsat-8) imagery to detect infield crop health variability for the implementation of a precision irrigation system was also accomplished. Spatial maps of canopy temperature and NDVI were developed using the images from different imaging platforms and analyzed for capacity to capture water requirements and crop health accurately. UAV imagery outperformed the other two platforms by providing the highest number of pixels and variations in temperatures and NDVI values to represent a given target area. Moderate and low spatial resolution imagery from aircraft (1-1.5 m/pixel) and satellite (30 m/pixel) was limited in detecting inter-row variability and outputting the average pixels of the crop canopy and inter-row space. Whereas high-resolution

UAV imagery (1.5 cm/pixel – 6 cm/pixel) precisely distinguished inter-row gap from plants and provided crop-only pixels without mixing with background soil. UAV imagery and aircraft imagery remains competitive in detecting crop variability between two nozzles of an irrigation pivot. UAV imagery was much more sensitive and precise in detecting minute changes as compared to other platforms. Satellite imagery was limited in capturing the variations at this small scale.

In summary, this study provided an appropriate combination of camera focal length and flying altitude to accurately and efficiently estimate canopy temperature and crop water stress in corn. Methods were developed to precisely detect inter and intra-row crop water stress and health variability using low-altitude high-resolution UAV imagery. Detailed insight into the capacity of different remote sensing platforms was provided to detect crop health variability in small-scale farms and implement crop irrigation management based on crop canopy temperatures.

Table of Contents

List of Figures

List of Tables

Acknowledgements

I am incredibly grateful to my major professor, Dr. Ajay Sharda, for believing in me and providing me with the opportunity to pursue my doctoral degree under his mentorship. His invaluable guidance and unwavering support have been instrumental in shaping my personal and professional growth, leading me to achieve this significant milestone.

I extend my heartfelt thanks to my supervisory committee members, Dr. Deon van der Merwe, Dr. J.M. Shawn Hutchinson, Dr. Ignacio A. Ciampitti, and Dr. Krishna Jagadish, for their generous time, valuable suggestions, and constant encouragement throughout my PhD journey. I am grateful to all the faculty and staff members of the Department of Biological and Agricultural Engineering, especially Arlene Jacobson, and Jamie Boeckman, for their support.

I sincerely appreciate the support of Prashanta Pokharel, Ketan Shende, Harman Sangha, Rahul Singh, Sylvester Badua, and John Eric during my field experiments, which greatly contributed to the success of my research. To my dear friends, Pardeep, Kanwal, Vishal, Manraj, Abhilekha, Gaganpreet, and Sevendeep, thank you for your continuous kindness and love, supporting me through the highs and lows of this journey.

Lastly, my heartfelt thanks go to my family - my father, mother, and brother - for their unwavering motivation and endless support in pursuing higher education. Their unconditional love and sacrifices have been my guiding light, and I am truly blessed to have them in my life.

In conclusion, I offer my profound gratitude to everyone who has contributed to my success, and I acknowledge the blessings from God that have made this journey possible.

Dedication

I dedicate this work to

my parents Karan Singh Gadhwal and Imrata Devi,

my brother Pawan Kumar Gadhwal,

my motherland Chobara, Haryana, India.

Chapter 1 - Introduction

1.1 Irrigation Management

Water is the most valuable and indispensable resource present on earth. The scarcity of water resources for irrigation poses a significant challenge in agriculture, particularly in arid and semi-arid regions. Agriculture consumes 80–90% of the freshwater available worldwide, about two-thirds of which is used for crop irrigation [Fereres & Evans, 2006; Gerhards *et al.*, 2019]. In the United States alone, 83.4 million acre-feet of water are consumed on irrigated acres annually, with corn being the crop with a maximum share of 25 % of total U.S. irrigated acres [Farm and Ranch Irrigation Survey (FRIS), 2018]. As climate change aggravates droughts and produces a risk to future water resources, it becomes imperative to use each unit of applied irrigation water for maximum production. In such conditions, the most promising solution for the sustainable management of agricultural water resources is improving agricultural water productivity. On-farm

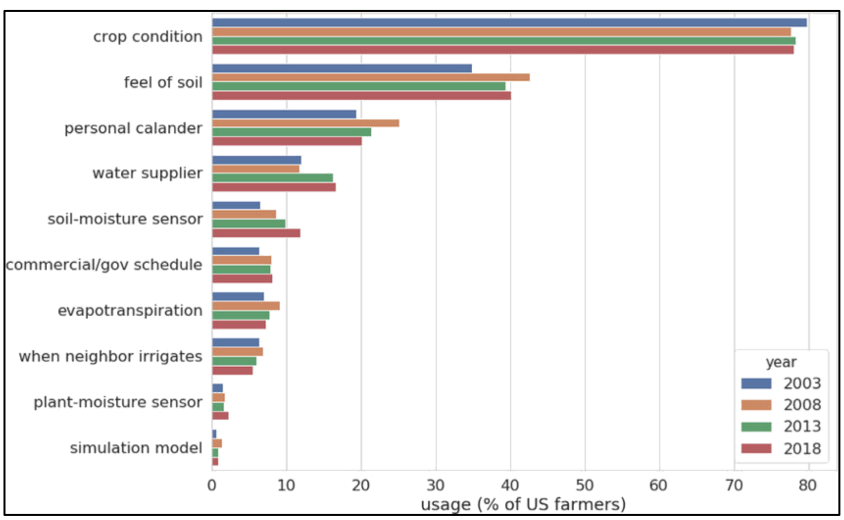

Figure 1.1. Irrigation-decision making methods from Farm and Ranch Irrigation Survey (FRIS) 2018

variable rate irrigation (VRI) technologies exist nowadays but need more implementation. The USDA's Farm and Ranch Irrigation Survey (FRIS) 2018 (Figure 1.1) reported that most US farmers apply irrigation based on crop conditions and soil feel. Less than 15 % use moisture-sensing devices to provide the exact required water. The key objective of VRI, "more crop per drop," cannot be accomplished without a thorough knowledge of crop water status to determine appropriate irrigation rates and timing. Crop water status information over a large farmland area has great potential for optimizing agricultural water use. Quantifying plant water needs through monitoring spatial crop water stress allows the deployment of a site-specific irrigation system that can provide the exact amount of water required by plants [Shi *et al.*, 2016].

1.2 Crop water stress and canopy temperature connection

Crop water stress (CWS) induces by water shortage in plants either due to soil moisture deficit or high environmental demands [Gerhards *et al.*, 2019]. CWS causes a decrease in photosynthesis activity, stomatal conductance, leaf water content, transpiration, and leaf expansion. Based on these characteristics, CWS can be detected by measuring soil moisture content and crop physiological characteristics (e.g., stomatal conductance, leaf water potential, canopy temperature, and photosynthesis activity) [Zhang *et al.*, 2019b]. Out of all the physiological characteristics, canopy temperature is the most important and widely accepted indicator of CWS [Awais *et al*., 2022; Peñuelas *et al*., 1993]. Canopy temperature is a relatively quick-response characteristic that does not depend on plant structure or pigment changes, which take more time to develop [Khanal *et al.*, 2017]. Leaf temperature is strongly correlated to stomatal control of leaves, leaf loses water through stomata openings during transpiration, causing a drop in leaf temperature [Idso *et al.*, 1981; Jones 1999; Jones *et al*. 2002]. So, if stomatal closure happens, it will increase the canopy temperature as there will be no heat dissipation through evaporation. A healthy and transpiring leaf's temperature should be similar to the air temperature, while stressed leaves exhibit a higher temperature [Giménez *et al*.,2021; Jones *et al*., 2014; Zhang *et al*., 2019a]. So, plants react to water stress by increasing leaf temperature and closing stomatal openings. It is for this reason that canopy temperature has become the most accepted and reliable tool for estimating plant water requirements [Awais *et al*., 2022].

1.3 Crop water stress assessment

Quantifying water stress using canopy temperature requires consideration of a few environmental variables that create high environmental demands and affect leaf stomata openings. These variables include air temperature (Ta), relative humidity (RH), vapor pressure deficit (VPD), solar radiation, and wind speed. Several canopy temperature-based indices have been used to monitor spatial crop water stress like, apparent thermal inertia (ATI), crop water stress index (CWSI) [Idso *et al*., 1981, Jackson *et al.*, 1981], degrees above non-stressed (DANS), degrees above canopy threshold (DACT), time temperature threshold (TTT), integrated DANS (IDANS), and integrated DACT (IDACT) [DeJonge *et al.*, 2015]. Of these indices, CWSI is the most commonly used index and there is a substantial correlation observed between CWSI and ground-based water stress indicators [Moller *et al.*, 2006; Taghvaeian *et al*., 2012; Bellvert *et al*., 2014; Gonzalez-Dugo *et al*., 2014; Pou *et al*., 2014; Taghvaeian *et al.*, 2014; DeJonge *et al*., 2015].

CWSI calculation is based on estimation of two baselines: the lower limit of the air-canopy temperature difference (non-water-stressed baseline, NWSB), which represents healthy plants, and the upper limit, which represents highly stressed plants [Awais *et al*., 2022]. These baselines can be calculated by two approaches: theoretical [Jackson *et al*., 1981] or empirical method [Idso *et al*., 1981]. The empirical method is preferred over the theoretical, as it uses only three variables (Ta, RH, and VPD), making it easier to implement. A linear relationship between the canopy-air temperature difference of healthy plants and atmospheric VPD is used as the NWSB. A constant value of canopy-air temperature difference representing stressed plants can be used as the dry reference or upper limit, which can vary from 4 ^{0}C to 10 ^{0}C, [Alves & Pereira, 2000; Cohen *et al*., 2005; Erdem *et al*., 2010; Moller *et al*. 2006; Wanjura *et al*., 2006]. NWSBs are crop and climate specific, so it becomes crucial to develop exclusive baselines when the crop or environmental conditions change. Once baselines are available, obtaining concurrent air temperature and relative humidity measurements, one can use canopy temperature to estimate CWSI. Several studies have been conducted to estimate CWSI for different types of crops like cotton [Cohen *et al*., 2015], grapevine [Bellvert *et al*., 2015, Pou *et al*., 2014, Zarco-Tejada *et al*., 2013], soybean [Crusiol *et al*., 2020], olives [Berni *et al*., 2009] apple tree [Gómez-Candón *et al*., 2016]. Using the baseline approach CWS has been estimated for Corn as well [Kar & Kumar, 2010; Payero & Irmak, 2006; Li *et al.*, 2010; Chen *et al.*, 2010; Irmak *et al.*, 2000; Zia *et al.*, 2013; Zhang *et al.*, 2023; Brewer *et al.*, 2022; DeJonge *et al.*, 2015; Zhang *et al.*, 2019b].

1.4 Canopy temperature sensing

To quantify the in-field variability of plant traits, numerous tools and techniques have been used in the past. Traditional methods of on-site/ground measurements are time-consuming, laborious, and costly. They omit the spatial variability of soil and crops, so they are not suitable for time-specific and continuous field-scale monitoring of plant traits [Bosecker 1988; Comba *et al*., 2020; Han *et al*., 2021, Ndlovu *et al*., 2021; Ziliani *et al.*, 2018]. Canopy temperature can be sensed using infrared radiometers on the ground or thermal infrared remote sensing. Remote sensing-based canopy temperature measurements have the advantages of being accessible, non-destructive, having low labor intensity, and considering spatial variability. [Berger *et al*., 2020; Campos-Taberner *et al*., 2018; G. Poley & J. McDermid, 2020; Li *et al.*, 2022; Ten Harkel *et al*., 2019].

The imaging sensors mounted on remote sensing platforms receive majority of incoming electromagnetic energy from target surfaces. This is in the form of reflected light, usually in the visible (VIS) and near infrared (NIR) wavelength ranges. Incoming energy can also be due to backscattered light from atmospheric components, or emitted light (including thermal infrared and fluorescent light) [Metternicht, G., 2008]. Different plant characteristics can be determined using specific wavelength regions of received electromagnetic energy. For example, rate of photosynthesis or leaf chlorophyll content can be estimated from fluorescence (683 nm and 740 nm) using hyperspectral bands. Customized cameras that detect two or more bands {example: red (630 nm-690 nm) and NIR (770 nm-900 nm)} can be used to determine an index that is correlated with leaf area, wilting stage, canopy structure, or canopy coverage. Thermal infrared {TIR (7500 nm – 13500 nm)} imaging can be used to quantify crop canopy temperature. Thermal infrared (TIR) imaging can quantify canopy temperatures using different remote sensing platforms. It is significantly affected by the altitudes and atmosphere between the imaging sensor and the target objects.

1.5 Canopy temperature sensing constraints and remote sensing platforms

Canopy temperature-based quantification of water requirements has been a significant application of remote sensing in agriculture and has been extensively explored using satellites [Hussain *et al*., 2020; Krishna *et al*., 2021; Ndlovu *et al*., 2021; Sibanda *et al*., 2021; Xu *et al*., 2020] and UAVs [Jaganmohan *et al*., 2016; Kang *et al*., 2018; Yang *et al*., 2017]. Remote sensing in agriculture is majorly influenced by platform altitude, spatial resolution, and the frequency and time-precision of revisiting an area (temporal resolution) [Metternicht, G., 2008; Messina *et al*., 2020]. Spatial resolution dictates the smallest object/area to be detected in imagery; thus, the key indicator of the level of detail in images. As spatial resolution drops, plant and background soil heterogeneity in a single pixel increases, leading to less precise measurements of crop traits [Mulla, 2013]. There are three main remote sensing platforms: unmanned aerial vehicles (UAVs), aircraft, and satellites, which cover most of the spatial resolutions and altitudes used in agriculture. Each remote sensing platform has its benefits and limitation from a technical and operational point of view.

Satellite imagery is susceptible to degradation by atmospheric factors. These factors include light absorption, scatter by clouds, variations in various particulates, aerosols, gasses, and temperatures that reduce the availability and consistency of satellite imagery. Another downside of satellite imagery is the fixed time acquisition, which can result in missing crucial crop phenological stages or specific time windows [Barzin *et al*., 2020; Gevaert *et al.*, 2015]. For instance, commonly used platforms like Sentinel (revisit time of 2-5 days) and Landsat8 (revisit time of 16 days) are limited in their ability to provide frequent agricultural assessments due to this constraint. Despite these limitations, the continuous advancements in satellite technology have opened up new possibilities. Some satellite platforms now offer daily coverage of target regions, which effectively addresses the problem of infrequent data collection. Notable examples of such satellites include Planet's Dove Constellation, Super View Constellation, Rapid Eye, and Satellogic. These advancements in satellite capabilities can play a very crucial role in agricultural monitoring, allowing for more informed and timely decision-making processes. Satellite imagery's benefits include large area mapping in a single drive, easy to access and free of cost (several but not all) available data, heavy payload capacity, and no constraint on flight duration [Li *et al.*, 2022].

However, UAV imagery provides elasticity in operations; users can perform multitemporal and custom-defined campaigns. Low-altitude UAV flights are easy and safer to conduct, provide a very high spatial resolution of centimeters level and avoid the majority of atmospheric interferences and clouds [Han *et al*., 2021; White *et al*., 2012; Zarco-Tejada *et al.*, 2013]. UAVs have widespread implementation and are suitable for small farms but have weaknesses like limited payload capacity, short flight duration, technical complexity (complex flight operations, image analysis, and data processing), and little spatial coverage. Aircraft imagery serves as a valuable intermediary between satellite and UAV imagery, offering advantages in terms of spatial coverage compared to UAVs and reduced atmospheric hindrances compared to satellites due to its closer proximity to crops during flight. This results in higher spatial resolution and more detailed imagery compared to satellites.

The aircraft surveys can be executed efficiently compared to the other platforms, allowing for rapid data collection over large areas. However, it comes with higher costs and demands complex campaign organization efforts. Despite the advantages, aircraft surveys may still miss some fine-scale details [Matese *et al*., 2015] that can be captured by lower-altitude UAVs, making it essential to carefully consider the trade-offs and specific requirements of each application when choosing the appropriate imaging platform.

The satellite imagery, limited by atmospheric effects and low spatial resolution, can only provide very few and homogenous temperature measurements throughout the field. While, UAV-based TIR imaging can precisely distinguish the surface temperature features due to its high spatial resolution and very low altitude (20 to 100 m) flight closer to the crop, diminishing the weather effects [Webster *et al.*, 2018]. A comparative analysis of different remote sensing platforms for canopy temperature sensing from an irrigation point of view still needs exploration.

UAV-based thermal remote sensing approach serves as a routine tool for monitoring plants' canopy temperatures, however, concerns still exist on accuracy of canopy temperatures collected by UAV systems and data extracted from imagery. An important concern for data extraction from thermal imagery is the need to separate pure crop canopy pixels from soil background. Thermal image processing is limited due to the low resolution of thermal cameras (from 320 × 240 to 640 × 480 pixels). It is often difficult to effectively separate soil pixels from crop pixels in thermal images, causing significant bias in Tc measurements. The most common method for excluding background pixels is using thermal imagery with RGB and multispectral imagery together, called the co-registration approach [Sagan *et al*., 2019; Zhang, L. *et al*., 2019; Zhang, Y. *et al.,* 2023]. Crop pixels can be separated in RGB or NIR imagery using different classification algorithms, and then co-registered with thermal imagery to extract canopy-only temperature values. Several scientists have also explored approaches which only use thermal imagery to extract pure canopy pixels, using edge detection algorithms [Bian *et al.* 2019; Ludovisi *et al.,* 2017; Meron *et al.,* 2013; Zhang, Z. *et al.,* 2018]. Input data of high resolution and adequate quality can improve the performance of these algorithms.

The accuracy and quality of thermal imagery are largely determined by the altitude at which it is collected. Images collected at lower altitudes produce more accurate canopy temperatures and can differentiate crop pixels from soil pixels better than images acquired at higher altitudes. Using different altitudes of flight over the same soybean field, Thomson et al. [Thomson *et al.*, 2012] investigated these effects. It was found that flight altitude influenced the canopy temperature estimation significantly and 58 % of the variability in canopy temperature was explained by altitude alone. Furthermore, absolute canopy temperature estimates from imagery were measured 4 to 6 °C, different from temperatures measured by a precise infrared radiometer at ground level. In another study [Heilman *et al.*, 1976] conducted with a thermal scanning sensor in an aircraft at 610 and 1220 meters above ground level to estimate crop canopy temperature, the sensor produced absolute errors of 1 to 6 °C in its measurements. These errors were attributed to the effects of the atmosphere, which increases with altitude. To reduce these errors, a correction procedure had to be implemented, making the process more complicated and potentially less accurate. There have been few more studies [Awais *et al.,* 2022, Sangha *et al.*, 2020] to determine the effect of varying low altitudes on canopy temperature sensing accuracy, but for crops with clearly visible gaps between rows. There is much variation in row spacing and canopy coverage from crop to crop. Vineyards, for example, have a spacing of a few meters in between rows, whereas corn is planted in much denser rows. This leads to large differences in fractional ground cover, ranging from 0 to 1 depending on crop stage [Baluja *et al.,* 2012; Han M. *et al.*, 2018]. These variations in canopy cover can affect temperature extraction and accuracy of extracted data. Thus, it is necessary to conduct these investigations in crops like corn at full canopy cover stage.

1.6 Research objective

In order to assess precise spatial canopy temperature, a thorough understanding of the effect of imaging altitude on corn canopy temperature sensing is required. This can be achieved by exploring thermal remote sensing at multiple low altitudes and high altitudes. Further, methods integrating high-resolution thermal imagery (centimeter-level spatial resolution) and ground-based baselines to quantify precise crop water stress need to be investigated for Corn in Kansas, USA region. Therefore, this study aims to:

- Examine the effect of different combinations of imagery collection altitude and camera view angle (focal length) in corn at full canopy cover stage on
    - Accuracy of canopy temperature estimates and the ability of thermal imagery to distinguish between hot and cold surfaces
    - Imagery's spatial resolution, ease of image stitching/orthomosaicing, geometric accuracy, and image quality.

- Develop precise spatial thermal map of corn fields with different irrigation treatments
- Develop a high-resolution spatial crop water stress index (CWSI) for corn using thermal infrared imaging from UAV and locally customized water stress baselines in Kansas, USA.
- Evaluate UAV-based CWSI against vegetative indices from near-infrared imagery and ground data on plant stress indicators
- Examine the capacity of UAV, aircraft, and satellite-based thermal and multispectral imaging in detecting canopy temperature and health variability in corn at a very fine scale for irrigation management.

Chapter 2 - Spatial corn canopy temperature extraction: How focal length and sUAS flying altitude influence thermal infrared sensing accuracy

2.1 Abstract

Irrigation water management starts with quantifying irrigation prescriptions based on crop water requirements at a spatial scale. The most accepted and effective method for estimating this water need is to use the canopy temperature of the plants. The use of small unmanned aerial systems (sUAS) with a thermal infrared camera has long been established as an effective method of measuring plant canopy temperatures at a spatial scale. However, concerns still exist about the accuracy of canopy temperatures collected by these systems and how imagery collection altitude or camera viewing angle affects the temperature estimation. To address these concerns, this study was designed to evaluate the effects of flying altitude of airborne thermal infrared (TIR) imagery and camera view angle on corn-canopy temperature sensing accuracy and image quality. Three different thermal cameras with focal lengths of 9mm, 13mm, and 19mm were used, and each camera was flown at an altitude of 30m, 50m, and 70m. Thermal cameras were mounted on an sUAS and flown over a 6000 m^2 cornfield. The sUAS was flown at a speed of 3m/s on autopilot mode guided by pre-planned missions. The thermal camera was triggered once per second, and imagery was geotagged using an external GPS unit. Images obtained using different combinations of focal lengths and flight altitudes were processed and converted into orthomosaics. Calibration was conducted using ground-based temperature reference panels and temperature maps were created from the orthomosaics. The orthomosaics were examined for the accuracy of the corn-canopy temperature sensing, ability to differentiate between hot and cold surfaces, ease of image

stitching/orthomosaicing, geometric accuracy, image quality and spatial resolution. The results indicated that with the combination of appropriate camera focal length, altitude, and image calibration techniques, a canopy temperature map of crops with a temperature error of less than 2° C from the actual canopy temperature can be produced. A narrow-angle thermal camera flying at low altitudes (<50m) was found to be the least suitable combination for corn canopy temperature sensing. The most appropriate combination for temperature estimation of corn canopies was with a 13 mm focal length camera flying at an altitude of 50m above ground level.

2.2 Introduction

Precision agriculture is a system that combines advanced machinery, sensors, information systems, and guided management to optimize production, while aware of different uncertainties and variations in agriculture. Precision agriculture offers a way to regulate the course of agricultural production and maintain product quality as well as quantity through site-specific inputs. The ultimate goal of precision agriculture is to improve profits and sustainability by optimizing the input of resources [Gebbers *et al*., 2010]. To achieve this goal, many tools and techniques are used to detect and quantify in-field variability of crop and soil parameters. Further to derive information that improves the efficiency of inputs, while protecting or increasing the yield [Khanal *et al.*, 2017].

Remote sensing has emerged as a vital tool for collecting and interpreting information about features of in-field plants and soil. Remote sensing in agriculture is influenced by the nature of the platform used (satellite, ground, or in the atmosphere), the section(s) of the electromagnetic spectrum used (infrared, RGB, microwaves), spatial resolution, spectral resolution (hyperspectral, multispectral, or single bands) of the sensor, radiometric resolution, and temporal resolution (the frequency and time-precision of revisiting an area) [Metternicht, G., 2008]. Satellite imagery has been extensively used in many applications in agriculture and vegetation studies in past years. Satellite imagery is susceptible to degradation by atmospheric factors. These factors include light absorption, scatter by clouds, variations in various particulates, aerosols, gasses, and temperatures that reduce availability and consistency of satellite imagery.

Unmanned Aerial Systems (UAS) can reduce limitations posed by atmospheric degradation of imagery by flying closer to ground level and excluding the majority of atmospheric degradation effects on light reflected from surface objects. However, it does not remove atmospheric factors related to incident light, such as effects related to light incident angle or cloud shadows [Barzin *et al.,* 2020]. UAS imaging can also be done at far finer spatial resolutions compared to other remote sensing platforms because the sensors are much closer to the objects of interest. Images derived from modern satellites used in agricultural applications typically have spatial resolutions of 2-15 meters. Manned aircraft can operate at lower altitudes and typically achieve spatial resolutions of 0.2-2 meters. Typical UAS used in agriculture can provide imagery with spatial resolutions in the 1-20 cm range. Even finer resolutions are used in some specialized applications because UAS has no lower limits on altitude above ground level. UAS therefore fills the resolution gap between ground-based observations and observations using other remote sensing platforms. Furthermore, fine spatial resolution imagery in the low centimeter range, has shown great promise in recent agricultural research on crop management, plant disease detection and mapping, quantification and mapping of field variability for site-specific inputs [Nebikera *et al.*, 2008]. UAS flights can be planned and executed rapidly and at relatively low cost. These targets key phases of phenological development and adjustment in response to the availability of favorable weather conditions [Barzin *et al.,* 2020]. A notable limitation of UAS applications in agriculture is the relatively small operational range. The limited energy capacity of current batteries and regulations that generally limit UAS operations to visual line of sight of the pilot bounds flight duration in typical agricultural UAS platforms. The maximum area that can be surveyed in a single flight is usually in the hundreds of acres range and may be even lower when very fine spatial resolution is required. Most agricultural UAS applications are therefore aimed at observations of individual fields or small groups of fields that are near each other. However, the advantages of agricultural UAS including relatively low costs of operations, flexibility in deployment, excellent spatial and temporal resolution have been key drivers in the agricultural use of UAS. Particularly in applications related to the generation of time-critical information and precision agriculture applications at the field-level [Berni *et al*., 2009].

The imaging sensors mounted on airborne platforms receive majority of incoming electromagnetic energy from target surfaces. This is in the form of reflected light, usually in the visible (VIS) and near infrared (NIR) wavelength ranges. Incoming energy can also be due to backscattered light from atmospheric components, or emitted light (including thermal infrared and fluorescent light) [Metternicht, G., 2008]. Different plant characteristics can be determined using specific wavelength regions of received electromagnetic energy. For example, rate of photosynthesis or leaf chlorophyll content can be estimated from fluorescence (683 nm and 740 nm) using hyperspectral bands. Customized cameras that detect two or more bands {example: red (630 nm-690 nm) and NIR (770 nm-900 nm)} can be used to determine an index that is correlated with leaf area, wilting stage, canopy structure, or canopy coverage. Thermal infrared {TIR (7500 nm – 13500 nm)} imaging can be used to quantify crop canopy temperature. Canopy temperature (Tc) is relatively quick-response characteristic that does not depend on plant structure or pigment changes, which take more time to develop and are the main drivers of variability in visible light and NIR remote sensing of plants [Khanal *et al.,* 2017]. Major application of Tc is for plant-based or site-specific irrigation management to attain precision irrigation in agriculture. Tc is one of the most useful crop characteristics when it comes to provide insight into water status of the plants [Brewer *et al*., 2022; Crusiol *et al*., 2020; Pineda, *et al.,* 2020, Zhou, Z. *et al*., 2021]. A leaf's cooling mechanism i.e., stomatal aperture, which is influenced by soil and plant water content and weather conditions, regulates the temperature of the leaves by means of controlling evapotranspiration. In adequate irrigated conditions, plants increase transpiration rate as a response to increasing environmental temperature, resulting into minimal changes in canopy temperature.

Whereas, under water deficient conditions, transpiration rate decreases, reducing leaf cooling effect, ultimately increasing Tc significantly [Giménez-Gallego *et al.*, 2021; Jones, H.G., 2014; Zhang, L. *et al.,* 2019]. It is for this reason that canopy temperature has become the most accepted and reliable tool for estimating plant water requirements.

A UAS-based thermal remote sensing approach serves as a routine tool for monitoring plants' canopy temperatures. TIR images collected over an agriculture field can be combined to generate orthomosaic maps of crop canopy temperatures. However, concerns still exists on accuracy of canopy temperatures collected by these systems and data extracted from imagery. An important concern for data extraction from thermal imagery is the need to separate pure crop canopy pixels from soil background. Thermal image processing is limited due to the low resolution of thermal cameras (from 320 × 240 to 640 × 480 pixels). It is often difficult to effectively separate soil pixels from crop pixels in thermal images, causing significant bias in Tc measurements. The most common method for excluding background pixels is using thermal imagery with RGB and multispectral imagery together, called co-registration approach [Sagan *et al.*, 2019; Zhang, L. *et al.,* 2019; Zhang, Y. *et al.,* 2023]. Crop pixels can be separated in RGB or NIR imagery using different classification algorithms, and then co-registered with thermal imagery to extract canopy-only temperature values. Several scientists have also explored approaches which only use thermal imagery to extract pure canopy pixels, using edge detection algorithms [Bian *et al*. 2019; Ludovisi *et al*., 2017; Meron *et al*., 2013; Zhang, Z. *et al*., 2018]. Input data of high resolution and adequate quality can improve the performance of these algorithms. The accuracy and quality of thermal imagery is largely determined by the altitude at which it is collected. Images collected at lower altitudes produce more accurate canopy temperatures and can differentiate crop pixels from soil pixels better than images acquired at higher altitudes. Using different altitudes of flight over the same soybean field, Thomson et al. [Thomson *et al.*, 2012] investigated these effects. It was found that flight altitude influenced the canopy temperature estimation significantly and 58 % of the variability in canopy temperature was explained by altitude alone. Furthermore, absolute canopy temperature estimates from imagery were measured 4 to 6 °C different from temperatures measured by a precise infrared radiometer at ground level. In another study [Heilman *et al.*, 1976] conducted with a thermal scanning sensor in an aircraft at 610 and 1220 meters above ground level to estimate crop canopy temperature, the sensor produced absolute errors of 1 to 6 °C in its measurements. These errors were attributed to the effects of the atmosphere, which increases with altitude. To reduce these errors, a correction procedure had to be implemented, making the process more complicated and potentially less accurate.

In order to provide adequate quality thermal imagery data for corn crop canopy classification tools and gain insight into the effect of altitude on canopy temperature sensing, thermal remote sensing at varying low altitudes needs to be extensively explored. There have been a few studies [Awais *et al.,* 2022, Sangha *et al*., 2020] to determine the effect of varying low altitudes on canopy temperature sensing accuracy, but for crops with clearly visible gaps between rows. There is much variation in row spacing and canopy coverage from crop to crop. Vineyards, for example, have a spacing of a few meters in between rows, whereas corn is planted in much denser rows. This leads to large differences in fractional ground cover, ranging from 0 to 1 depending on crop stage [Baluja *et al.,* 2012, Han M. *et al.*, 2018]. These variations in canopy cover can affect temperature extraction and accuracy of extracted data. Thus, it is necessary to conduct these investigations in crops like corn at full canopy cover stage. Therefore, this study aims to examine the effect of different combinations of camera view angle (focal length) and imagery collection altitude in corn at full canopy cover stage on:

- The ability of thermal imagery to distinguish between hot and cold surfaces and accuracy of canopy temperature estimates.
- Imagery's spatial resolution, ease of image stitching/orthomosaicing, geometric accuracy, and image quality

2.3 Materials & Methods

2.3.1 Unmanned Aerial System (UAS) and Thermal Imaging System

A quadcopter (Matrice 100, Shenzhen DJI Sciences and Technologies Ltd.) was used for imagery collection. The aerial system has a payload capacity of 1 kg with a maximum flight time of 40 minutes. Two lithium-ion batteries were used to supply power to the sUAS. Each battery has 5700 mah of energy capacity. FLIR Vue pro-Thermal Infrared (TIR) sensors from FLIR Systems, USA, were used for thermal imaging. The weight of the sensor was 350 g, and it was mounted facing straight downwards during normal aircraft flight attitude. Missions were planned with a maximum estimated flight time of 25 minutes to ensure an adequate safety margin for potential

Figure 2.1. Quadcopter Matrice 100 used with the FLIR Vue pro Thermal Infrared Sensor

flight duration. Three different thermal cameras with focal lengths of 9mm, 13mm, and 19mm were used. These are the most common focal lengths commercially available for thermal cameras and cover the range of low, medium, and wide fields of view. Each camera was flown at an altitude of 30 m, 50 m, and 70 m. Each one had the size of 5.74 cm x 4.45 cm, Uncooled Vox Microbolometer thermal imager, a frame rate of 30Hz, and an image pixel count of 640 x 512. The spectral band used by the cameras was 7.5 – 13.5 µm, and images were collected in 14-bit tiff format. The cameras can also record in 8-bit Jpeg format. In this format, camera can autocorrect the difference in the radiance from the object and assign uniform values to pixels. This results in estimated information regarding the radiance from the object and introduction of a degree of error. In 14-bit tiff format, autocorrection is not applied, and results in image pixels that represent a closer estimate of actual radiance differences. Corrections to improve absolute temperature estimates were based on thermal calibration panels placed at ground level, as described below.

2.3.2 Research Site

The study was conducted on corn at the Kansas Research Valley experiment field (39.076076° N, -95.768777° W), Silver Lake, Kansas, USA, with Eudora Silt Loam soil type. Corn was planted on 22 April 2020, and the plot used for the study was a small part (Approx. 6000 m^2) of the entire field (16000 m^2). Assessment of a sub-section of the field was needed in order to make it possible to perform multiple flights in a short duration around solar noon, ensuring that environmental conditions remained consistent between flights.

2.3.3 Mission Planning

Missions for the flights were made in Mission Planner (Version 1.3.72) by ARDUPILOT. Mission Planner was not directly compatible with the sUAS used, so a compatible software platform (Litchi, VC Technology Ltd) was used to transfer missions from Mission Planner to the sUAS. The area of interest was selected using a polygon tool and auto waypoint generation tools in the software. The waypoints were saved in an excel file for importation into the Litchi platform. A compatible data file (.csv) was exported from Litchi and stored online in a Litchi account for repeated use. A separate autopilot and GPS unit (Pixhawk, 3DR) was used with the original Mission Planner flight plan to trigger the camera and tag images with coordinates. The missions were planned to collect imagery as close as possible to the solar noon, before and after solar noon plants will start showing shadow on the side, which increases with distance from solar noon, and introduces an additional source of error in temperature estimates. So, most flights were conducted close to solar noon (13:21 pm) as shown in Table 2.1, but a couple of missions were repeated due to technical issues, resulting in approximately $\pm$ two hours from solar noon.

The flight speed was 3 m/sec, and the camera was triggered once per second based on the

Table 2.1. Mission details and imagery data for different flights. The number of filtered images represents the images used to develop orthomosaic

Flights	No. of images (Filtered)	No. of images (Original)	Time of Flight (Original)	Flight Duration (min)	Overlap
9mm-30m	181	322	11:33:38-11:39:00	7	F 80 S 80
9mm-50m	232	318	11:49:03-11:54:20	7	F 90 S 89
9mm-70m	120	191	12:02:06-12:05:16	4	F 90 S 89
13mm-30m*	298	385	15:34:43-15:41:07	8	F 76 S 79
13mm-50m	233	321	15:26:53-15:32:14	7	F 85 S 85
13mm-70m	238	321	15:14:09-15:19:29	7	F 90 S 90
19mm-30m*	302	385	13:39:02-13:45:27	8	F 66 S 70
19mm-50m*	354	448	14:26:14-14:33:41	10	F 85 S 85
19mm-70m	234	320	14:18:38-14:23:57	7	F 87 S 82

*Orthomosaic was not acceptable

earlier study [Sangha *et al*., 2020] performed. According to this study, if higher flying speed is used, then the images will go blurry and not provide detailed information from the crop. If the sUAS is flown at a slower speed, it will not be able to complete the low altitude flights in the time window restricted due to battery capacity and solar noon. At this speed, image triggering was kept after one second as recommended by the mission planner and keeping in mind the image stitching process. Triggering at every two seconds was attempted, but results were not favorable. Images were not stitched, which worked adequately for one second trigger time. Overlap for different altitudes was kept according to flight time limitation and image stitching suitability observed in the previous study [Sangha *et al*., 2020]. In most of the flights, front (F) and side (S) direction overlap was more than 80%. At lower altitudes because of exceeded flight time, it was kept at an acceptable lower level [Sangha *et al*., 2020] as shown in Table 2.1. Different thermal cameras collected different number of images in respective mission, depending on the overlap, altitude and focal length of the camera, mentioned under No. of images (Original) column in Table 2.1.

2.3.4 Image stitching and Orthomosaicing

It was necessary to combine all photos from a single flight and make a collective image or mosaic. This replicates entire field to analyze the crop canopy throughout the field. These mosaics were precisely georeferenced to ensure that measured ground data on a site can be compared with data extracted from the imagery at the same location. Ground control points (GCP), in the form of black and white panels (Figure 2.2), were used for geometric calibration of imagery. A real-time kinematic (RTK) global positioning system receiver Topcon GR-5 (Topcon, Tokyo, Japan) with <1 cm accuracy was used to survey GCP coordinates. The RTK technique improves GNSS position accuracy by sending correctional data wirelessly from a fixed base station to a moving receiver/rover. The base unit was established near the field boundary and the rover was used to get the position of the center of GCP. The GCPs were typically kept at a distance of 50 m from each other. A total of 16 GCPs were placed eight on the boundary of the field and eight inside the field. Metashape Professional by Agisoft (Agisoft LLC, St. Petersburg, Russia) was used to generate georeferenced orthomosaics from individual images [Han X. *et al.,* 2018, Nebikera *et al.*, 2008].

Figure 2.2. Topcon Gr-5 base station with a rover unit, for collection of RTK corrected GCPs coordinate

Before processing, blurred images were removed to avoid unnecessary errors. The number of images used in orthomosaic generation after using this filtering process are mentioned under No. of images (Filtered) column in Table 2.1. These sorted images then converted into orthomosaics using Agisoft's standard workflow for orthomosaic generation (Figure 2.3). In this workflow, the

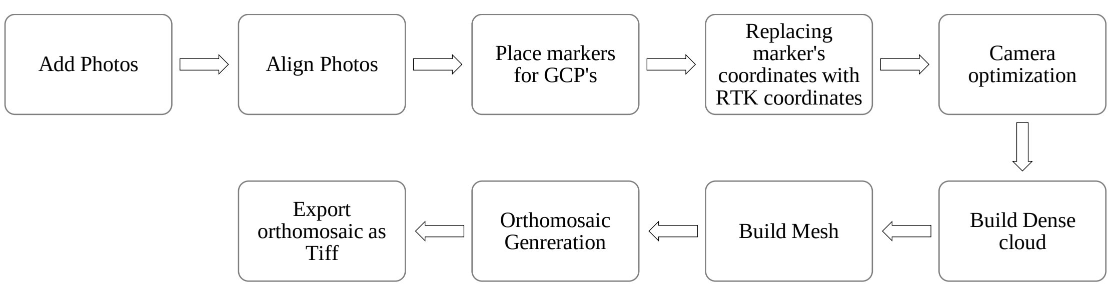

Figure 2.3. Agisoft's standard workflow for orthomosaic generation

center of GCPs were marked in individual images and later replaced with RTK based ground collected coordinates. Cameras were optimized with these new precise locations of GCPs. In this way, orthomosaic created will be highly accurate in terms of positioning. Four calibration panels were used to convert orthomosaics into temperature maps, similar ground-based calibration was used in previous studies [Han X. *et al.,* 2020; Sangha et al., 2020]. A water-covered white panel generated the coolest temperature, and dry panels, from white to grey to black (Figure 2.4), generated increasing reference temperatures. The temperatures of the panels were recorded using Flir TG167 Spot Thermal Camera (Flir Systems Inc, Wilsonville, OR, USA), within 45 seconds of the sUAS passing over the panels. The average pixel values for each panel were extracted from the orthomosaic. These pixel values represented thermal camera's response for the particular panel, while real-time temperature of that panel has already been recorded with a spot thermal camera. Based on the pixel values and the real time temperature values for each panel, a regression equation

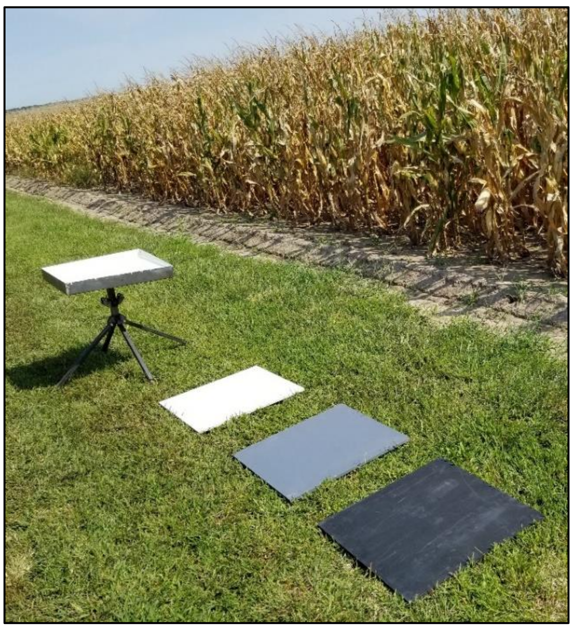

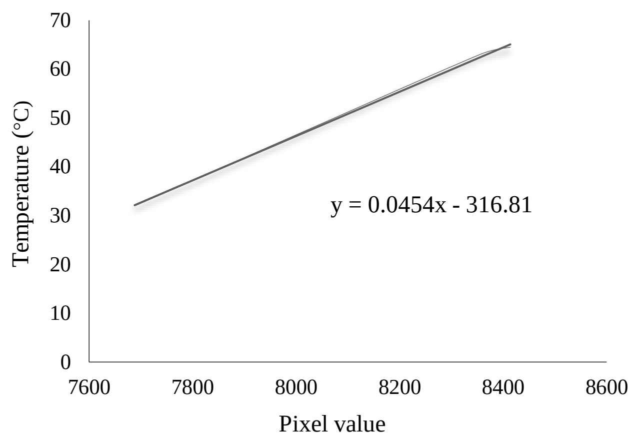

Figure 2.4. Panels used to calibrate imagery pixels: Black, gray, white and water panel and sample calibration curve

(Figure 2.4) was developed for each flight. This regression equation was then used to convert whole field's pixels in an orthomosaic to temperature values (temperature maps) in ArcMap 10.6.1 (ArcGIS, ESRI, Redlands, CA, USA) using the Raster Calculator tool.

2.3.5 Image Quality Analysis

2.3.5.1 Spatial Resolution and Spectral Discrimination

In thermal imagery, the radiance measurement accuracy decreases because of scattered light, optical distortion, diffraction, and sensor image processing, resulting in a blurred section in image, which is called the spot size effect. A measurement spot of at least 10 pixels in diameter should be considered for any meaningful result to decrease this effect. A diameter of 20 pixels is large enough to negate the effect of the spot size. If we do not consider this minimum pixel limit, then the observed data will not be the same as the actual data, thus leading to significant errors. So, the determination of ground resolution is vital to eliminate the possibility of spot- size effect in temperature extraction. Using Arc map, each orthomosaic was zoomed in to the extent where individual pixels can be seen. Then the dimension of the pixel was measured. This is recorded as the spatial resolution of imagery. Further, to visualize the effect of spatial resolution of imageries from different missions, temperature orthomosaics were classified using Arc Map in a stretch from the temperature of 24 °C to 45 °C and exported as a Map over an area near the western boundary of the field (Figure 2.7). The minimum and maximum temperature values for the classification of orthomosaics were chosen to cover the range of the crop and background temperature. Discrimination analysis was performed to evaluate the imagery for the level of temperature discrimination for crop and background soil. The black wooden panel that was used for temperature calibration was also used for this analysis. Pixel values across the panel were plotted against the pixel number from West to East. Starting and ending points were off the wooden panel so that a difference of pixel value in background soil and panel could be observed. Parabolic pixel value curves were observed across the transitions between panel values and background values. The patterns of the change in slope were used to determine the widths of the transition zones between background values and reliable panel values. They were also used to indicate the effective spatial resolution of temperature discrimination between plant canopy and soil background. The steeper slope represents distinct discrimination, and the greater pixels on the flat section of the curve in the middle represents greater resolution of information from the panels (crops in real world scenario). So, the most desired curve will be with a steeper slope to reach the peak and more no. of pixels on the horizontal span.

2.3.5.2 Geometric accuracy

The geometric accuracy of generated orthomosaics were evaluated against ASPRS (American Society for Photogrammetry and Remote Sensing) Positional Accuracy Standards for Digital Geospatial Data (EDITION 1, VERSION 1.0.0, 2014). It defines horizontal accuracy classes in terms of their Root Mean Square Error in the X direction (RMSEx) and in Y direction (RMSEy) values. For example, consider an orthomosaic having a resolution of 7.5 cm. If the calculated RMSEx and RMSEy values are less than 7.5 cm, or 1-pixel of the orthomosaic, then the recommended horizontal accuracy class for this will be "highest accuracy work". This class reflects the highest level of accuracy for the specified resolution. In contrast, RMSEx and RMSEy values of 15.0 cm, or equivalent to 2-pixels of orthomosaic, are classified as "standard mapping and GIS work". This is appropriate for a standard level of precision and high-quality geospatial mapping application. This level of precision is typical of most current projects designed to meet existing standards. If RMSEx and RMSEy values are greater than 22.5 cm, or 3-pixels of orthomosaic, then the horizontal accuracy class for this will be "visualization and less accurate work", generally used when higher accuracies are not required. A sheet patterned identically to a black and white checkerboard with 12 "x 12" of individual square-sized boxes was used for this analysis (Figure 2.5). Intersecting points of black and white boxes were used as the reference points. Coordinates of these points were extracted from orthomosaics using ArcMap. Ground based coordinates of these points were also collected using real-time positioning data from the

Figure 2.5. Sheet used for geometric accuracy analysis consisting black and white checkerboard boxes

Topcon GR5 RTK system, which has an accuracy of < 1 cm for horizontal surveying. A difference/error in position, measured in centimeters, was calculated using coordinates of these 18 intersecting points from orthomosaic and ground based RTK positions. The errors were calculated for both north–south (y) and east–west (x) directions. Further, these errors were squared and their root mean values were derived, which were called RMSEy and RMSEx. These values were then compared for all flights. Smaller RMSE values indicate more accurate orthomosaic locations.

2.3.5.3 No-Reference Quality Metrics (NRQM) Analysis

The relative visual quality of images was calculated using NRQM scores for each flight. These scores were calculated using BRISQUE and NIQE algorithms available in MATLAB, which can be applied directly to images. NRQM algorithms use statistical characteristics of input imagery instead of a reference image to evaluate image quality as used in reference quality metrics. This method includes two major algorithms for image quality analysis, and both models use similar predictable statistical elements known as Natural Scene Statistics (NSS). These statistics are established on standardized luminance coefficients in the aspect of the spatial domain, and a Gaussian distribution is used to model them in multidimensions. Distortion in images comes out as a disturbance in this distribution. The two algorithms differ only in how they use these NSS features to get the required quality scores.

The first model is Blind/Reference less Image Spatial quality Evaluator (BRISQUE). It is a trained model which uses the data of images with already known distortions. Therefore, this model will be limited to analyze imagery based on the same type of distortion. It is an opinion-based model that limits its freedom of analysis but provides an edge of better correlation -with human perception of image quality. The lower the BRISQUE score the better the image quality. The other type of technique used is Natural Image Quality Evaluator (NIQE), this can measure the random distortions in imagery and is an opinion unaware model. It does not use subjective quality comparison and will not correlate with human perception of image quality compared to BRISQUE. This model selects the statistically significant segments from the distorted image and extracts NSS features from them. Then it fits the multivariate Gaussian distribution to the NSS feature of available imagery. The distance among these Gaussian distributions will be considered as our NIQE score.

2.3.6 Temperature Extraction

From the temperature-converted orthomosaics, temperature values were extracted at four ground truthing locations (GTL) using ArcMap. Three locations were near the West boundary of the field, from where ground truthing data was collected using a handheld FLIR thermal camera. An Apogee radiometer SI-111 was installed at the fourth GTL. The radiometer was kept at two feet above the canopy, at a 45° angle of view. It was used to estimate crop canopy temperature once per minute. Three temperature values from the datalogger were used for each flight. Including the temperature closest to the start of the flight, and two more values at 10-minute intervals. The average of these three values represents the GTL4 ground (Grd) value in the results section. For the remaining three sites, ground data at each site was recorded for three plants. Per plant, three leaves open to sunlight were selected, then the temperature at three different spots on each leaf was recorded using the handheld FLIR thermal camera. These 27 canopy temperature values were averaged for an individual flight representing real-time crop canopy temperature (Grd) of that GTL. The temperature values were extracted from orthomosaics using 3D-analyst tools from ArcMap. These tools enable us to create a new feature and query attribute values on a surface along the feature. A line (feature) was drawn along the crop rows for a distance of 2.5 m on the temperature orthomosaic (surface). Next, a profile graph was generated showing the temperature values corresponding to the pixels along this line. The profile graph values were then exported as numbers and averaged to get single value representing one replication. At each GTL, three replications were pulled from crop rows and two from aisles. These values were then averaged and the average output value (Img) represented individual GTL for each flight.

2.4 Results and discussion

2.4.1 Image stitching and orthomosaics

Images from missions with camera focal length 13 mm at flying altitudes of 30 m and for 19 mm focal length at 30 m and 50 m altitude did not realize a composite orthomosaic using the modeling software. Image alignment is a very critical step of image processing. It depends on availability of sufficient discrete features and quality information in images. Considering the fact that images from a wide viewing angle camera (9 mm focal length) cover more area on the ground, as compared to a narrow-angle camera (19 mm focal length), the modeling software could not identify significant common features between overlapping images from the narrow-angle camera used at lower altitudes. The challenge of identifying enough discrete features significantly increased in a crop such as maize at full canopy coverage. The imageries covered a small area in a single image and were imaging the canopy such that only a uniform surface of crop canopy, that looks similar in multiple images, appeared in adjacent images. Overall, the image datasets from

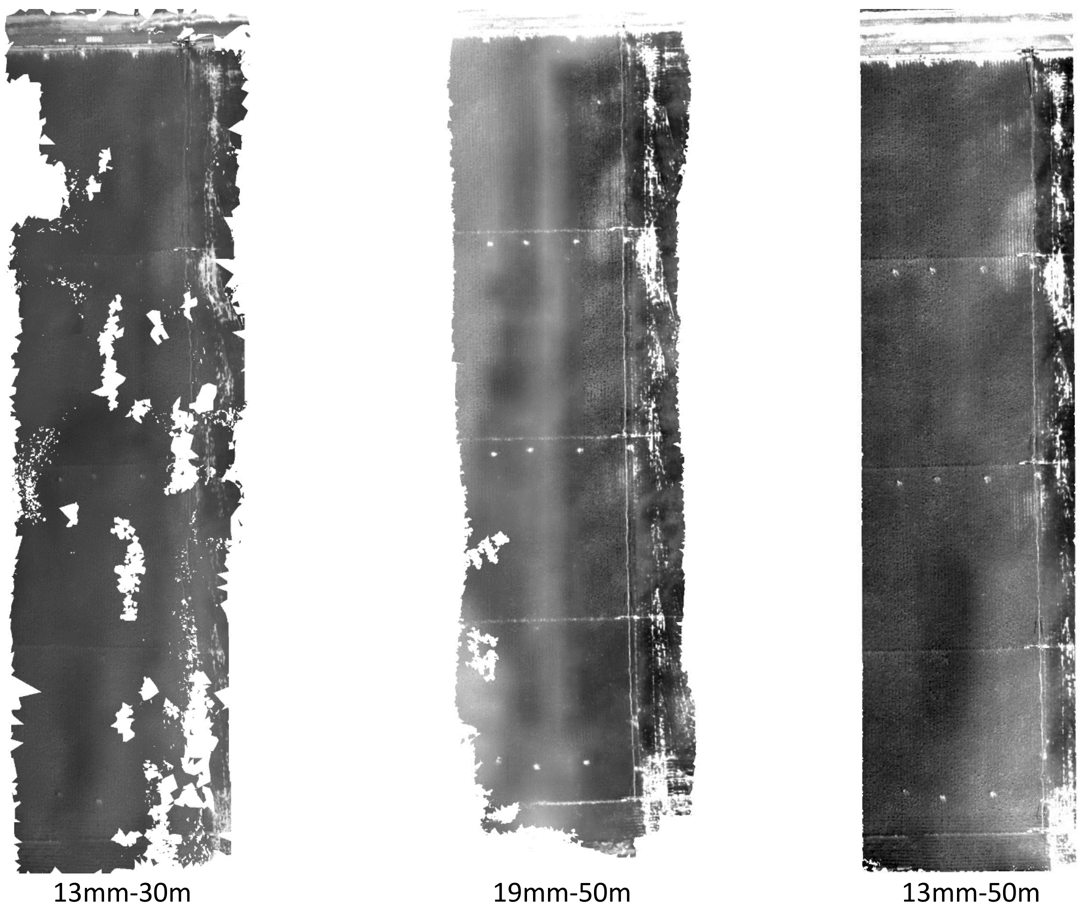

Figure 2.6. Poor quality orthomosaics (13mm-30m and 19mm-50m) in comparison with a good quality orthomosaic (13mm-50m)

the aforementioned missions (13 mm focal length at 30 m and for 19 mm focal length at 30 m and 50 m altitude) presented considerable challenges in the alignment, reduced the quality of orthomosaics [Anderson *et al.*, 2019], did not provide a complete composite orthomosiac for data analytic, and henceforth were not analyzed further for inclusion in the results section. Orthomosaics generated from imagery with the 9 mm camera at all altitudes, 13 mm camera at 50 m and 70 m, and 19 mm camera at 70 m provided satisfactory quality and fulfilled all the data analysis needs. Therefore, data from only these orthomosaics was considered for further data analysis and presentation in the results section. Since, combination of 13 mm camera focal length and 50 m altitude produced a healthy orthomosaic and there were no missing points in orthomosaic and all images were aligned, it was kept as a reference orthomosaic for the comparison with poor quality orthomosaics. Analysis of the processing report of orthomosaics indicated that, 13 mm camera at 50 m utilized 76,810 tie points out of 84,811 key points to generate a point cloud. The 3-D model of this imagery set has 177,179 faces and 89,385 vertices. It was found that in 19 mm camera at 30 m altitude imagery, only 22 images out of 356 were aligned, and these images have only 3029 tie points available out of 36,307 key points in the point cloud. This is significantly less number as compared to reference orthomosaic. The other two incomplete orthomosaics have enough tie points available for images to be aligned, but the 3D model from the imagery of the 19 mm camera at 50 m has only 26,459 faces and 14,485 vertices; and from 13 mm camera imagery at 30 m has 38,257 faces and 20,868 vertices. These results explained the incomplete alignment of images and incomplete composite orthomosaics from certain missions (Figure 2.6). Therefore, users should be mindful of carefully selecting a camera focal length and flying altitude in order to develop a complete orthomosaic.

2.4.2 Geometric accuracy and No Reference Quality Metrics (NRQM) Scores

Geometric accuracy analysis showed that 9 mm camera at 30 m altitude has the highest values for RMSEx and RMSEy of 15.93 cm and 20.26 cm, respectively. Spatial resolution for this imagery was 5.51 cm, so this imagery showed an accuracy of approximately three pixels for y-direction and x-direction, indicating the imagery under “visualization and less accurate work” category not recommended for “standard mapping and GIS work”. On the contrary, the 13 mm imagery at 50 m altitude, exhibited the RMSEx value 2.87 cm, and the RMSEy value of 4.53 cm, with a spatial resolution of 6.5 cm. The RMSE values from 13 mm imagery at 50 m altitude imagery provided an accuracy of less than one pixel, thereby enabling its suitability for “standard mapping and GIS work”. Similarly, results were observed for imagery from 9 mm camera at 50 m and 70 m altitude; 13 mm camera at 70 m; and 19 mm camera at 70 m altitude, suggesting those

Table 2.2. RMSEx and RMSEy values for orthomosaics

Focal Length	Altitude								
	30m			50m			70m		
	$RMSE_x$ (cm)	$RMSE_y$ (cm)	Spatial Resolution (cm)	$RMSE_x$ (cm)	$RMSE_y$ (cm)	Spatial Resolution (cm)	$RMSE_x$ (cm)	$RMSE_y$ (cm)	Spatial Resolution (cm)
9mm	20.26	15.93	5.51	11.49	10.72	9.74	6.37	6.51	13.75
13mm	-	-	-	2.87	4.53	6.5	6.58	10.58	9.1
19mm	-	-	-	-	-	-	9.14	5.21	6.4

*Columns with dashes indicate the missions not considered for analysis

to be suitable for "standard mapping and GIS work". Overall, imagery from all combinations of camera focal length and altitude presented in Table 2.2, except the 9 mm camera at 30 m altitude, qualified the metrics needed for "standard mapping and GIS work". However, 13 mm camera at 50 m altitude provided lowest RMSE values compared to all other combinations of camera focal lengths and flying altitudes. Average BRISQUE and NIQUE scores did not show significant

Table 2.3. BRISQUE and NIQUE scores for different flights

Flights	BRISQUE	NIQUE
9mm-30m	44.48	12.20
9mm-50m	46.96	10.70
9mm-70m	45.36	11.51
13mm-50m	44.57	12.14
13mm-70m	46.76	10.76
19mm-70m	46.21	11.06

deviations from one flight to another (Table 2.3). These results implied that altitude and focal length did not impact image quality to a significant level. So, users may choose the camera and altitude combination according to the requirement without any concerns of image quality.

2.4.3 Spatial Resolution and Spectral discrimination

If different focal length and altitude combinations are compared, spatial resolution is an essential factor to consider. Images are characterized by their spatial resolution, which determines the level of detail they contain and the smallest object that can be detected. Information on the degree of detail in a single pixel is crucial in order to select the appropriate imaging sensor and its

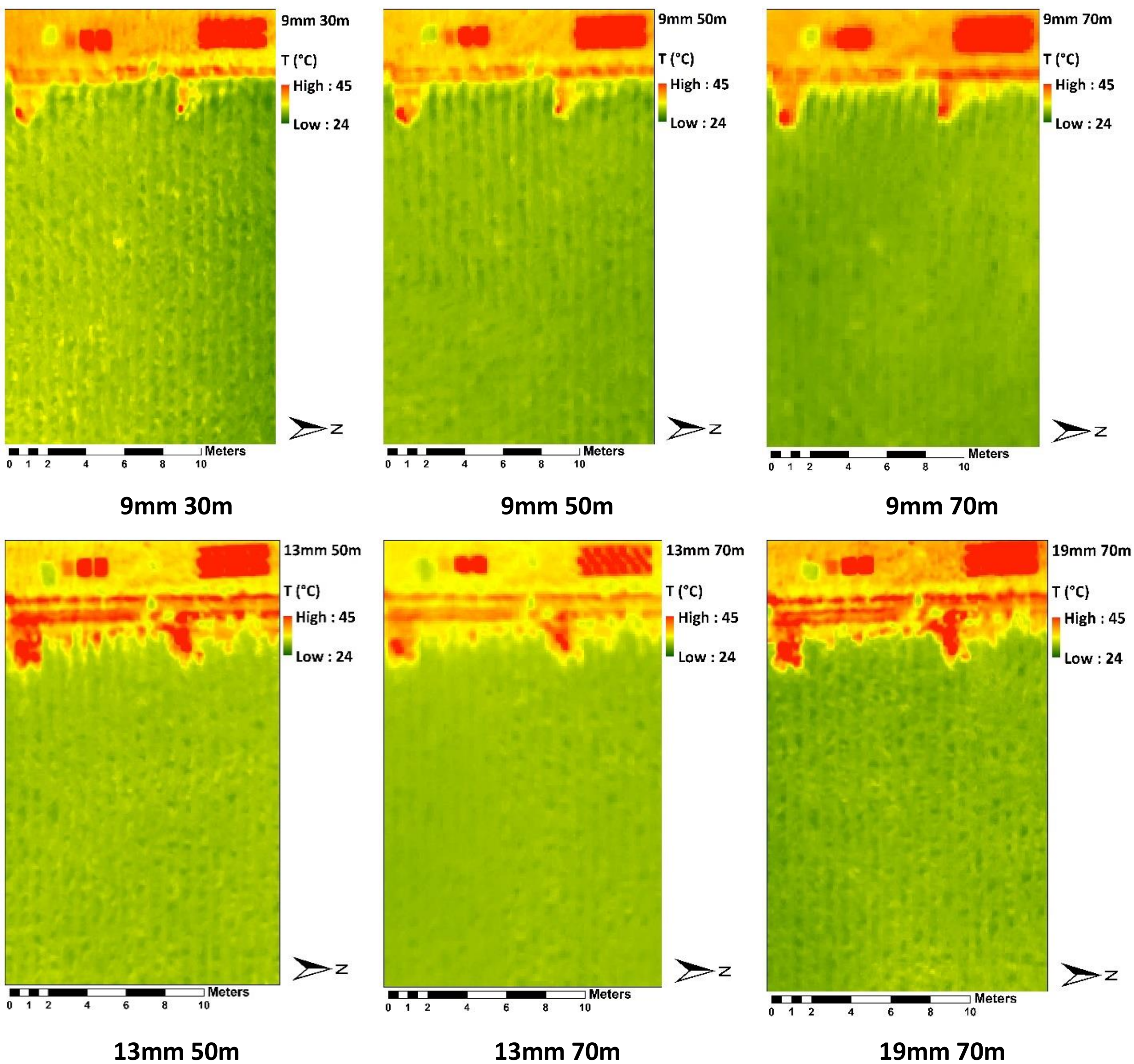

Figure 2.7. Thermal orthomosaics from west boundary area of field for all the flights

flying altitude to distinguish plant rows or individual plants. The lower the resolution, the more likely it is that background pixels in the soil will mix with canopy pixels, leading to false information and errors in extracting canopy temperatures. The spatial resolution of orthomosaics

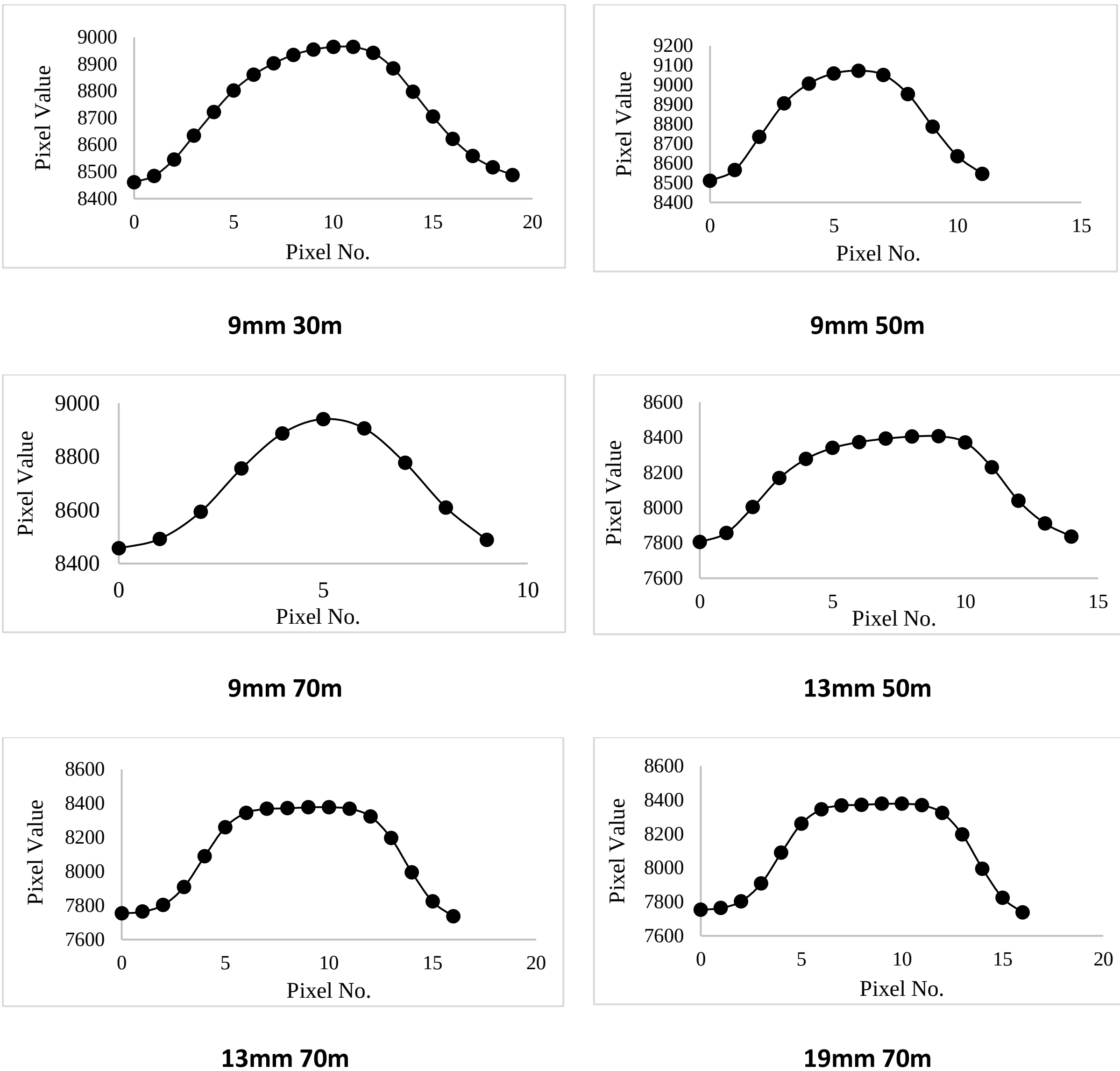

Figure 2.8. Spectral Discrimination curves across black panel

from all the flights was measured with the help of the Arc map. The 9 mm-30 m imagery provides the smallest size of the pixel of 5.51 cm (highest spatial resolution), and 9 mm-70 m imagery has the largest pixel size of 13.75 cm (lowest spatial resolution). As a further aid to interpretation, temperature orthomosiacs generated from all combination of camera focal length and flying altitude are shown in Figure 2.7, ranging from 24°C to 45 °C. Imagery (9 mm-70 m and 13 mm-70 m) with coarser spatial resolution exhibit blurriness near the field boundary in separating green crop regions from light yellow or red soil backgrounds (Figure 2.7). Whereas in imagery with fine resolution less than 6.5 cm/pixel (9 mm-30 m, 13 mm-50 m and 19 mm-70 m) this difference was distinctly apparent with more details. In Figure 2.8, imagery for 13 mm camera at an altitude of 50 m and 70 m and for 19 mm camera at 70m showed a steeper slope and more no. of pixels on a horizontal span at the peak in spectral discrimination plots. The steeper slope observed for these imageries indicated greater discrimination between crop and soil background, while greater number of plotted points on horizontal section at peak (no. of pixel present on the panel) exhibited higher resolution of imagery. The results showed that these imageries displayed satisfactory discrimination in hot and cold pixels. Imagery with the 9 mm camera at 30 m, 50 m, and 70 m had a smooth slope compared to other flights and had fewer pixels on the peak. For practical applications, good spatial resolution would have multiple pixel arrays representing the canopy and good spectral discrimination would represent crop data accurately without the edge effect of soil background [Sangha *et al*., 2020]. Overall, from a spectral discrimination point of view, 13 mm – 50 m, 13 mm - 70 m and 19 mm - 70 m came out as superior to the rest of the combinations, and from a spatial resolution point of view, 13 mm – 50 m, 9 mm – 30 m and 19 mm – 70 m provided better results than the rest of the combinations. Both spatial resolution and spectral discrimination are critical for the easy and rapid extraction of quality crop response data. So, collective analysis of spatial resolution and spatial discrimination indicated that 13 mm – 50 m and 19 mm – 70 m could provide more accurate crop data for users interested in precision management of irrigation technologies.

2.4.4 Temperature Extraction

The temperature difference (Diff) between imagery temperature values and ground temperature values along with its average value (Avg Diff) is included in the analysis, is shown in Table 2.4. The temperature values calculated over crop rows and aisles between two rows (represented within parenthesis) are shown in Table 2.4. The temperature values showed that there was no significant difference between canopy temperatures extracted from rows and aisles. The

Table 2.4. Average temperature values of crop canopy from imagery (Img), ground (Grd) truthing, and difference between Img and Grd temperature values (Diff) for four ground-truthing locations.

Flight	Temperature (°C) for row (gap)												Average Temperature Difference
	GTL1			GTL2			GTL3			GTL4			
	Img	Grd	Diff	Img	Grd	Diff	Img	Grd	Diff	Img	Grd	Diff	
9mm-30m	26.22 (26.74)	32.38	6.16 (5.64)	29.96 (30.40)	32.31	2.34 (1.91)	31.24 (30.53)	31.96	0.72 (1.43)	28.66 (27.91)	28.65	0.01 (0.73)	2.37 (2.43)
9mm-50m	28.85 (29.05)	31.10	2.25 (2.06)	30.11 (30.60)	31.30	1.19 (0.70)	30.26 (30.81)	32.11	1.85 (1.30)	29.08 (28.88)	31.22	2.14 (2.34)	1.73 (1.6)
9mm-70m	30.76 (30.99)	30.93	0.17 (0.06)	29.77 (30.24)	31.18	1.41 (0.94)	29.82 (30.25)	30.50	0.69 (0.26)	27.82 (27.73)	31.17	3.35 (3.45)	1.29 (1.18)
13mm-50m	32.40 (32.33)	32.60	0.20 (0.28)	31.12 (30.96)	32.43	1.32 (1.47)	31.19 (31.23)	33.23	2.03 (1.99)	32.24 (32.21)	31.35	0.90 (0.86)	1.13 (1.15)
13mm-70m	30.26 (30.31)	31.42	1.16 (1.11)	30.81 (30.66)	28.37	2.44 (2.29)	30.71 (30.84)	29.26	1.45 (1.58)	31.50 (31.46)	30.04	1.47 (1.42)	1.61 (1.6)
19mm-70m	31.23 (31.96)	28.68	2.55 (3.28)	30.17 (29.6)	32.75	2.58 (3.15)	29.36 (28.98)	30.68	1.33 (1.70)	31.42 (31.47)	31.24	0.18 (0.23)	1.88 (2.09)

* The temperature in parenthesis represents the average temperature of plant canopy within aisle of two consecutive rows.

temperature similarities could be due to the fact that the crop canopy cover was uniform across the field including within the aisles, especially after vegetative growth is complete. The temperature similarities between data extracted from crop rows and aisles indicated that users might not focus on extracting canopy data only from crop rows at the full canopy cover stage. This approach will make spatial data analytics relatively simpler and faster. Among all treatments, the least average temperature difference of 1.13°C was observed for 13 mm at 50 m between Grd and Img. There was no significant deviation in average temperature difference values between all flights except 9 mm at 30 m, which exhibited a value of 2.4°C. This is because there was an unexpected difference between Img and Grd value at GTL1, which might be due to the presence of a hotspot primarily due to presence of much hotter bare soil surface close to GTL1. It is also important to note that canopy temperature extracted from GTL locations among different flights was comparable. These results exhibited that multiple flights over same crop area would yield consistent and robust canopy temperature response characterization. From these results, it can be concluded that appropriate camera focal length, altitude and image calibration techniques can produce a temperature map of the crop canopy with a temperature error of less than 2°C from actual canopy temperature. High-spatial and accurate canopy temperature knowledge through low altitude high-resolution imagery can potentially help users develop irrigation management decision through use of precision irrigation technologies at high-spatial resolution.

2.5 Conclusion

This study evaluated the thermal imagery obtained from different combinations of focal lengths and flight altitudes for canopy temperature sensing accuracy and various aspects of image quality. Major outcomes of this study are:

1. The appropriate selection of camera focal length and flying altitude can yield consistent and accurate canopy temperature sensing. Following the results obtained, we can conclude that a canopy temperature map of crops with a temperature error of less than 2°C from actual canopy temperature can be produced. The reliability of these results is evidenced by consistency in temperature difference values over multiple locations (GTL1-4) for an

individual flight and over a single location (GTL2) for multiple flights.

2. Further, this study revealed that temperature values extracted from imagery, representing crop rows and aisles, were not significantly different at the full canopy cover stage. This was mainly due to the crop canopy covering most of the space between two rows and creating a continuous surface of leaves. As a result, the temperature values extracted over crop rows and aisles came out nearly the same (negligible difference of less than 0.5 °C). Hence, one can use temperature values extracted from crop rows or aisles when corn is healthy and at full canopy cover stage without concern of significant canopy temperature errors.
3. The study also found that, for narrow-angle (large focal length) camera flying at low altitudes on highly dense and uniform canopy cover, image stitching software was unable to find unique features between overlapping images. This raised complications in alignment of images which resulted in unacceptable quality orthomosaics. So, users might consider caution when using a narrow-angle thermal camera at low altitude to extract corn canopy temperatures. Overall, thermal camera with 13 mm focal length flying at an altitude of 50 m provided orthomosaics which qualified for all parameters needed to develop accurate orthomosaics and extract precise canopy temperature.

In summary, low-altitude thermal remote sensing from 30 meters to 70 meters with the low, medium and wide field of view cameras was explored for a dense crop canopy. The spatial resolution and spectral discrimination-based assessment provided better insight into selection of the appropriate focal length and altitude for producing high-quality thermal imagery and precise canopy temperature sensing. It was interesting to see how the coarser spatial resolution thermal maps showed blurry differences between crop and soil background, whereas fine-resolution imagery successfully demonstrated distinct differences. The canopy temperature maps of spatial resolution ranging from 5.51 cm/pixel to 13.75 cm/pixel demonstrated that very detailed and accurate information could be extracted based on user requirements. This study also showed that we can compute differences in canopy temperature even between two adjacent rows of corn plants. It can be very helpful in quantifying canopy temperature-based indices for assessing plant water needs, such as the crop water stress index (CWSI). Thus, with this low altitude high-resolution thermal imagery it is possible to determine plant water needs even if they change from row to row, leading to very precise irrigation management. In the future, higher resolution (spatial) thermal camera needs to be developed which can potentially be used on manned planes to enhance operational efficiencies, capture higher spatial resolution imagery and to develop and implement precision irrigation management decisions.

Chapter 3 - Quantifying precise and high spatial resolution crop water stress using UAV-based thermal infrared and multispectral imagery

3.1 Abstract

Precision irrigation technology implementation is lacking due partly to the unavailability of a robust decision support system. Sensor systems and the spatial crop water stress data could potentially provide the feedback needed to develop a site-specific irrigation decision system. Therefore, the goal of this study was to 1) develop an accurate spatial thermal and multispectral map of a corn field with different irrigation treatments; and 2) derive the crop water stress index of corn using thermal and near-infrared imagery and co-relate it to real-time collected ground data representing plant stress indicators. A thermal camera (FLIR Vue Pro) with 13 mm focal length and a multispectral camera (MicaSense Rededge) were mounted on a Matrice 100 sUAS and flown at 50 m altitude over a four acres corn field divided into three irrigation levels (50%, 75%, and 100% irrigation level). Field-specific water stress baselines were developed and used in CWSI quantification to consider the effect of the instant local environment. Canopy temperature maps were generated from thermal images, then CWSI maps were created using canopy temperature and water stress baselines. The CWSI was evaluated against field-measured leaf water potential, imagery-based vegetative indices NDVI (Normalized Difference Vegetation Index), and NDRE (Normalized Difference Red Edge index) at nine sampling locations. Results showed that high-resolution precise crop water stress maps were capable of inter-row and intra-row detection of corn water stress. The vegetative indices significantly explained variation in crop water stress, with NDRE having the highest R^2 value of 0.8 and NDVI having an R^2 value of 0.7. Field-measured

leaf water potential also significantly affected water stress but showed a weaker correlation with R^2 values of 0.6. Overall results from this study showed that the combination of thermal imaging and NIR imaging could be utilized to determine accurate crop water stress on the spatial scale for irrigation water management and scheduling.

3.2 Introduction

Water is one of the most precious resources available on earth. The scarcity of water resources for irrigation management is the most concerning challenge in agriculture, especially in arid and semi-arid regions. Agriculture consumes 80–90% of the freshwater available worldwide, about two-thirds of which is used for crop irrigation [Fereres & Evans, 2006; Gerhards *et al.*, 2019). In the United States alone, 83.4 million acre-feet of water are consumed on irrigated acres annually, with corn being the crop with a maximum share of 25 % of total U.S. irrigated acres [Farm and Ranch Irrigation Survey (FRIS), 2018]. As climate change aggravates droughts and produces a risk to future water resources, it becomes imperative to use each unit of applied irrigation water for maximum production. In such conditions, the most promising solution for the sustainable management of agricultural water resources is improving agricultural water productivity. On-farm variable rate irrigation (VRI) technologies exist nowadays but need more implementation. The USDA's Farm and Ranch Irrigation Survey (FRIS) 2018 reported that most US farmers apply irrigation based on crop conditions and soil feel. Less than 15 % use moisture-sensing devices to provide the exact required water. The key objective of VRI, "more crop per drop," cannot be accomplished without a thorough knowledge of crop water status to determine appropriate irrigation rates and timing. Crop water status information over a large farmland area has great potential for optimizing agricultural water use. Quantifying plant water needs through monitoring spatial crop water stress allows the deployment of a site-specific irrigation system that can provide the exact amount of water required by plants [Shi *et al.*, 2016].

Crop water stress (CWS) induces by water shortage in plants either due to soil moisture deficit or high environmental demands [Gerhards *et al.*, 2019]. CWS causes a decrease in photosynthesis activity, stomatal conductance, leaf water content, transpiration, and leaf expansion. Based on these characteristics, CWS can be detected by measuring soil moisture content and crop physiological characteristics (e.g., stomatal conductance, leaf water potential, canopy temperature, and photosynthesis activity) [Zhang *et al.*, 2019b]. Out of all the physiological characteristics, canopy temperature is the most important and widely accepted indicator of CWS. Canopy temperature is a relatively quick-response characteristic that does not depend on plant structure or pigment changes, which take more time to develop [Khanal *et al.*, 2017]. Leaf temperature is strongly correlated to stomatal control of leaves, leaf loses water through stomata openings during transpiration, causing a drop in leaf temperature [Idso *et al.*, 1981; Jones 1999; Jones *et al*. 2002]. So, if stomatal closure happens, it will increase the canopy temperature as there will be no heat dissipation through evaporation. A healthy and transpiring leaf's temperature should be similar to the air temperature, while stressed leaves exhibit a higher temperature [Giménez *et al*.,2021; Jones *et al*., 2014; Zhang *et al.*, 2019a]. So, plants react to water stress by increasing leaf temperature and closing stomatal openings. It is for this reason that canopy temperature has become the most accepted and reliable tool for estimating plant water requirements [Awais *et al*., 2022]. Quantifying water stress using canopy temperature also requires consideration of a few environmental variables that create high environmental demands and affect leaf stomata openings. These variables include air temperature (Ta), relative humidity (RH), vapor pressure deficit (VPD), solar radiation, and wind speed.

Canopy temperature can be sensed using infrared radiometers on the ground or thermal infrared remote sensing. On-site/ground measurements are time-consuming, laborious, and costly. They omit the spatial variability of soil and crops, so they are inappropriate for time-specific and continuous crop monitoring [Han *et al*., 2021, Ndlovu *et al*., 2021]. Remote sensing-based canopy temperature measurements have the advantages of being accessible, non-destructive, having low labor intensity, and considering spatial variability. Satellite and aerial imagery have been extensively used in the past to monitor crop water stress. Satellite imagery faces challenges in monitoring CWS at the farm scale due to its coarser spatial resolution. Additionally, satellite imagery is susceptible to degradation by atmospheric factors. These factors include light absorption, scatter by clouds, variations in various particulates, aerosols, gasses, and temperatures that reduce the availability and consistency of satellite imagery [Barzin *et al*., 2020]. The accuracy and quality of thermal imagery are significantly affected by the altitude at which it is collected. The accuracy changes with the effects of the atmosphere, which increases with altitude [Heilman *et al*., 1976; Thomson *et al*., 2012]. A correction procedure had to be implemented to reduce errors generated from the atmosphere, making the process more complicated and potentially less accurate.

An Unmanned Aerial System (UAS) can reduce these limitations posed by atmospheric degradation of imagery by flying closer to ground level and excluding most atmospheric degradation effects. Images collected at lower altitudes produce more accurate canopy temperatures and can provide high spatial resolution accommodating differentiation of crop pixels from soil pixels, as compared to images acquired at higher altitudes. The unique benefits of using UAS for crop monitoring include; low cost, ease of construction, convenient transportation, quick operating cycle, increased flexibility, and high spatial-temporal resolution. These characteristics make UAS ideal for near real-time CWS monitoring with the desired resolution at a farm scale [Hussain *et al*., 2020; Sepulcre-Cantó *et al*., 2006; Ludovisi *et al.*, 2017]. Several canopy temperature-based indices have been used to monitor spatial crop water stress like, apparent thermal inertia (ATI), crop water stress index (CWSI) [Idso *et al*., 1981, Jackson *et al.*, 1981], degrees above non-stressed (DANS), degrees above canopy threshold (DACT), time temperature threshold (TTT), integrated DANS (IDANS), and integrated DACT (IDACT) [DeJonge *et al.*, 2015]. Of these indices, CWSI is the most commonly used index and there is a substantial correlation observed between CWSI and ground-based water stress indicators [Moller *et al.*, 2006; Taghvaeian *et al*., 2012; Bellvert *et al*., 2014; Gonzalez-Dugo *et al*., 2014; Pou *et al*., 2014; Taghvaeian *et al.*, 2014; DeJonge *et al*., 2015].

CWSI calculation is based on estimation of two baselines: the lower limit of the air-canopy temperature difference (non-water-stressed baseline, NWSB), which represents healthy plants, and the upper limit, which represents highly stressed plants [Awais *et al*., 2022]. These baselines can be calculated by two approaches: theoretical [Jackson *et al*., 1981] or empirical method [Idso *et al*., 1981]. The empirical method is preferred over the theoretical, as it uses only three variables (Ta, RH, and VPD), making it easier to implement. A linear relationship between the canopy-air temperature difference of healthy plants and atmospheric VPD is used as the NWSB. A constant value of canopy-air temperature difference representing stressed plants can be used as the dry reference or upper limit, which can vary from 4 ^{0}C to 10 ^{0}C, [Alves & Pereira, 2000; Cohen et al., 2005; Erdem et al., 2010; Moller et al. 2006; Wanjura et al., 2006]. NWSBs are crop and climate specific, so it becomes crucial to develop exclusive baselines when the crop or environmental conditions change. Once baselines are available, obtaining concurrent air temperature and relative humidity measurements, one can use canopy temperature from aerial imagery to estimate CWSI. Several studies have been conducted to estimate CWSI for different type of crops like, cotton [Cohen *et al*., 2015], grapevine [Bellvert *et al*., 2015, Pou *et al*., 2014, Zarco-Tejada *et al*., 2013], soybean [Crusiol *et al*., 2020], olives [Berni *et al*., 2009] apple tree [Gómez-Candón *et al*., 2016]. Using the baseline approach CWS has been estimated for Corn as well [Kar & Kumar, 2010; Payero & Irmak, 2006; Li *et al.*, 2010; Chen *et al.*, 2010; Irmak *et al.*, 2000; Zia *et al.*, 2013; Zhang *et al.*, 2023; Brewer *et al.*, 2022; DeJonge *et al.*, 2015; Zhang *et al.*, 2019b], but methods integrating ground-based baselines and high-resolution thermal imagery (centimeter-level spatial resolution) to quantify precise crop water stress are little explored for corn in the Kansas, USA region. Therefore, this study aims to:

1) Develop precise spatial thermal and multispectral map of corn fields with different irrigation treatments.
2) Develop a high-resolution spatial crop water stress index (CWSI) for corn using thermal infrared imaging from UAV and locally customized water stress baselines in Kansas, USA.
3) Evaluate UAV-based CWSI against vegetative indices from near-infrared imagery and ground data on plant stress indicators.

3.3 Materials & Methods

3.3.1 Experimental Setup

This study was conducted on four-acre corn fields at the Kansas Research Valley experiment field (39.076076° N, -95.768777° W), Silver Lake, Kansas, USA, during 2020 and 2021. Experiment fields used for both years were adjacent (Figure 3.1) and had Eudora Silt Loam soil type. Corn was planted on 22 April 2020 and 15 April 2021 with a row direction from west to east. Each year, the whole field was divided into three equal parts, and a unique irrigation level was assigned to each part to measure canopy temperature under different stress conditions. Irrigation levels were: (a) Well watered, where irrigation was provided to fulfill 100% of the water requirement (ii) Slightly water deficient, where 75% of required water was provided (iii) Stressed, where irrigation to replace 50% of water requirement was provided to generate significant water stress in plants. For the 2020 season, the north part of the field was assigned to 50% irrigation, followed by 75% irrigation to the center part and 100% irrigation to the south part. For the 2021 season, 50% irrigation treatment was provided to the south part of the field, and 75% irrigation treatment was applied to the center part. But due to the high soil electric conductivity (EC), this field part turned out to be the healthiest one, even healthier than the 100% irrigation part on the north side of the

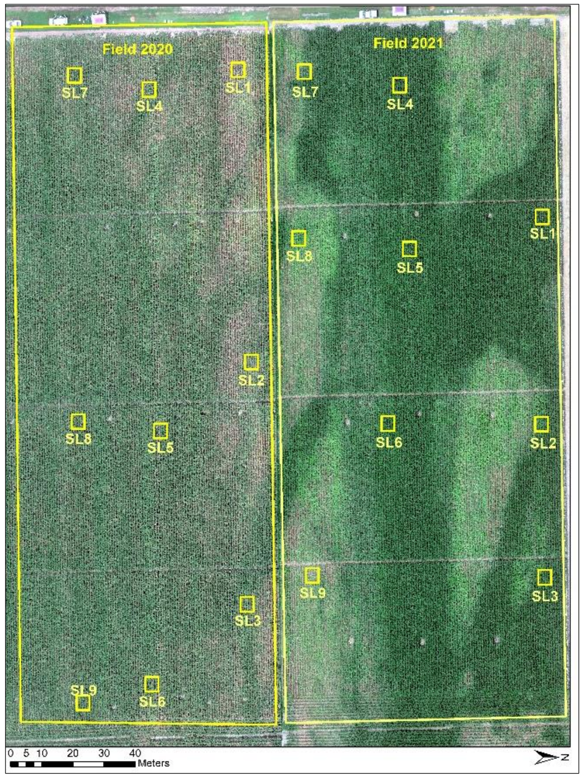

Figure 3.1. RGB orthomosaics of the experiment fields and sampling location's layout for years 2020 and 2021

field. Three sampling locations for each irrigation treatment were selected randomly to collect ground data and compare it with imagery-based data, as shown in Figure 3.1. Irrigation management of the entire corn field was carried out by a professional agronomist working at the research experiment field using soil moisture probes. The irrigation treatments were applied when the crop reached a stage (V9-V10) where water deficiency cannot result in permanent damage to plant growth or death of the plant.

3.3.2 Airborne imaging system

A quadcopter (Matrice 100, Shenzhen DJI Sciences and Technologies Ltd.) was used for aerial imagery collection (Figure 3.2). The quadcopter has a payload capacity of 1 kg with a maximum flight time of 40 minutes. FLIR Vue pro-Thermal Infrared sensor (FLIR Systems, USA) of focal length 13mm was used for thermal infrared imaging. The camera was an Uncooled Vox Microbolometer thermal imager with a 640 x 512 pixels resolution. The spectral response was in the 7.5 – 13.5 µm range, and images were collected in 14-bit tiff format. Thermal images were captured in 14-bit tiff format to avoid autocorrection (applied by the camera in other formats) and to get image pixels representing a closer estimate of actual radiance differences from the target. The thermal camera was calibrated using surface temperature measurements to ensure measurement accuracy. For multispectral imaging, MicaSense Red-edge camera (MicaSense, Inc., WA, USA), which records spectral response in 5 different spectral bands - blue, green, red, red-edge, and near-infrared, was used. Multispectral imagery was calibrated to consider the lighting conditions during the imagery acquisition period using a calibration panel provided by the camera manufacturer. Images of the calibration panel were taken before and after the flight and used later in image processing.

For each imaging sensor, UAV was flown at 50 m altitude at a speed of 3 m/s based on results from our previous study [Gadhwal *et al.*, 2022]. Four flights were conducted each year during the study period (2020-2021), and the best two representing the clear sky days were selected for further analysis. UAV flight missions were prepared using Mission Planner; a fixed route of waypoints was designed considering the front and side overlap percentage between consecutive images, the camera’s focal length, and flying altitude. All flights' front and side direction overlap was around 85%. As the mission planner recommended, images were obtained after every second for both cameras to suit the image-stitching process. Mission Planner was not directly compatible with the UAV, so a compatible software platform (Litchi, VC Technology Ltd) was used to transfer missions from Mission Planner to the UAV. Thermal images were geotagged using a separate module and GPS unit (PixHawk, 3DR). Multispectral images were geotagged using the integrated

Figure 3.2. Aerial imaging system used in the study

GPS unit with the camera. The sensors were mounted facing straight downwards during normal aircraft flight attitude. Flights were conducted close to solar noon because before and after solar noon, plants exhibit shadows on the side, creating errors in imagery.

3.3.3 Ortho-mosaicking

Each UAV flight generated hundreds of images, which were converted into an orthomosaic, representing the whole experiment area, using Metashape Professional by Agisoft (Agisoft LLC, St. Petersburg, Russia). Raw images were geotagged using standard GPS, with an accuracy of approximately 2 meters. This low geometric positioning accuracy is a source of error in overlaying different orthomosaics and comparing measured ground data with imagery-extracted data. So, to generate orthomosaics with centimeter-level positioning accuracy, ground control points (GCPs) and high-accuracy Real-Time Kinematic (RTK) corrected coordinates of these GCPs were used. GCPs used were black and white painted plastic sheets of 2 feet x 2 feet; 16 GCPs were placed, covering the whole field symmetrically. Two Topcon GR-5 (Topcon, Tokyo, Japan) GNSS receivers were used, one as a base station and another as a moving rover, to collect RTK coordinates of the center of GCPs. Blurred images and images from turns were removed from the data set. Then the remaining images were converted into a mosaic using Agisoft's standard

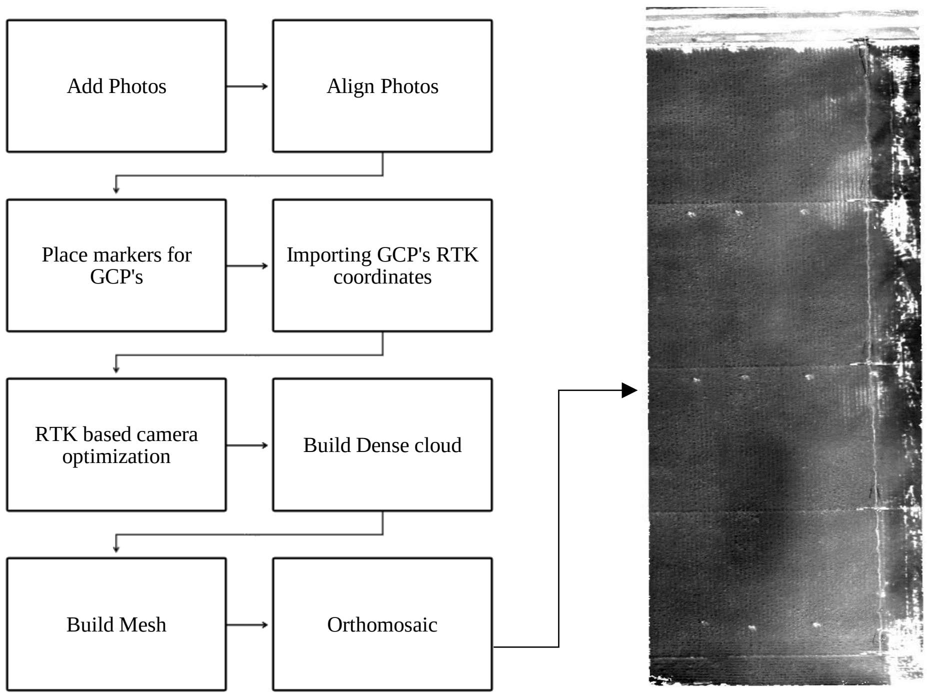

Figure 3.3. Agisoft's workflow for Ortho-mosaicking using RTK coordinates of GCPs

workflow (Figure 3.3). The final product from Agisoft was an orthomosaic with cm-level accuracy. Two types of ortho mosaics were generated: thermal and multispectral. Thermal orthomosaic was a single-band mosaic, representing irradiance values of objects and multispectral mosaic was a 5-band mosaic demonstrating reflectance response in 5 different bands, separately.

3.3.4 Measurement of maize canopy temperature and empirical CWSI calculation

Three (IRs) infrared radiometers (model SI-111; Apogee Instruments, Inc., Utah, USA) were installed in the field during the 2021 crop season, one in each irrigation treatment. IRs were always kept 3 feet above the crop canopy, aiming vertically downward, i.e., nadir view as shown in Figure 3.4. Canopy temperature (T_c) was sensed each minute and recorded after every 5 minutes to an attached data logger. It was ensured that 100 % of the temperature signal came from leaves by measurement of several leaf temperatures with a hand-held Flir TG167 Spot Thermal Camera (Flir Systems Inc, Wilsonville, OR, USA) and with an additional visual inspection. A similar instrumental setup was used in previous studies [Payero & Irmak, 2006, Bellvert *et al*., 2014 and Zhang *et al*., 2019] to measure infield canopy temperature over the entire season. Along with the canopy temperature, several weather parameters were recorded at an automated Campbell CR10x weather station installed adjacent to the research field, including air temperature (T_a), relative humidity (RH), net solar radiation, and wind speed. The weather data acquisition interval was 5 min, matching the canopy temperature data interval. The canopy temperature and meteorological data were collected from the crop growth stage V10-V12 (where the canopy significantly covered the gap between rows) to the maturation stage. With season-long data of canopy temperature and weather parameters, crop water stress baselines were developed, and eventually, empirical crop water stress index (CWSI) was calculated using these baselines in the following equation:

$$\mathrm{CWSI} = \frac{(\mathrm{Tc}-\mathrm{Ta})_{\mathrm{m}} - (\mathrm{Tc}-\mathrm{Ta})_{\mathrm{LL}}}{(\mathrm{Tc}-\mathrm{Ta})_{\mathrm{UL}} - (\mathrm{Tc}-\mathrm{Ta})_{\mathrm{LL}}} \quad (1)$$

Where $(T_c\text{-}T_a)_m$ is the actual measurement of canopy- air temperature difference; $(T_c\text{-}T_a)_{LL}$ is the lower limit of the air-canopy temperature difference, and $(T_c\text{-}T_a)_{UL}$ is the upper limit of air-canopy temperature difference. The non-water stressed baseline (NWSB) or $(T_c\text{-}T_a)_{LL}$ was quantified using linear relation between the T_c - T_a of well-watered canopy and vapor pressure deficit (VPD), a similar procedure implemented by [Payero & Irmak, 2006, Zhang *et al*.,2019, Taghvaeian *et al*., 2012]. VPD was calculated using the standard equation consisting of RH and T_a:

$$VPD = 0.6108\, X \exp\left(\frac{17.27Ta}{Ta+237.3}\right) X \left(\frac{100-RH}{100}\right) \quad (2)$$

Values of well-watered canopy-air temperature difference ($T_c - T_a$) in units of ^{0}C were regressed against VPD in units of Kpa for the whole season. Each data point used in the regression was the 5-minute average of the T_c, T_a, and VPD; a total of 4312 data points were acquired for the 2021 crop season. The resulting linear regression equation was used as NWSB.

$$\text{NWSB or } (T_c\text{-}T_a)_{LL} = a + b*VPD \qquad (3)$$

This equation can be used for multiple years if the crop and location are kept the same; in our study, we used this equation from 2021 for calculating CWSI for the 2020 season, as field location

Figure 3.4. Infrared radiometer installed over corn canopy in the field

and crop was the same. For NWSB calculation, canopy temperatures and weather parameters were used from 08:00 to 18:00 h of the day and only when wind speed was below 4 m/s. Using temperature values from early morning, late evening, and windy days is not recommended because it can generate errors in the baseline calculation. The upper limit of air-canopy temperature difference $(T_c\text{-}T_a)_{UL}$ represents $(T_c\text{-}T_a)$ of plants when transpiration almost ceased, i.e., highly stressed plants. This upper limit is generally observed to be constant, and a dry reference temperature based on canopy temperature from the stressed crop was used for this upper limit

[Ehrler *et al*., 1978, Irmak *et al*., 2000, Cohen *et al*., 2005 Mangus *et al*., 2016]. Using VPD values for specific flight times and days, NWSB for every flight was calculated separately. These values of NWSB and a constant upper limit were then used in equation (1) to calculate the final linear relationship between $(T_c\text{-}T_a)_m$ and CWSI for each flight, which was further used to generate CWSI maps.

3.3.5 Spatial mapping of canopy temperature, CWSI, and vegetative indices

Thermal and multispectral orthomosaics generated from Agisoft represent the response of target objects in the respective bands. To extract useful and easy-to-interpret properties of the crop, such as canopy temperature, crop water stress, crop canopy greenness, or chlorophyll content, these orthomosaics were converted into different kinds of spatial maps. The thermal orthomosaics

Figure 3.5 Calibration panels used to generate surface temperature map: Black, gray, white, and water panel

were converted into the crop canopy surface temperature map using four calibration panels, as shown in Figure 3.5. These panels were used as the cold and hot references for thermal imaging, a water- covered white-painted panel represented the coldest pixels, and the black-painted wooden panel represented the hottest pixels. White and gray panels were the references for increasing temperature from cold to hot reference, respectively. Temperatures of these panels were measured during the UAV flight, within 45 seconds of the UAV passing over the panels, using Flir TG167 Spot Thermal Camera (Flir Systems Inc, Wilsonville, OR, USA). The same panels' pixel values/ digital numbers were extracted from the thermal mosaic and regressed against the recorded panel temperatures. The resulting linear equation was then used to convert the thermal orthomosaic into a surface temperature map in ArcMap 10.6.1 (ArcGIS, ESRI, Redlands, CA, USA) using the Raster Calculator tool. These temperature maps were further converted to the CWSI maps using the already determined relationship between $(T_c\text{-}T_a)_m$ and CWSI for each flight using the Raster Calculator tool. For the $(T_c\text{-}T_a)_m$ calculation, the canopy temperature orthomosaic (".tiff" file) was used in place of T_c, and average air temperature during the flight was used for T_a.

Water stress hinders photosynthesis activity in plants and consequently affects the greenness and chlorophyll content of the leaves. To quantify these canopy-related changes with change in water stress, two kinds of vegetative indices were derived from the multispectral orthomosaic- NDVI (Normalized Difference Vegetation Index) and NDRE (Normalized Difference Red Edge index). NDVI assesses the greenness of crop canopy and crop vigor. NDRE is useful in measuring the chlorophyll content in plant leaves. The band combination used to calculate NDRE makes it especially sensitive to changes in chlorophyll contained within the leaves. Out of the different bands available in multispectral orthomosaics, specifically required bands were used in the Raster calculator to map the vegetative indices of crop canopy.

$$NDVI = \frac{(\text{NIR} - \text{RED})}{(\text{NIR} + \text{RED})} \tag{4}$$

$$NDRE = \frac{(\text{NIR-RE})}{(\text{NIR+RE})} \tag{5}$$

Where RED, NIR, and RE represent reflectance in the red, near-infrared, and red-edge bands, respectively, obtained from multispectral images. NDRE values range from -1 to +1. Theoretically, NDRE values lower than 0.3 can be interpreted as a tell-tale sign of an unhealthy or stressed plant, and very low values could also stand for bare soil. NDRE values from 0.3 to 0.6 belong to mildly stressed plants, and values from 0.6 to 1 indicate very healthy crops [Ndre Index, 2019]. NDVI values range from -1 to +1; sparse vegetation cover or the crop where canopy cover is not dense due to high water stress or simply an unhealthy plant is represented by moderate NDVI values ranging from 0.2 to 0.5. High NDVI values >0.6 indicate the presence of dense and healthy vegetation, like crops at their peak growth stage [Gidey *et al*., 2018].

3.3.6 Ground data collection

The crop water stress obtained from aerial imagery was evaluated against a plant-based water stress indicator, leaf water potential (LWP). LWP (in units of Bar) was measured using a Scholander pressure chamber (PMS Instrument Company, Albany, OR, USA), as shown in Figure 3.6, following a similar procedure as discussed in [Turner & Long, 1980]. LWP measurements were taken at three sampling locations (SL) per irrigation level right after the aerial thermal image acquisition. Each sampling location was bounded in a 4ft x 5ft box and was geo-referenced with a

Figure 3.6 Scholander pressure chamber in the field for leaf water potential

highly accurate Topcon GR-5 RTK positioning system. One leaf per plant and three different plants were selected for each location to measure LWP. The ground data was collected in the closest possible time frame to UAV flights to have relevancy with imagery.

3.3.7 Data extraction from orthomosaics and analysis

Pixel values associated with sampling locations were extracted from CWSI, NDVI, NDRE, and temperature maps by manually selecting pixels representing pure canopy, as shown in Figure 3.7. Polygon masks bounding only crop canopy were generated in ArcMap using RGB/digital

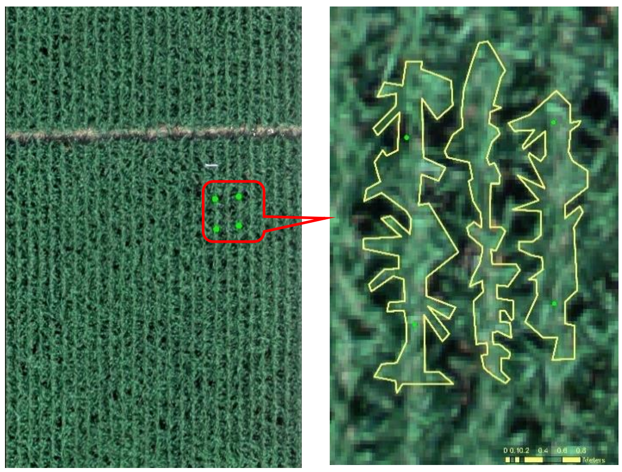

Figure 3.7 Manual selection of pixels representing pure canopy

orthomosaic and then overlaid over other maps for data extraction. As each orthomosaic had centimeters level positioning accuracy, there were negligible chances of error in overlaying masks on different data layers. Values of various parameters were compared at nine sampling locations. Linear regression analysis was performed using SAS® to test the significance and strength of the relationship between CWSI, vegetative indices, and ground data for each flight.

3.4 Results and Discussion

3.4.1 Non-Water-Stressed Baseline (NWSB) and CWSI estimation

Values of canopy-air temperature difference ($T_c - T_a$) in units of ^{0}C were regressed against VPD in units of Kpa for Non-Water-Stressed Baseline calculation. Each data point represents T_c,

T_a, and VPD collected at 5 min intervals from a well-watered zone. A linear regression model was fitted to the data to quantify this relationship. P-value of <0.0001 from linear regression analysis (Figure 3.8) showed that ($T_c - T_a$) was significantly affected by VPD with an R^2 value of 0.65. ($T_c - T_a$) was linearly decreasing with increase in VP, as shown in equation 6. Similar results of NWSB

$$(T_c - T_a) = -1.39617(VPD) + 1.27784 \qquad (6)$$

were observed in some previous studies [Payero & Irmak, 2006, Zhang *et al*., 2019, Taghvaeian *et al*., 2012 and Mangus *et al*., 2016]. This equation further will be referred as Non-Water-Stressed

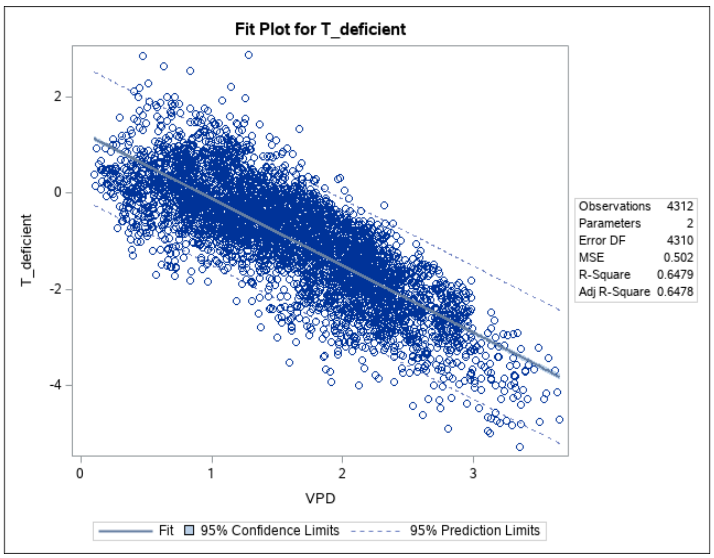

CWSI Data

The REG Procedure
Model: MODEL1
Dependent Variable: T_deficient

Number of Observations Read	4312
Number of Observations Used	4312

Analysis of Variance

Source	DF	Sum of Squares	Mean Square	F Value	Pr > F
Model	1	3981.33582	3981.33582	7931.35	<.0001
Error	4310	2163.51159	0.50197		
Corrected Total	4311	6144.84740			

Root MSE	0.70850	R-Square	0.6479
Dependent Mean	-0.97495	Adj R-Sq	0.6478
Coeff Var	-72.67088		

Parameter Estimates

Variable	DF	Parameter Estimate	Standard Error	t Value	Pr > |t|
Intercept	1	1.27784	0.02750	46.47	<.0001
VPD	1	-1.39617	0.01568	-89.06	<.0001

Figure 3.8 Relationship between T_c -T_a and VPD for non-water-stressed baseline (NWSB) quantification

Baseline (NWSB). The upper limit of air-canopy temperature difference used was a dry reference of 8 °C above air temperature based on canopy temperature from the stressed crop only.

Table 3.1 CWSI equations for individual flights

Flights	8/4/2020	8/18/2020	8/06/2021	8/17/2021
CWSI Equation	CWSI= $\frac{(Tc-Ta)m + 0.875}{8.88}$	CWSI= $\frac{(Tc-Ta)m + 0.857}{8.86}$	CWSI= $\frac{(Tc-Ta)m + 0.977}{8.977}$	CWSI= $\frac{(Tc-Ta)m + 1.137}{9.137}$

Using NWSB and upper limit, the final relationship between $(T_c - T_a)_m$ and CWSI for each UAV flight date was determined, presented in Table 3.1. These equations were further used to convert temperature orthomosaics into CWSI maps.

3.4.2 Crop water stress and vegetative indices maps

To assess the variability of crop water stress and crop health throughout the 4-acre corn field for years 2020 and 2021, spatial maps of the CWSI, canopy temperature, NDRE, and NDVI

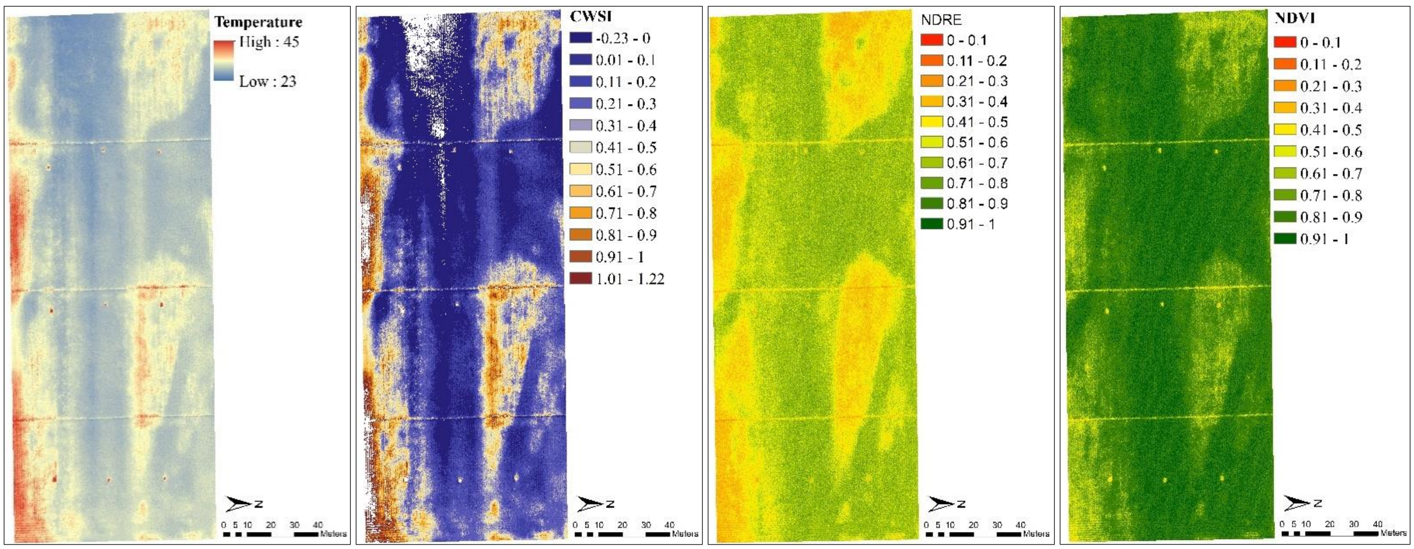

Figure 3.9 Spatial maps of the whole field on 08-06-2021: (a) Canopy Temperature (b) CWSI (c) NDRE (d) NDVI

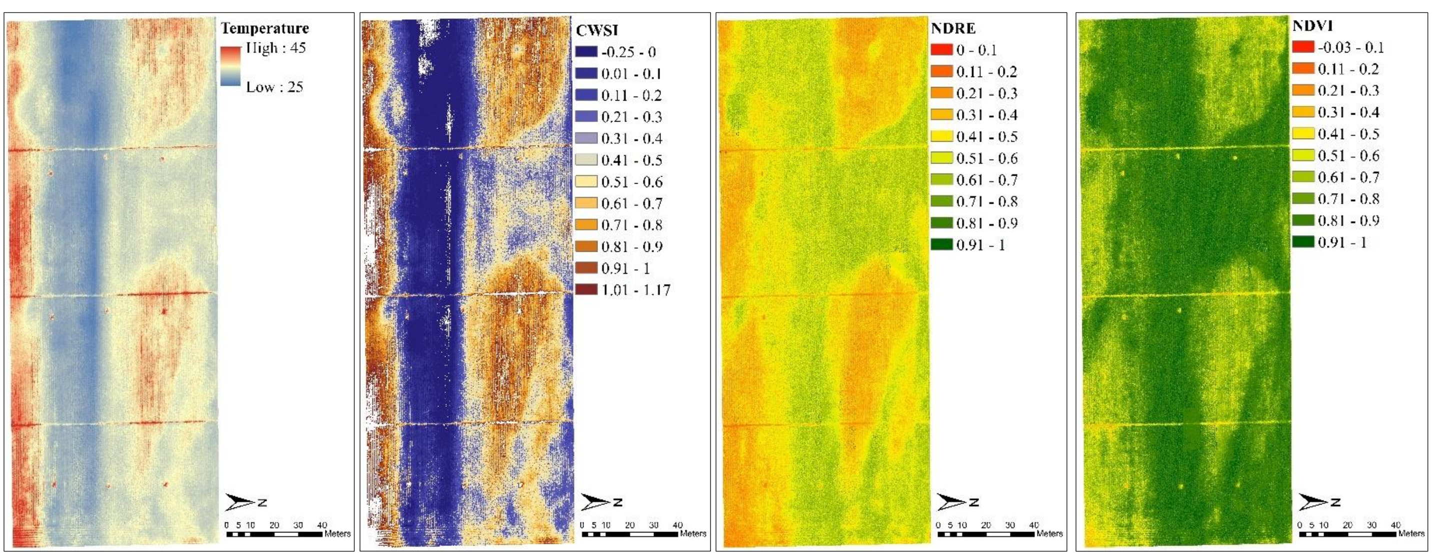

Figure 3.10 Spatial maps of the whole field on 08-17-2021: (a) Canopy Temperature (b) CWSI (c) NDRE (d) NDVI

were developed as shown in Figures 3.9, 3.10, 3.11 and 3.12. During the data collection crop was in the late reproductive and maturation stage. For better visualization, all maps were classified in green to red color scheme, where the healthier canopy (having low temperature, low CWSI, high NDVI and NDRE values) was represented by green color, and the stressed canopy (with high temperature, high CWSI, low NDVI and NDRE values) was represented by red color. Maps are provided with a legend where we can see values associated with the respective parameter, a north-direction arrow at the bottom, and a scale bar in meters to visualize distances. It can be noticed from the field maps on 08-06-2021 that the regions along the south boundary and two major regions on the northwest and center-north boundary (red spots) of the field were with low water availability to plants and represented water-stressed conditions. These regions have high-temperature values, majorly from 35 ^{0}C to 40 ^{0}C and CWSI values >0.6 associated with them, which should be the case for stressed canopy. Similar results showed by vegetative indices maps where NDRE<0.4 and NDVI<0.68 values, indicating the presence of unhealthy crops. The healthiest part of the field was the center strip and two small regions near the north boundary, represented by lush green color. These regions have canopy temperature values <30 ^{0}C, CWSI<0.3, NDRE>0.6, and NDVI>0.8, which strongly indicates a healthy crop. On 08-17-2021, the field was under higher water stress than on 08-06-2021. This resulted in the slight shrinking of healthier regions and expansions of water-stressed regions, but the pattern was almost similar to the earlier date data. The stressed regions have temperature values from 36 ^{0}C to 42 ^{0}C and have CWSI >0.6, NDRE<0.4, and NDVI<0.64. The healthier canopy on this date had canopy temperature values less than 34 ^{0}C; other parameters were; CWSI<0.3, NDRE>0.6, and NDVI>0.8. For the 2020 season, water stress variability across the field was not as good as in the 2021 data. The only stressed regions were nearby the west boundary of the field and a few along the north boundary of the field, as shown in maps for 08/18/2020 in Figure 3.11. For these regions, canopy temperature values were ranging from 32 ^{0}C to 36 ^{0}C, CWSI values were >0.7, and NDRE values were noticed <0.35 with NDVI values <0.6. The rest majority of the plants in the field were barely stressed or were in good health. For the healthy plants, the temperature was less than 30 ^{0}C with CWSI values

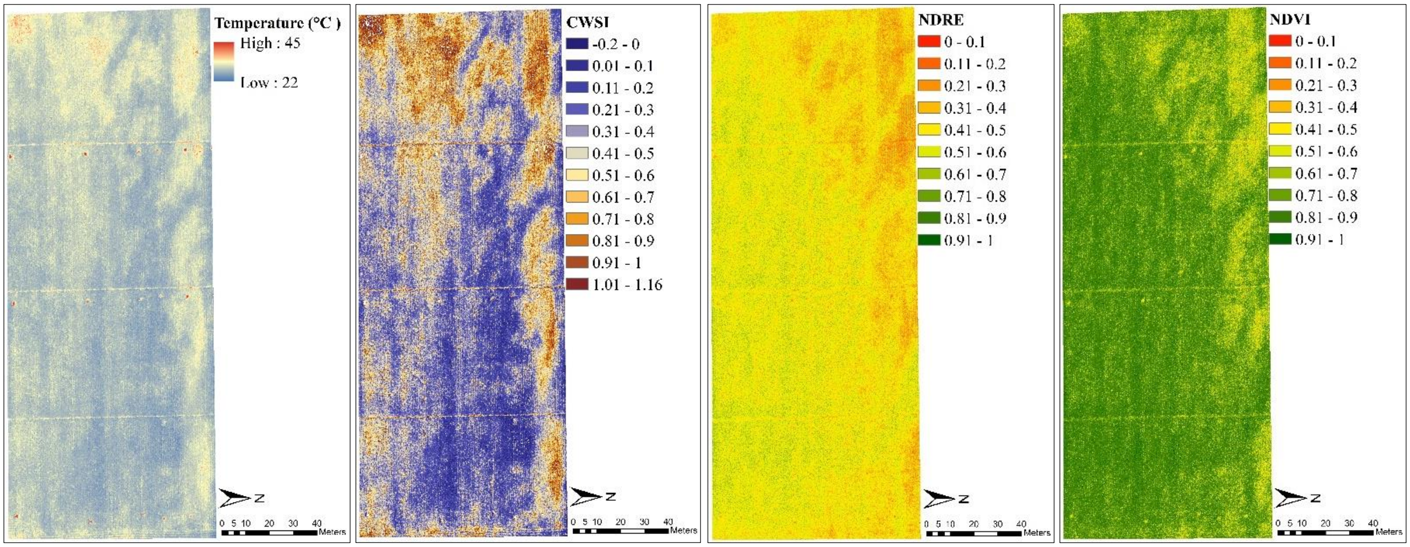

Figure 3.11 Spatial maps of the whole field on 08-18-2020: (a) Canopy Temperature (b) CWSI (c) NDRE (d) NDVI

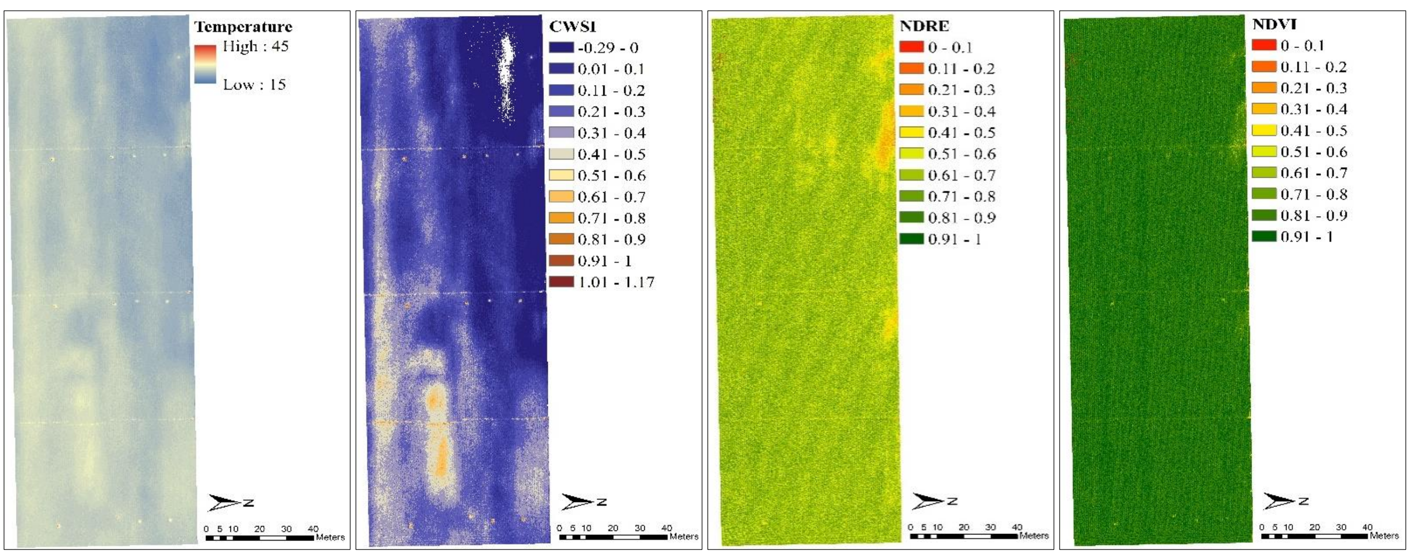

Figure 3.12 Spatial maps of the whole field on 08-04-2020: (a) Canopy Temperature (b) CWSI (c) NDRE (d) NDVI

not exceeding 0.5 and NDRE values greater than 0.46 with NDVI>0.7. On 08/04/2020, plants were very healthy and barely stressed. NDRE and NDVI maps in Figure 3.12 show that the values across the entire field were uniform. The majority of NDVI values were greater than 0.8 with NDRE greater than 0.6. For most regions of the field, temperature values did not go beyond 30 ^{0}C and the crop water stress index was also below 0.5, a clear indication of a uniformly healthy crop and the absence of water stress. To visualize how a water-stressed crop behaves differently from a healthy one, a comparative analysis was performed between a water-stressed crop from 08/17/2021 and a crop with minimum or no water stress from 08/04/2020. Canopy temperature, CWSI and NDVI values for the entire 4-acre field were plotted as shown in Figure 3.13. The number of pixels associated with a specific parameter value was on the y-axis and the actual measurement of the parameter was on x-axis. It can be noticed that non-water stressed crop has temperature values spread over a very narrow span, from 19 ^{0}C to 30 ^{0}C and a sharp peak at 25 ^{0}C. In contrast, the stressed field temperatures spread over a wider span of 25 ^{0}C to 47 ^{0}C, a mix of both lower temperature values representing healthy plants and higher temperature values representing stressed

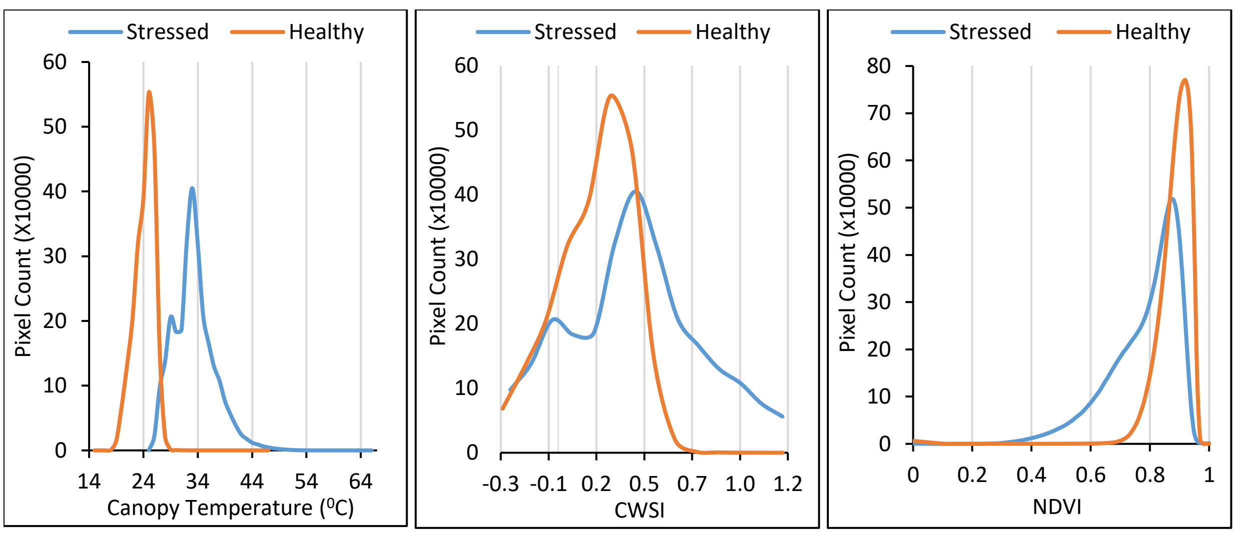

Figure 3.13 Entire field-level comparison between a highly stressed (08/17/2021) and a healthy crop (08/04/2020)

plants. CWSI values for non-water stressed data were not exceeding 0.6 and have a narrow spread. In contrast, for stressed data, CWSI spread was from minimum to maximum values, and a significant part of the field went beyond 0.6 to the maximum value of CWSI, representing stressed plants. For non-water stressed crop, NDVI values were going from 0.7 to 1, associated with healthy plants. Whereas NDVI values for the water-stressed crop ranged from 0.4 to 1, including regions with lower NDVI values where plants were stressed. Water stress in plants hinders photosynthesis activity and lowers the chlorophyll content, resulting in low NDRE and NDVI values. The presence of low NDVI and NDRE values in stressed regions from CWSI maps shows the sensitivity and accuracy of CWSI maps developed in this study to detect water-stressed plants over a 4-acre corn field at full canopy coverage stage.

3.4.3 Crop water stress variation across sampling locations

For further rigorous evaluation of the imagery-based water stress, it was evaluated against NDRE and ground-based water stress indicator (LWP) at nine different sampling locations across the field. The LWP value assigned to a single location is the average value of the three LWP measurements made at that location. CWSI and NDRE values representing a single sampling location are the average value of all the selected crop canopy pixels of the respective parameter at that location. The graphs in Figure 3.14 and Figure 3.15 show these mean values of CWSI, NDRE from imagery, and LWP at the nine sampling locations in the field. For the 2021 season, sampling locations 7,8 and 9 represent 50% irrigation treatment and are, in general highly stressed regions. Locations 4,5 and 6 are from 75% irrigation, but due to the high soil electric conductivity (EC), this part of the field turned out to be the healthiest one, even healthier than the 100% irrigation (locations 1,2 and 3). Looking at the data from 08/06/2021 in Figure 3.14, locations 1-6 had no water stress, therefore showing high NDRE values around 0.6 and low LWP of 8 Bar with CWSI values lower than 0.3. Whereas locations 8 and 9 were highly water-stressed, having CWSI values of 0.7 and 0.9, LWP values of 13.8 Bar and 16.5 Bar, respectively. NDRE values for these locations were low, 0.42 and 0.35, respectively. Location 7 was mildly water-stressed as compared to locations 8 and 9, it has NDRE value of 0.53 and CWSI value of 0.25, but LWP data was surprisingly high as 16 Bar. The dataset from 08/17/2021 showed that locations 4,5 and 6 were least stressed, followed by locations 1,2 and 3 as mildly stressed, and locations 7,8 and 9 as highly

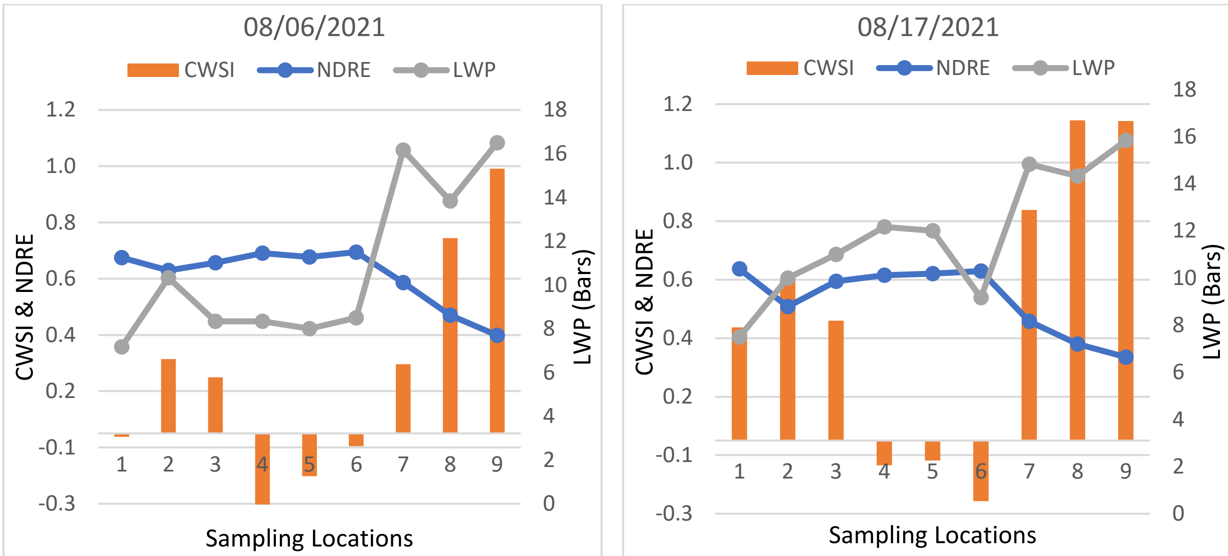

Figure 3.14 Mean values of CWSI, NDRE (left axis), and LWP (right axis) at 9 sampling locations (x-axis)

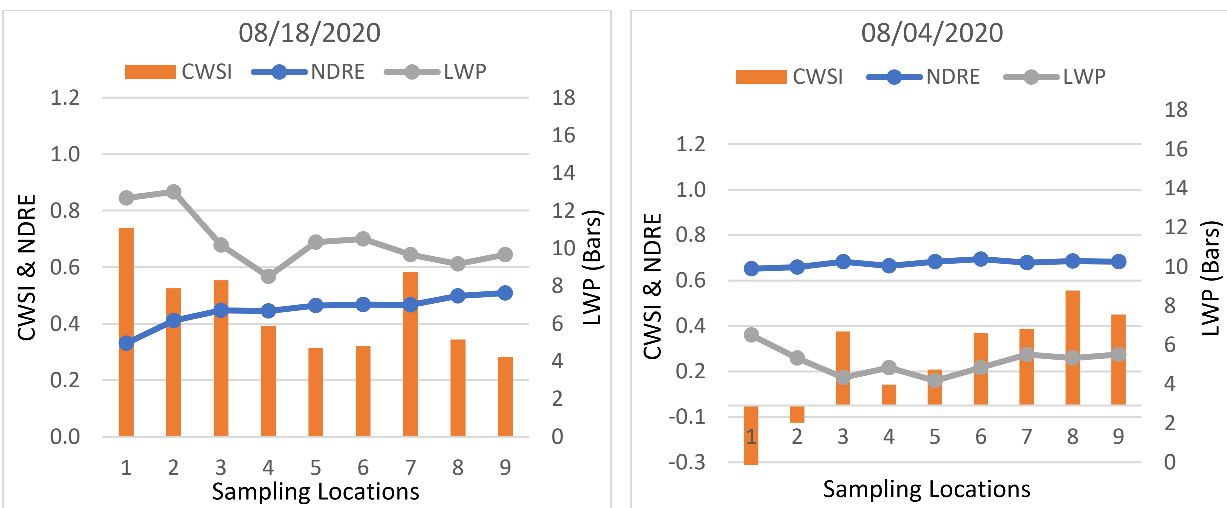

Figure 3.15 Mean values of CWSI, NDRE (left axis), and LWP (right axis) at 9 sampling locations (x-axis)

stressed. Highly water-stressed locations showed high values of CWSI and LWP and low values for NDRE, which can be seen in Figure 3.14. For the 2020 season, locations 1,2 and 3 belong to 50% irrigation, and 7,8 and 9 are from 100% irrigation. But soil EC at location 7 was low so behaving slightly similar to the 50% irrig at stressed locations (1,2,3 and 7) and just opposite scenario at healthy ation region. In general, high values of CWSI and LWP with low values of NDRE can be seen locations (4,5,6,8 and 9) from 08/18/2020 data in Figure 3.15. Field level spatial maps and Figure 3.13 already made it evident that on 08/04/2020 crop was under very mild stress or almost no water stress. As a result, uniform NDRE values of 0.6 were observed at all 9 locations, and CWSI values for most locations were lower than 0.4. Ground-based LWP also demonstrated no water stress conditions by having values below 6.5 Bar at all locations. After analyzing four datasets over the span of two years, it can be seen that imagery-derived water stress demonstrated the expected behavior aligning with crop health and ground-based water stress. Hence it can be derived that aerial thermal imaging-based crop water stress is capable of precisely differentiating water-stressed plants and healthy plants.

3.4.4 Correlations analysis

To quantify the relationship between CWSI and the rest of the parameters (NDRE, NDVI, and LWP) at sampling locations, a significance assessment of the influence of respective parameters on CWSI were provided. The relationship between CWSI and vegetative indices was negatively linear. For both data sets from 2021, linear regression analysis was performed; results are shown in Table 3.2. NDRE significantly affected CWSI, (p-value <0.0001) and showed a strong correlation with R^2 value greater than 0.8. Whereas the NDVI showed a comparatively weaker correlation but still significantly affected CWSI (p-value <0.0001) with an R^2 value of 0.7. Ground-collected LWP also significantly affected CWSI, with a p-value of <0.0001 for 08/06/2021 and a p-value of 0.001 for 08/17/2021. But this correlation was not as strong as it was for vegetative indices; the R^2 value for the 08/06/2021 data was 0.601, and 0.356 for the 08/17/2021 data. For the 8/18/2020 data, NDRE and NDVI were significantly affecting (p-value <0.0001) CWSI with a similar strong correlation having R^2 value of 0.67, LWP also significantly affected CWSI with a p-value of 0.025 but not a really strong correlation (R^2 = 0.19). As the crop was not under water stress on 08/04/2020, causing very low variability in CWSI and vegetative indices. There was not a significant effect of LWP on CWSI (p-value = 0.07) for this data, and NDVI also showed a very weak correlation (R^2 =0 .27). But NDRE was able to perform better and was strongly correlated with CWSI (p-value<0.0001 and R^2 = 0.57). The reason NDRE outperforms NDVI in terms of explaining variability in CWSI can be the better distinguishing power of the Red-Edge band to chlorophyll content/photosynthesis activity compared to the red band. The ground data in terms of

Table 3.2 Coefficient of determination (R^2), root mean square error (RMSE) and p-value for CWSI vs NDRE, NDVI and LWP

Flight Date	Parameters	R^2 (n=27)	RMSE	p-value
08-06-2021	CWSI vs NDRE	0.899	0.123	<0.0001
	CWSI vs NDVI	0.715	0.207	<0.0001
	CWSI vs LWP	0.601	0.244	<0.0001
08-17-2021	CWSI vs NDRE	0.81	0.211	<0.0001
	CWSI vs NDVI	0.699	0.266	<0.0001
	CWSI vs LWP	0.356	0.388	0.001
08-18-2020	CWSI vs NDRE	0.665	0.091	<0.0001
	CWSI vs NDVI	0.678	0.089	<0.0001
	CWSI vs LWP	0.186	0.142	0.025
08-04-2020	CWSI vs NDRE	0.570	0.162	<0.0001
	CWSI vs NDVI	0.265	0.211	0.006
	CWSI vs LWP	0.128	0.230	0.067

*Data with significant crop water stress is highlighted in yellow, and non-water stressed data is in green

LWP significantly affected CWSI for most of the data, but sometimes it showed a weaker correlation which was not the case with vegetative indices. There can be a major reason for that, as vegetative indices and CWSI were measured remotely and had the same environmental condition between crop and imaging sensors, resulting in similar variations in the measurements.

Also, the value assigned to a single replication for these parameters was the average of multiple pixels of canopy coming from several plants; three replications per location were used. Whereas LWP was measured on the ground using one leaf at a plant and three replications for a single sampling location. So, an important factor of a specific leaf's health and fewer numbers of data points to average out the variation in ground data can be a potential reason for this not-so-strong correlation.

3.5 Conclusion

This study demonstrated the capability of high-resolution airborne thermal imagery to detect crop water stress in a corn field comprising three irrigation levels. Spatial maps were

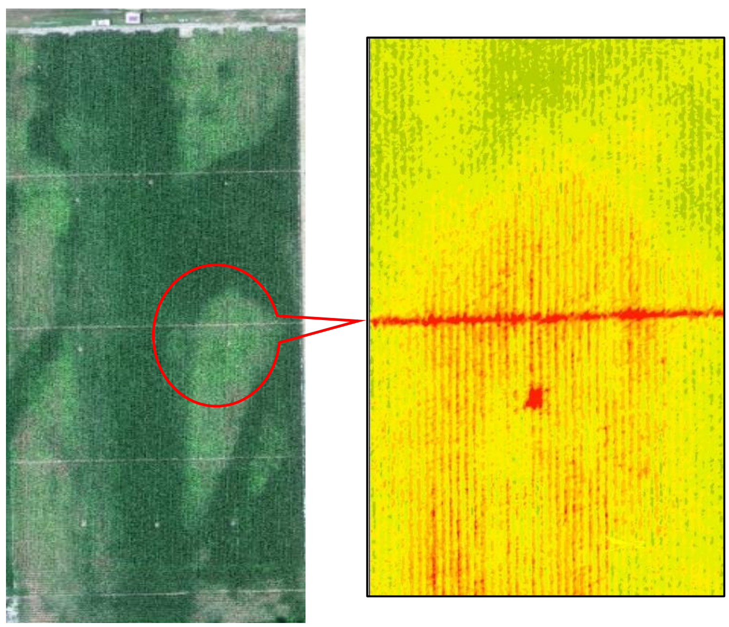

Figure 3.16 RGB orthomosaic of the corn field and zoomed in CWSI map for inter-row and intra-row visualization

generated for an established index, CWSI, to detect water stress. Field-specific non-water stress baselines for corn were developed and incorporated in CWSI map generation to consider the effect of instant local air temperature and relative humidity on canopy temperature. This is a much-needed component for precise water stress quantification. The CWSI maps were evaluated against field-measured leaf water potential and imagery-based vegetative indices (NDRE, NDVI), which allow for variations of structural and chlorophyll content of the canopy. From the results, it can be derived that high-resolution precise crop water stress maps were capable of inter-row and intra-row detection of water stress for corn (Figure 3.16), which further can be used in robust site-specific irrigation management. The vegetative indices significantly explained variation in crop water stress, with NDRE having the highest R^2 values, around 0.8 and NDVI having R^2 values around 0.7. Field-measured leaf water potential also significantly affected water stress but showed a weaker correlation with R^2 values of 0.2, 0.4, and 0.6 for three different datasets. It’s critical to notice that NDRE showed more sensitivity as compared to NDVI to variability in chlorophyll content resulted from water stress. Its possible due to the better distinguishing power of the Red-Edge band to chlorophyll content/photosynthesis activity than the red band.

Chapter 4 - Feasibility and accuracy assessment of UAV, Aircraft, and Satellite-based remote sensing for crop canopy temperature and crop health mapping

4.1 Abstract

Spatial information on plant-water requirement is the most crucial input for designing an efficient site-specific irrigation system. In quantifying this spatial information, canopy temperature-derived crop water stress maps could provide a potential solution. With the support of modern, advanced, and cost-effective remote sensing platforms like Unmanned Aerial Vehicle (UAV), aircraft, and Satellite, remote sensing data can be systematically collected with varying degrees of efficiency for spatial water stress assessment. However, each of these platforms provides remote sensing data at varying degrees of spectral and spatial resolutions, which can impact the user's ability to develop spatial water stress maps and implementation of precision irrigation systems. Therefore, the main goals of this study were 1) to assess the feasibility and accuracy of UAV, aircraft, and satellite-based imaging for crop water stress quantification and crop health mapping; and 2) to compare and contrast the resolution of water stress zone identification for precision irrigation technology implementation. Thermal infrared (TIR) and multispectral images were obtained over a four-acre cornfield using a quadcopter (Matrice-100), aircraft (Ceres Imaging), and Satellite (Landsat-8). Spatial maps of canopy temperature and NDVI were developed using these images and analyzed for capacity to capture water requirements and crop health accurately. UAV imagery outperformed the other two platforms in providing detailed imagery and sensing changes in crop health throughout the field. For a sample area of dimension 82 m x 44 m, the UAV imagery provided 683 different types of canopy temperature values. In

contrast, aircraft imagery provided 158 different values, followed by satellite imagery which provided only 5-6 variations in canopy temperature to represent the same area. Moderate and low spatial resolution imagery from aircraft (1-1.5 m/pixel) and satellite (30 m/pixel) was limited in detecting inter-row variability and outputting the average pixels of the crop canopy and inter-row space. Whereas high-resolution UAV imagery (1.5 cm/pixel – 6 cm/pixel) precisely distinguished inter-row gap from plants and provided crop-only pixels without mixing with background soil. UAV imagery was precise and sensitive in detecting crop variability between two nozzles of an irrigation pivot, while aircraft imagery was less precise and sensitive. Satellite imagery was not able to capture the variations at this small scale. So, overall, UAV and aircraft imagery remains competitive in providing infield crop health variability for site-specific management in agriculture. Satellite imagery is limited in providing infield crop health variability to design site-specific irrigation, especially for small-scale farms.

4.2 Introduction

Precision agriculture offers solutions to control agricultural production while ensuring quantity and quality through the use of site-specific management. Site-specific management involves dividing an agriculture field into different zones to receive optimized inputs based on the infield crop health variability rather than a uniform application of inputs [Jones *et al*., 2017]. Precision agriculture becomes an essential tool in site-specific management through monitoring yield, plant stresses, nutrient status, and water requirements for sustainable farming practices [Segarra *et al.*, 2020]. To quantify in-field variability, numerous tools and techniques have been used in the past. Traditional methods of ground-based surveying and sample collection with added lab analysis to quantify crop traits are laborious and not quick, so they are not suitable for a field scale and continuous monitoring of plant traits [Bosecker 1988; Comba *et al*., 2020; Ziliani *et al.*, 2018].

Remote sensing, a non-destructive, low labor intensive, considers spatial variability, emerged as a robust tool to monitor crop traits at the field scale [Berger *et al*., 2020; Campos-Taberner *et al*., 2018; G. Poley & J. McDermid, 2020; Li *et al.*, 2022; Ten Harkel *et al*., 2019]. Remote sensing in agriculture is majorly influenced by platform altitude, spatial resolution, and the frequency and time-precision of revisiting an area (temporal resolution) [Metternicht *et al.*, 2008; Messina *et al*., 2020]. Spatial resolution dictates the smallest object/area to be detected in imagery; thus, the key indicator of the level of detail in images. As spatial resolution drops, plant and background soil homogeneity in a single pixel increases, leading to less precise measurements of crop traits [Mulla, 2013]. There are three main remote sensing platforms: unmanned aerial vehicles (UAVs), aircraft, and satellites, which cover most of the spatial resolutions and altitudes used in agriculture.

Each remote sensing platform has its benefits and limitation from a technical and operational point of view. Satellite imagery is susceptible to degradation by atmospheric factors like light absorption, scatter by clouds, aerosols, gasses, and temperatures that reduce the availability and consistency of satellite imagery. Another downside of satellite imagery is that it can only be acquired on a fixed day and time, which depends on the revisit times of the satellite. It's not possible to acquire satellite images at a desired crop phenological stage or time window [Barzin *et al*., 2020; Gevaert *et al.*, 2015]. Satellite imagery's benefits include large area mapping in a single drive, easy to access and free of cost (several but not all) available data, heavy payload capacity, and no constraint on flight duration [Li *et al*., 2022]. However, UAV imagery provides elasticity in operations; users can perform multitemporal and custom-defined campaigns. Low-altitude UAV flights are easy and safer to conduct, provide a very high spatial resolution of centimeters level and avoid the majority of atmospheric interferences and clouds [Han *et al*., 2021; White *et al*., 2012; Zarco-Tejada *et al*., 2013]. UAVs have widespread implementation and are suitable for small farms but have weaknesses like limited payload capacity, short flight duration, technical complexity, and little spatial coverage. Aircraft imagery fills the gaps between satellite and UAV imagery by providing an optimum spatial coverage with a decent spatial resolution of around 1-5 meters for farm scale variability detection. Aircraft surveys can be executed efficiently compared to the other platforms but involve higher costs and complex campaign organization efforts and are prone to skip fine-scale details [Matese *et al*., 2015].

Quantification of water requirements has been a significant application of remote sensing in precision agriculture. Remote sensing has been extensively used in monitoring plant water status using satellites [Hussain *et al*., 2020; Krishna *et al*., 2021; Ndlovu *et al*., 2021; Sibanda *et al*., 2021; Xu *et al*., 2020] and UAVs [Jaganmohan *et al*., 2016; Kang *et al*., 2018; Yang *et al*., 2017].

For estimating plant water requirements, surface or canopy temperature (in the case of agricultural crops) is the most accepted and reliable tool [Awais *et al*., 2022; Peñuelas *et al*., 1993]. Thermal infrared (TIR) imaging can quantify canopy temperatures using different remote sensing platforms. TIR imaging is significantly affected by the altitudes and atmosphere between the imaging sensor and the target objects. Because of these effects and low spatial resolution, satellite imagery provides very few and similar temperature measurements throughout the field. UAV-based TIR imaging can precisely distinguish the surface temperature features due to its high spatial resolution and very low altitude (20 to 100 m) flight closer to the crop, diminishing the weather effect [Webster *et al.*, 2018].

So, selecting an appropriate remote sensing platform is always a trade-off based on user requirements. A comparative assessment is necessary to highlight each imaging system's capacity and benefits for a specific objective. A few studies have compared the performance of UAV and satellite-based thermal imaging [Deilami et al., 2018; Kraaijenbrink et al., 2018]. But a comparative analysis of different remote sensing platforms for canopy temperature sensing from an irrigation point of view still needs exploration. Therefore, this study aims to examine the capacity of UAV, aircraft, and satellite-based thermal and multispectral imaging in detecting crop health variability in corn at a very fine scale for irrigation management.

4.3 Materials & Methods

4.3.1 Experimental Site

This study was conducted during the years 2020 and 2021 on a four-acre corn field at the Kansas Research Valley experiment field (39.076076° N, -95.768777° W), Silver Lake, Kansas, USA, with Eudora Silt Loam soil type. Fields used for both years were adjacent, as shown in

Figure 4.1. Corn was planted on 22 April 2020 and 15 April 2021 with a row direction from west to east and a row spacing of 76 cm (30 inches). The aerial imagery was collected using three

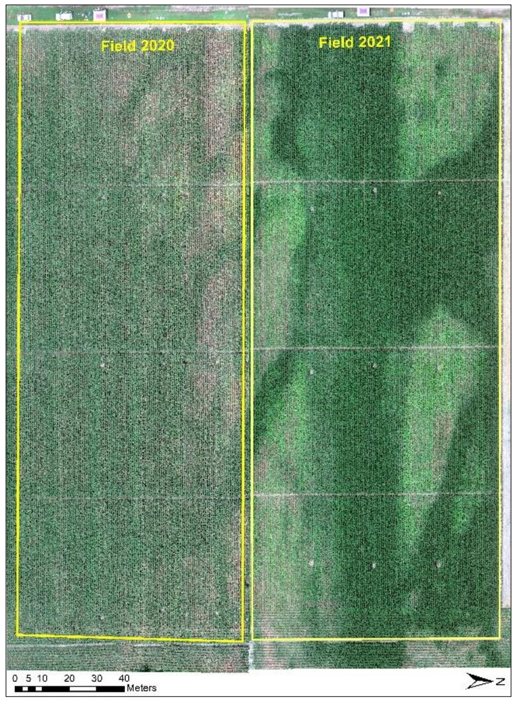

Figure 4.1 RGB orthomosaics of the experiment fields for years 2020 and 2021

different remote sensing platforms at full canopy coverage during the late vegetative stage of corn.

4.3.2 Crop parameters

Two crop parameters: Leaf surface temperature and NDVI were considered for the comparative assessment of remote sensing platforms. Canopy temperature has a relatively quick response, and temperature changes can be seen prior to changes in plant structure or pigmentation. In precision agriculture, site-specific plant stress (heat stress or water stress) monitoring is the primary application of canopy temperature. The stomatal apertures of leaves, the opening and closing of which regulate the transpiration rate, act as a cooling mechanism to regulate the leaves' temperature. When plants are exposed to adverse conditions, the leaf temperature rises, and in response to that, plants cool down by increasing the transpiration rate through stomata openings.

It is feasible if the water supply to plants is adequate; otherwise, plants will not be able to increase transpiration, leading to an increase in canopy temperature. This property made canopy temperature the most reliable tool to detect plant stresses before any visible symptoms appear [Jones *et al*., 2014; Zhang *et al.*, 2019; Giménez-Gallego *et al.*, 2021]. To quantify canopy structure changes, the NDVI (Normalized Difference Vegetation Index) was derived to measure the crop canopy greenness and vigor.

$$NDVI = \frac{(\text{NIR} - \text{RED})}{(\text{NIR} + \text{RED})} \tag{1}$$

Where RED and NIR represent reflectance in the red and near-infrared bands. The NDVI values range from -1 to +1; a crop with a sparse canopy or meager vegetation cover is described by moderate NDVI values ranging from 0.2 to 0.5. The presence of dense and healthy vegetation, such as crops at peak growth, is characterized by NDVI values higher than 0.6 [Gidey *et al.*, 2018]. So, canopy temperature and chlorophyll/greenness changes are key indicators of crop health. To evaluate aerial imagery from various platforms for crop monitoring and site-specific management, these parameters should be considered for the appropriate results.

4.3.3 Aerial Imagery

Three remote sensing platforms: unmanned aerial vehicle (UAV), manned aircraft, and

Table 4.1 Aerial imagery collection details for UAV, aircraft, and Satellite

Imaging Platform	Flying Altitude	Spatial Resolution (Per pixel)		Datasets			
		Thermal Infrared	Multispectral	D1	D2	D3	D4
UAV	50 m	6 cm	1.5 cm	07/19/2020	08/18/2020	08/06/2021	08/17/2021
Aircraft	3400-3500 m	1.2 m	0.9 m	07/25/2020	08/11/2020	08/07/2021	08/22/2021
Satellite	-	100 m	30 m	07/25/2020	08/18/2020	08/21/2021	08/21/2021

satellite, were used to map corn fields for crop canopy temperature and NDVI. Collecting the imagery from all platforms on the same day were not feasible, so the closest possible images from all three formats were obtained. Imagery collection altitude, spatial resolution, and data collection date for each remote sensing platform are mentioned in Table 4.1.

4.3.3.1 UAV

A quadcopter, Matrice 100 (Shenzhen DJI Sciences and Technologies Ltd.), was used to collect thermal infrared (TIR) and multispectral aerial imagery (Figure 4.2). It has a payload capacity of 1 kg with a maximum flight time of 40 minutes. FLIR Vue pro-Thermal Infrared sensor (FLIR Systems, USA), with a focal length of 13 mm and resolution of 640 x 512 pixels, was used for thermal infrared (TIR: 7.5 – 13.5 μm) imaging. Multispectral images were collected using a MicaSense Red-edge camera (MicaSense, Inc., WA, USA), which records spectral response in 5 different bands – blue (475 nm), green (560 nm), red (668 nm), red-edge (717 nm), and near-infrared (842 nm). For both imaging sensors, UAV was flown at 50 m altitude with a speed of 3 m/s [Sangha *et al.*,2021; Gadhwal *et al.*, *2022*]. Throughout the study period (2020-2021), multiple flights were conducted, but only two flights each year representing the clear sky days and good-quality images were considered for analysis.

UAV was flown on autopilot mode guided by a fixed route of waypoints, commonly known as a flight mission, generated using the Mission planner. Forward and side overlaps between images were kept at 85% to meet image stitching requirements and smoothly develop orthomosaics. As recommended by the mission planner, both cameras were triggered after 1 second depending on flying altitude and image overlap. Since UAV was not directly compatible with the mission planner, a web-based platform (Litchi, VC Technology Ltd) was used to transfer missions from the mission planner to UAV. Thermal images were geotagged using an autopilot controller (PixHawk, 3DR) and an independent GPS unit; multispectral images were geotagged using the integrated module within the camera. Flights were conducted around solar noon since shadows on the side of plants before and after solar noon can cause errors in imagery. Captured images were assembled into orthomosaics following standard workflow from Metashape Professional by Agisoft (Agisoft LLC, St. Petersburg, Russia). Real-Time Kinematic (RTK) corrected coordinates of 16 ground control points (GCPs), distributed evenly throughout the field, were measured using Topcon GR-5 (Topcon, Tokyo, Japan) GNSS receivers with centimeter-level positioning accuracy. These coordinates were then used in Agisoft to provide images and orthomosaics with very high positioning accuracy. Before generating orthomosaics, multispectral images were calibrated to account for lighting conditions during the acquisition period. For this

Figure 4.2 UAV imaging system used in the study

calibration, images taken before and after the UAV flight of a calibration panel (provided by the camera manufacturer) were used in Agisoft. For each flight date, the final products used from Agisoft were thermal and multispectral ortho mosaics with cm-level positioning accuracy. Using the method described in our previous study [Gadhwal *et al.*, 2022], the thermal orthomosaics were converted into the canopy temperature map. NDVI maps were generated using required bands from multispectral orthomosaic in the Raster calculator tool of ArcMap 10.6.1 (ArcGIS, ESRI, Redlands, CA, USA).

4.3.3.2 Aircraft

Aerial imagery was obtained from a commercial platform, CERES Imaging (CERES Imaging, CA, USA), on the closest possible dates to UAV flights. A manned aircraft flying at 1,000-1,500 m altitude captured thermal images with a 1.5 m/pixel spatial resolution and multispectral images with a spatial resolution of 1 m/pixel. The imaging platform (CERES Imaging) performed all image processing and provided two types of orthomosaics: thermal and multispectral. The thermal orthomosaic contained surface temperature values in degree Celsius and was directly used for further analysis. The multispectral orthomosaic had reflectance values corresponding to 4 bands (B1: 800 nm, B2: 670 nm, B3: 550 nm, and B4: 717 nm). Red (B2) and near-infrared (B1) bands were used to calculate the (NDVI) vegetation index using the Raster calculator tool of ArcMap.

4.3.3.3 Satellite

Landsat surface reflectance and surface temperature images were downloaded from USGS Earth Explorer (https://earthexplorer.usgs.gov) as close as possible to both UAV and aircraft imagery. The images were obtained from "Landsat Collection 2 U.S. Analysis Ready Data (ARD)", which became publicly available via Earth Explorer in Fall 2021. Landsat ARD data sets are processed to the highest scientific standards and can be used directly. The use of this data evades remote sensing preprocessing steps such as radiometric correction, geometric correction, and cloud detection and allows more time for analysis and applications [Dwyer *et al.*, 2018; U.S. Geological Survey, 2018; Zhu, 2019 and Ren *et al.*, 2021]. The original spatial resolution of Landsat8 surface reflectance images was 30 m/pixel, and of surface temperature images was 100 m/pixel, but ARD thermal images were resampled to provide a spatial resolution of 30 m/pixel. The ARD surface temperature data was originally derived from the thermal infrared band (Band 10 TIRS1: 10,600-

11,190 nm) of the Landsat8 satellite.

To convert surface temperature images to temperature maps (pixel values in kelvin), a multiplicative scale factor of 0.00341802 and an additional offset of 149.0 was required. The temperature maps in kelvin were then converted to degree Celsius maps. Similarly, the surface reflectance images needed to be multiplied by 0.0000275 and offset by -0.2 before further use. After scaling, NDVI maps were generated using Red (Band 4: 640 - 670 nm) and Near-Infrared (Band 5: 850 - 880 nm) bands from ARD reflectance data. All the raster calculations and map generation were accomplished using ArcGIS. The temperature and NDVI maps were clipped to the field's boundary and used as final products from the satellite platform.

4.3.4 Data analysis

The crop canopy temperature is a very sensitive plant characteristic that varies drastically with the changes in air temperature, humidity, wind speed, and cloud cover. So, temperature measurements from different dates should not be directly compared for values, as the weather conditions of two other days substantially differ. It can be noticed from Table 4.1 that the imagery representing each platform was from different dates. Comparison of canopy temperature's spread, distribution, and spatial patterns over the same field at different dates is still viable. Whereas NDVI depends on chlorophyll content and is an internal property of the plant leaves, it doesn't change rapidly and can be compared directly for the imagery from a few days apart.

The spatial variability throughout the field was assessed using NDVI and canopy temperature maps obtained from various imaging platforms. Datasets from two different dates were analyzed for each year. The capability of a particular imaging platform to detect in-field variability was initially evaluated through a visual examination of the spatial maps. Initially, the maps were classified using equal intervals and a consistent symbology for all platforms. However, this uniform symbology approach led to a loss of granular information due to significant variations in details and distributions of NDVI and temperature values between platforms. For the dataset

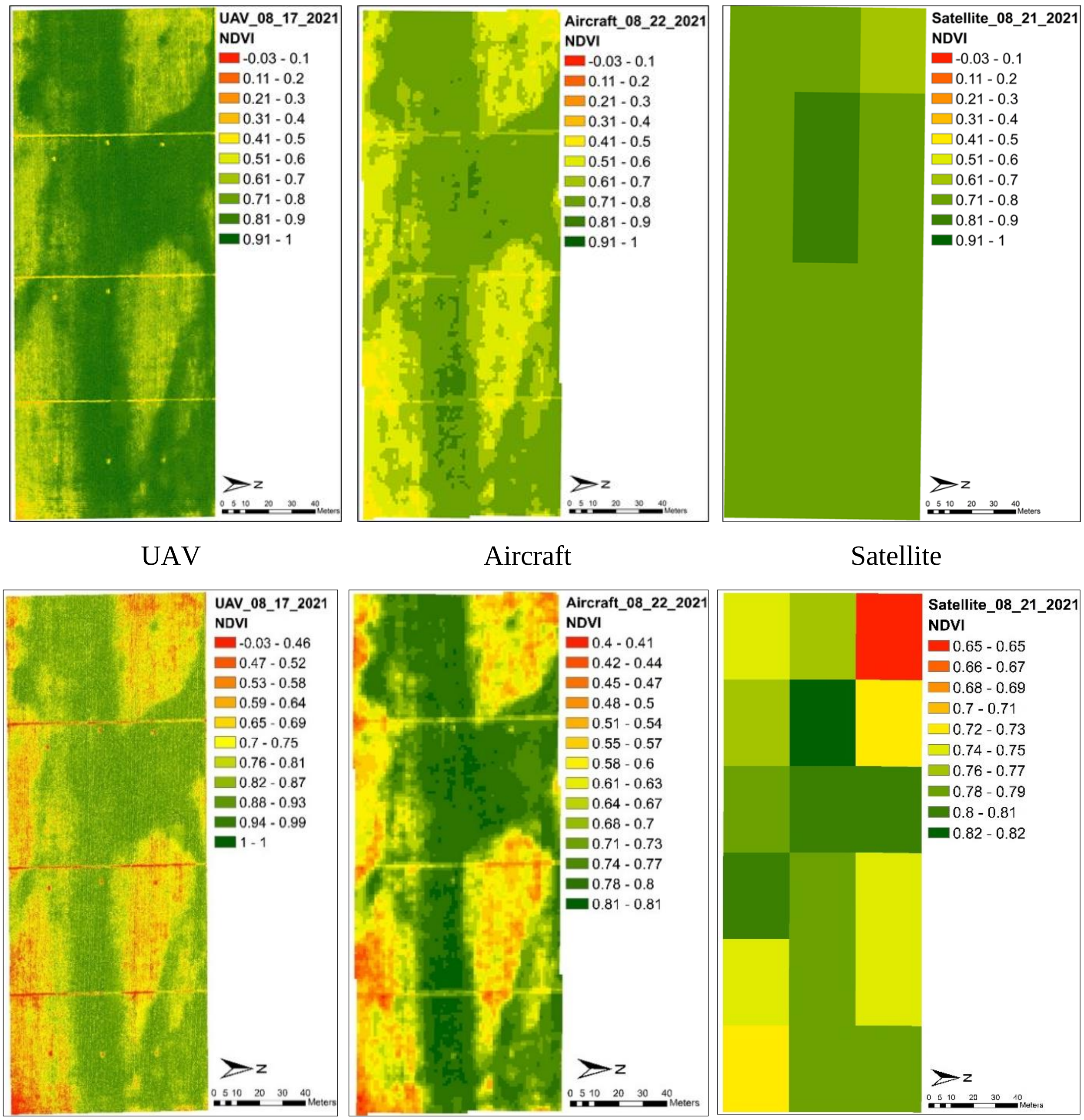

Figure 4.3 Spatial NDVI maps' classification: equal interval and same symbology (top), and standard deviation-based classification (bottom)

presented in Figure 4.3, the NDVI values for UAVs ranged from -0.03 to 1.0; for aircraft, they ranged from 0.4 to 0.81; and for satellites, they ranged between 0.65 and 0.82. As a result, applying the same symbology and intervals to express this differently spread data from the three platforms became challenging. Similar behavior was observed for temperature maps as well.

After exploring various classification methods, the standard deviation classification method was used to present fine details and enhance the contrast between different values within the field. This approach creates classes with equal value ranges that are a proportion of the standard deviation, typically at intervals of one, one-half, one-third, or one-fourth, using mean values and standard deviations from the mean. This method significantly improves contrast by dividing the color palette only between variations from the mean value. The standard deviation approach outcomes can be observed in Figure 4.3, where background soil, irrigation pivot track marks, and different crop health zones are clearly visible, whereas, in the equal interval approach, they appeared slightly mixed. Therefore, the standard deviation method was chosen for visual comparison and analysis. The pixel values from spatial maps and the number of pixels representing these values were also plotted to determine the level of detail provided by each imaging platform. These plots were also exploited to analyze the distribution and behavior of NDVI and canopy temperature across the field, enhancing the visual inspection.

The focus of this study was to gauge the capacity of different remote sensing platforms to provide inputs for precise site-specific irrigation management. In the agricultural irrigation application, pivot nozzles are the smallest and base unit. To develop an efficient and applied variable irrigation system, it’s essential to assess crop variability at the nozzle’s scale. A small field segment covered by a sub-section of the irrigation pivot was selected to measure this variability. Imagery with the minimum difference in collection days from different platforms and showing sufficient in-field variability (dataset D4) was used for this analysis. Several lines representing the movement of the irrigation pivot’s nozzles were laid over spatial maps to visualize the crop parameter variations between nozzles. The number of pixels used to cover the target area, variety in values, mean value, and standard deviation were estimated for canopy temperature and NDVI from each imaging platform. Further, to analyze the performance of imaging platforms in detecting fine-scale changes in crop health, the region between two adjacent nozzles with a mix of healthy and underperforming plants was comprehensively explored using profile graphs.

4.4 Results & Discussion

4.4.1 Entire field spatial visualization

4.4.1.1 Season 2021

To assess the spatial variability in the corn field, canopy temperature, and NDVI maps generated from the three imaging platforms: UAV, aircraft, and satellite were explored. For season 2021, two datasets, D3 and D4, were considered; dataset D3 represented a crop with a comparatively denser and greener canopy compared to dataset D4. It can be seen from the NDVI maps (Figure 4.5) that the middle portion of the field and certain regions on the northern boundary exhibited high (>0.75) NDVI values (dark green color), indicating the presence of healthier crops. These regions showed a wider spread of healthy plants in dataset D3 compared to a thinner spread in dataset D4. A similar pattern was observed from the temperature maps (Figure 4.4), where the healthy crop was represented by lower temperature values (blue color), and stressed zones exhibited higher temperature values (yellow and red color).

It was noticed that UAV and aircraft imagery were able to differentiate the healthy and stressed regions with a high degree of accuracy. In contrast, satellite imagery could not achieve the same level of discrimination due to its low resolution. Furthermore, the UAV imagery was able to capture small-scale variations like very slight shrinkage in the portion of the healthy crop, whereas the aircraft imagery was able to capture relatively large-scale variations, especially in thermal imagery. Values corresponding to entire spatial maps were also plotted to show the distribution of

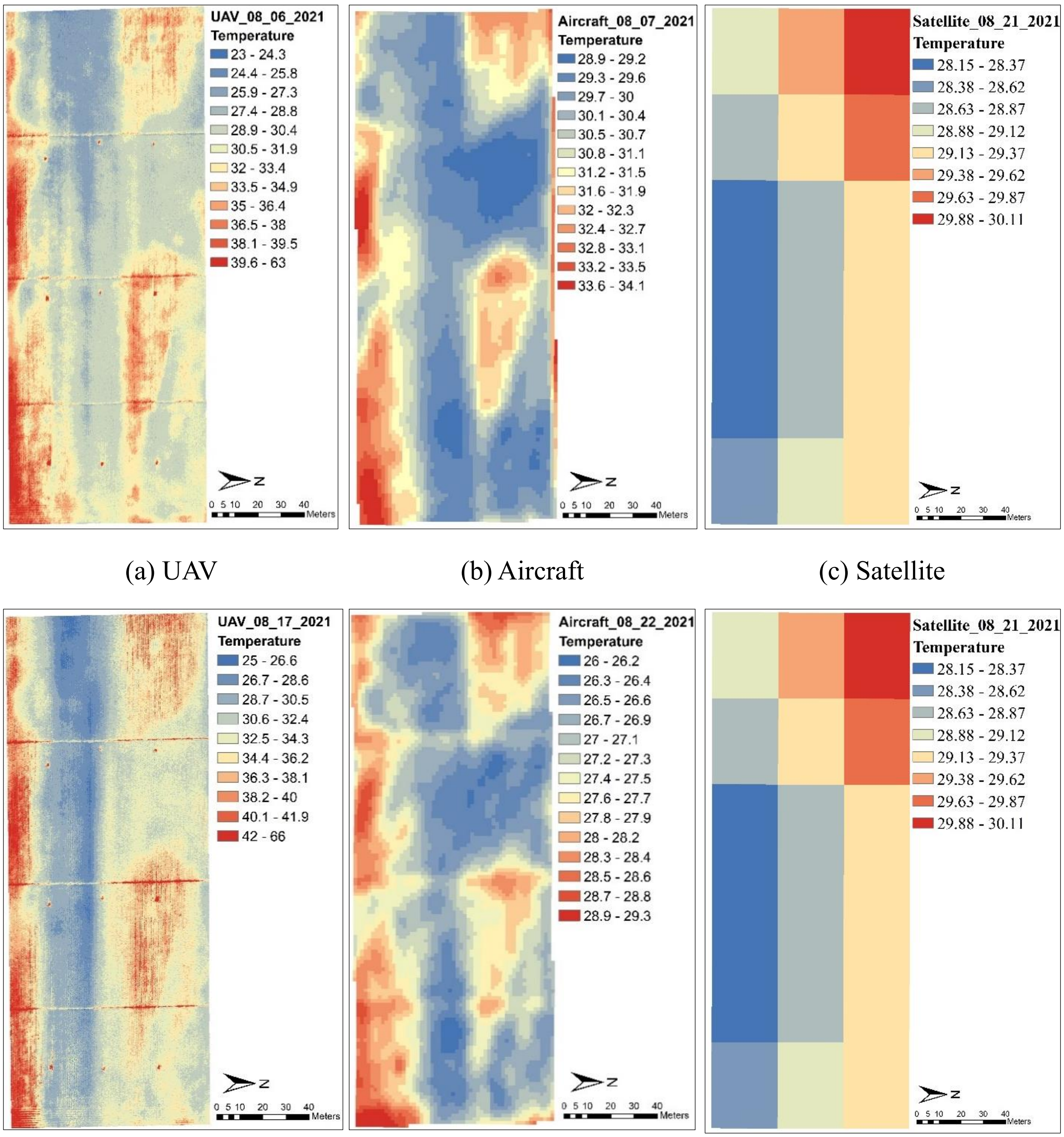

Figure 4.4 Spatial maps of corn canopy temperature of the entire field for dataset D3 (top) and D4 (bottom)

NDVI and temperature throughout the field. The temperature plots (Figure 4.6) showed that the UAV maps covered a wide range of temperatures, spread over a span of 12 °C representing all kinds of temperature values from the field. This indicates that the UAV imagery captured a broader range of temperatures, including extreme temperature values generated from bare soil or objects

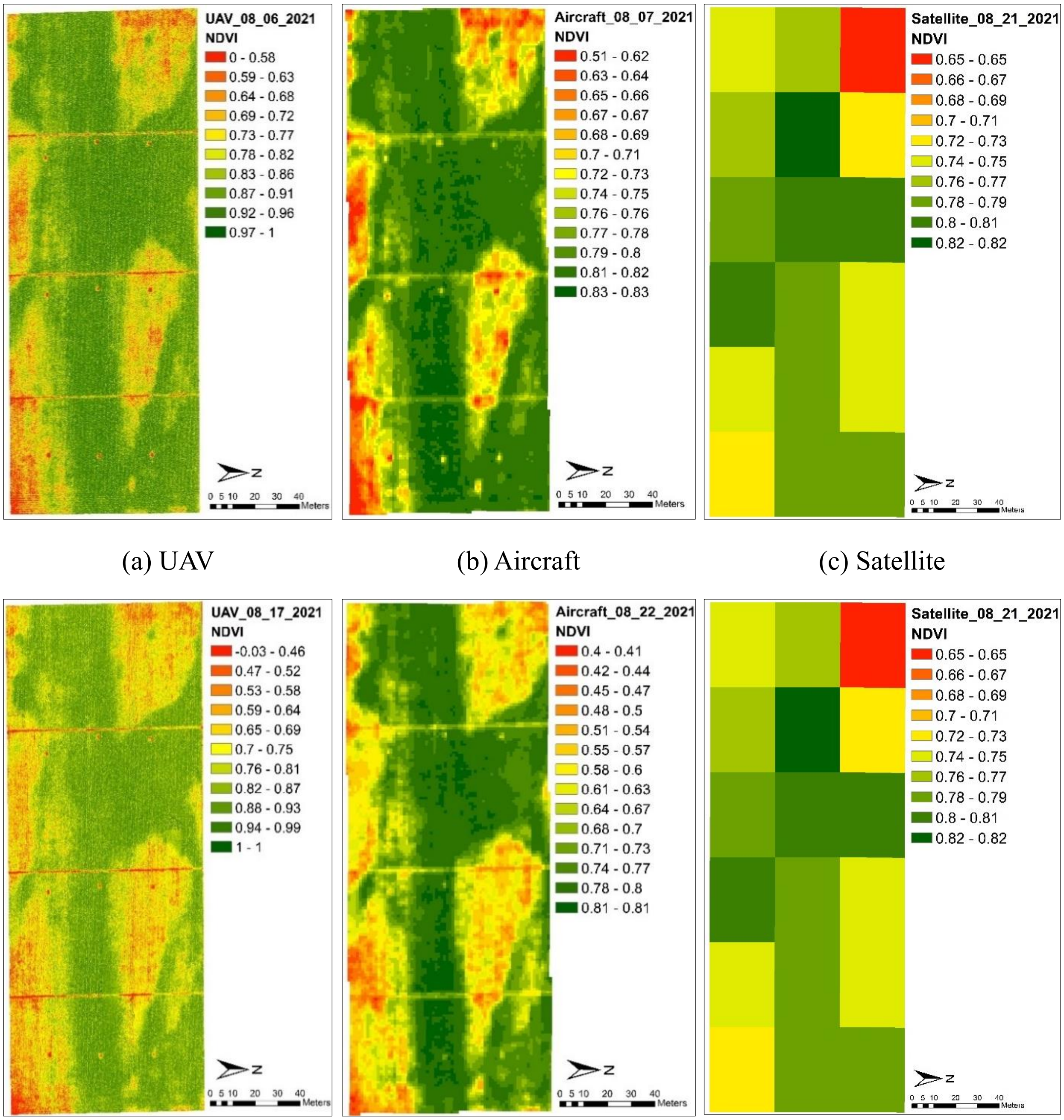

Figure 4.5 Spatial maps of NDVI of the entire corn field for dataset D3 (top) and D4 (bottom)

different from plants, as well as minor temperature variations within the crop. In contrast, the aircraft images had a narrower spread of 4 °C to 5 °C, indicating that the aircraft imagery was not able to capture as many temperature variations as the UAV imagery. The satellite images had an even narrower range of 2 °C, indicating that the satellite imagery could only catch very few temperature variations compared to the other two platforms. The NDVI plots (Figure 4.7) also

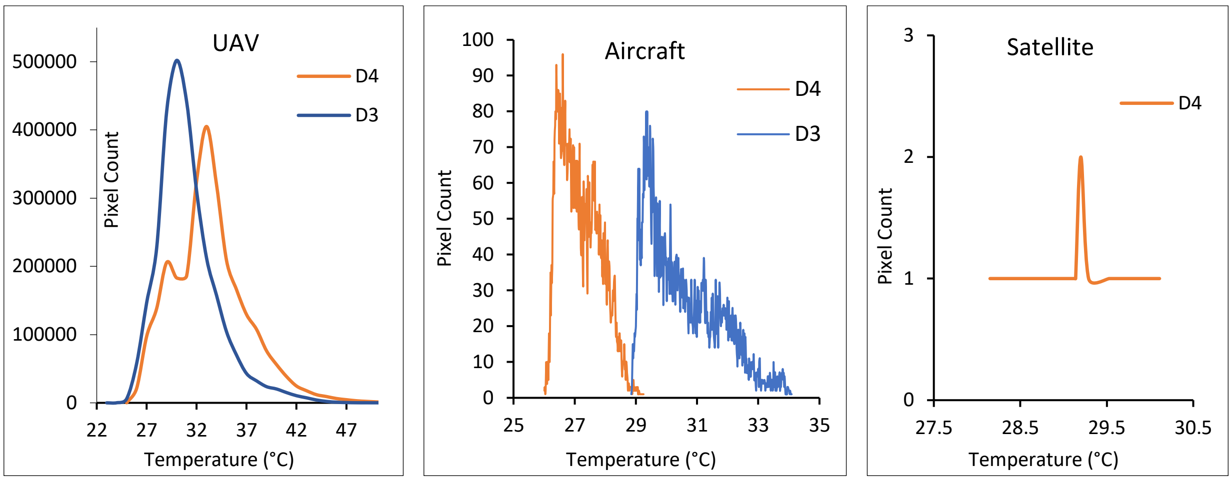

Figure 4.6 Temperature plots from spatial maps of season 2021: a) UAV b) aircraft and c) Satellite

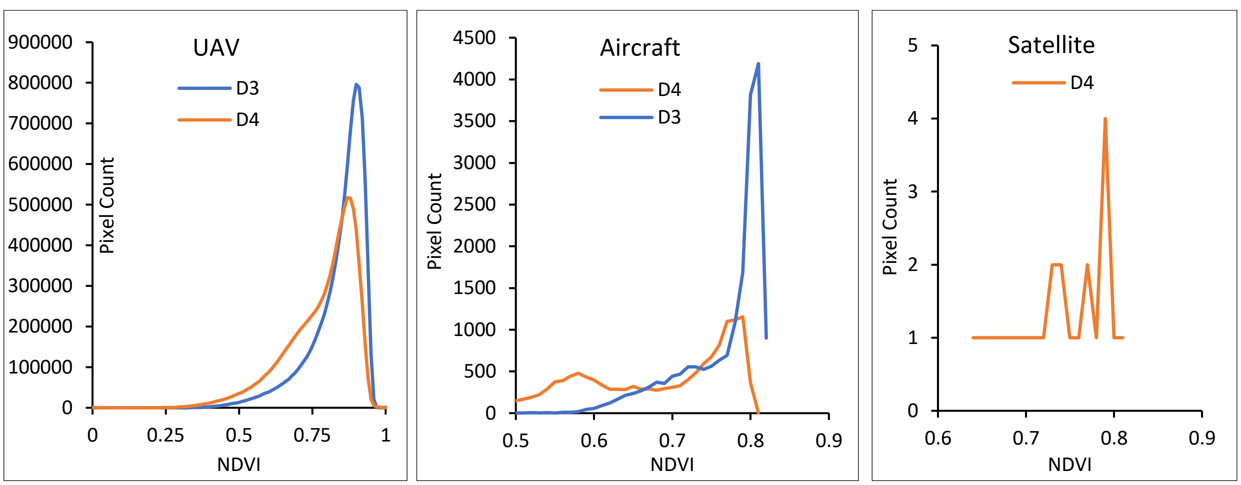

Figure 4.7 NDVI plots from spatial maps of season 2021: a) UAV b) aircraft and c) Satellite

showed a clear difference between the range captured by different imaging platforms. Additionally, the NDVI plots showed that dataset D4, with a slightly less healthy crop, exhibited substantial values between 0.5 and 0.75 for UAV and aircraft imagery, indicating the presence of less healthy plants. On the other hand, the majority of NDVI values for dataset D3 were found to be more than 0.7, corresponding to healthy plants.

4.4.1.2 Season 2020

Two datasets from season 2020, D1 and D2, were also included for spatial visualization of infield variability. The 08/18/2020 satellite thermal imagery was of inadequate quality and was

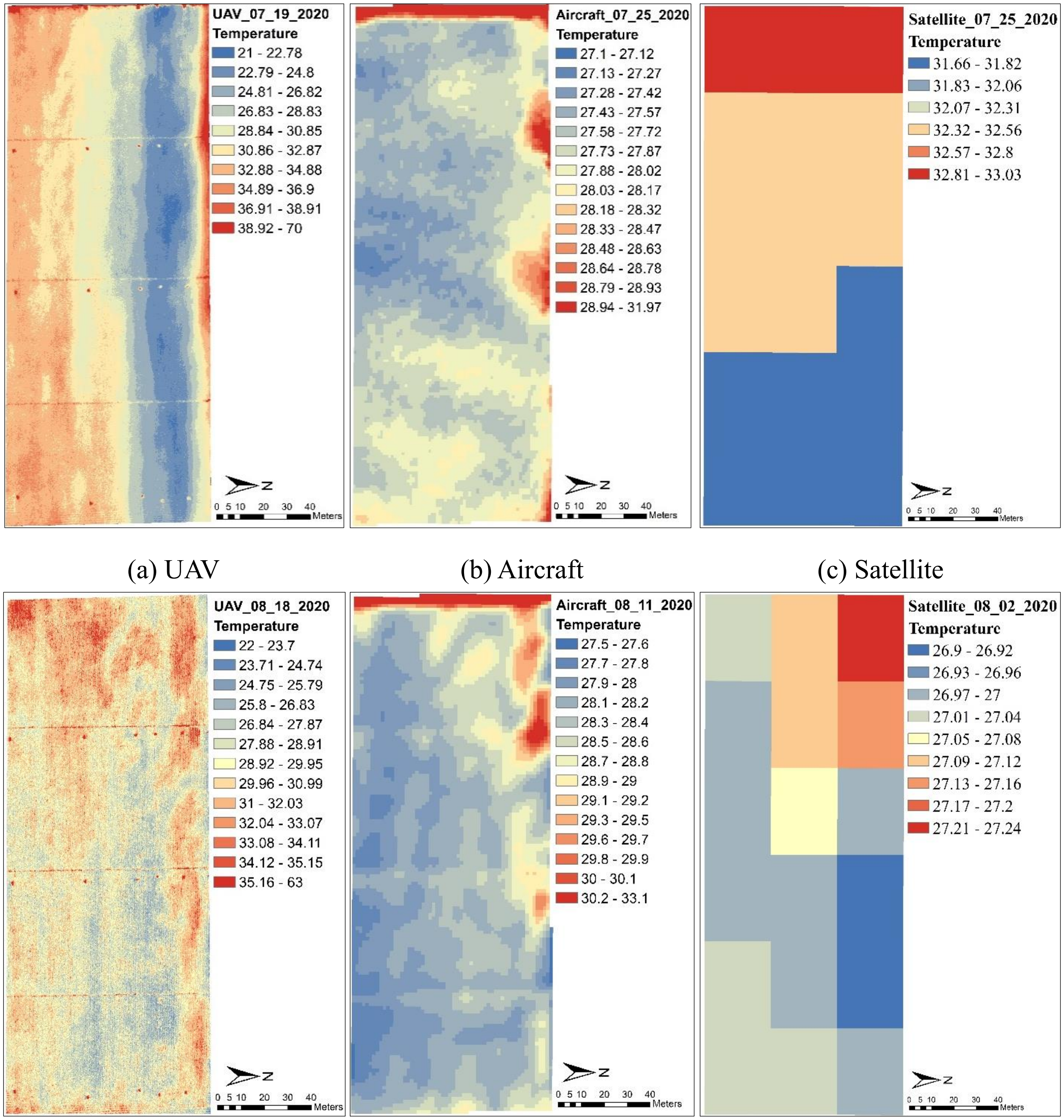

Figure 4.8 Spatial maps of corn canopy temperature of the entire field for dataset D1 (top) and D2 (bottom)

substituted with the next closest available thermal imagery from 08/02/2020. There was minor within-field variability and a slight difference between crop health among these two datasets but

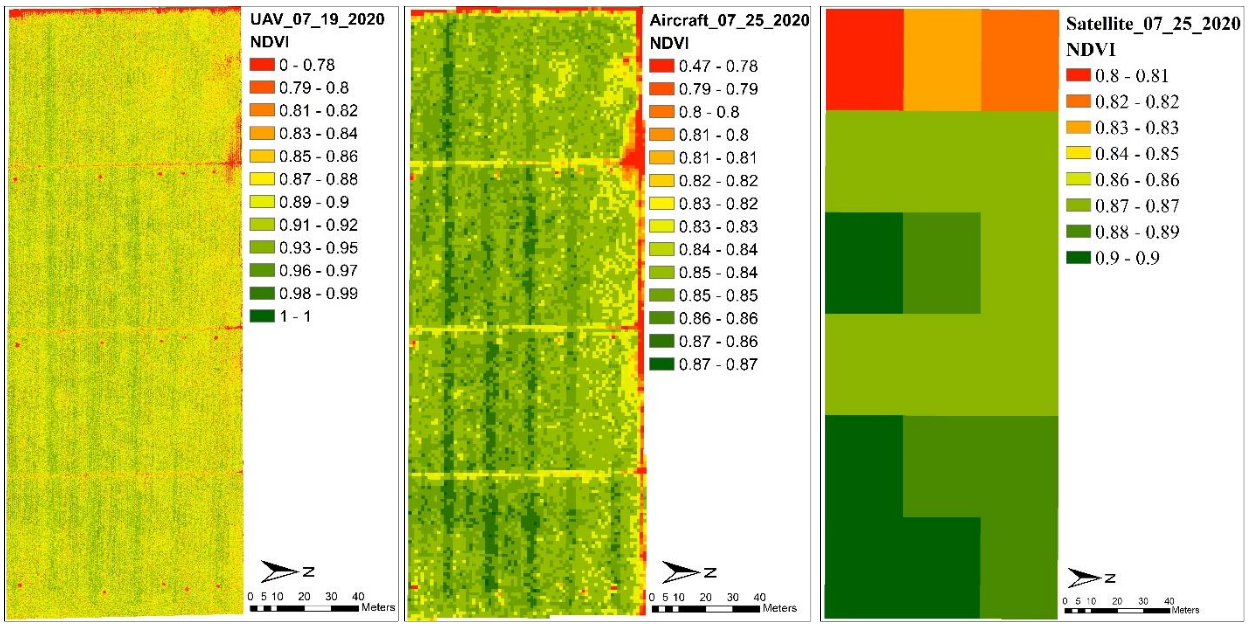

(a) UAV (b) Aircraft (c) Satellite

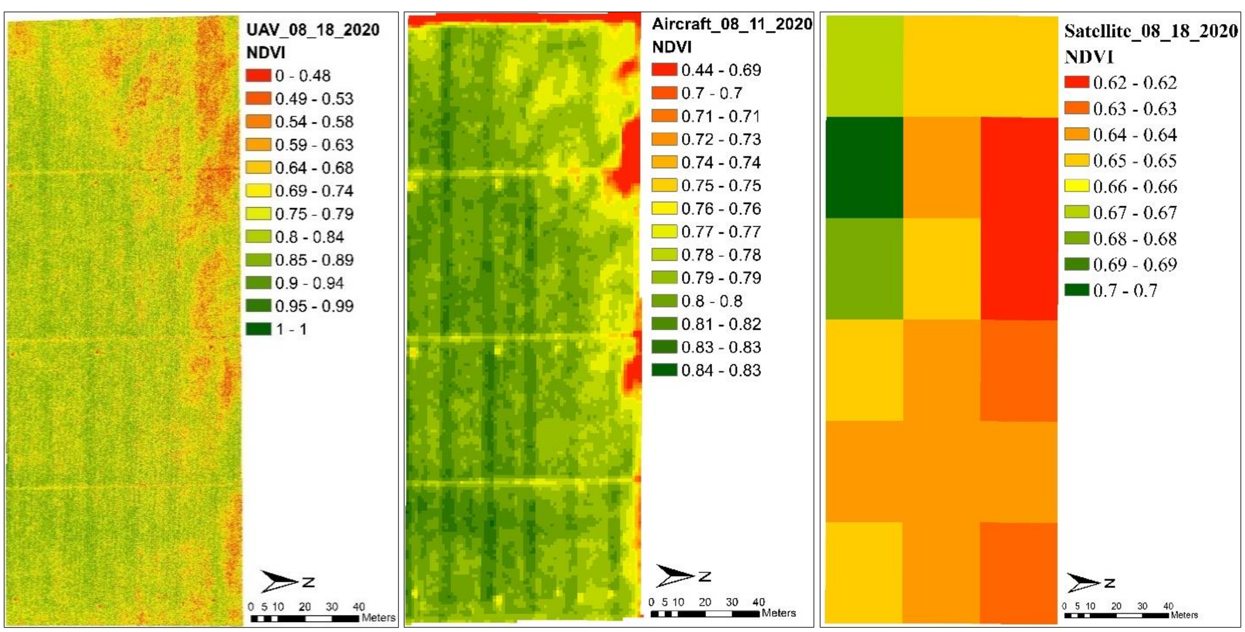

Figure 4.9 Spatial NDVI maps of the entire corn field for dataset D1 (top) and D2 (bottom)

not as strong as in the two datasets from season 2021. Considering the NDVI and temperature spatial maps (Figures 4.8 and 4.9), bright red regions common in datasets D1 and D2 on field boundary were the regions with bare soil where no crop was planted. From NDVI maps (Figure 4.9) of dataset D1, it can be clearly seen that the crop was uniformly healthy throughout the entire field. However, slight stress was noticed nearby the northwest boundary from temperature and NDVI maps of the D2 dataset. These changes were clearly visible in UAV and aircraft maps, but satellite imagery was not able to detect these changes because of the low resolution. The presence

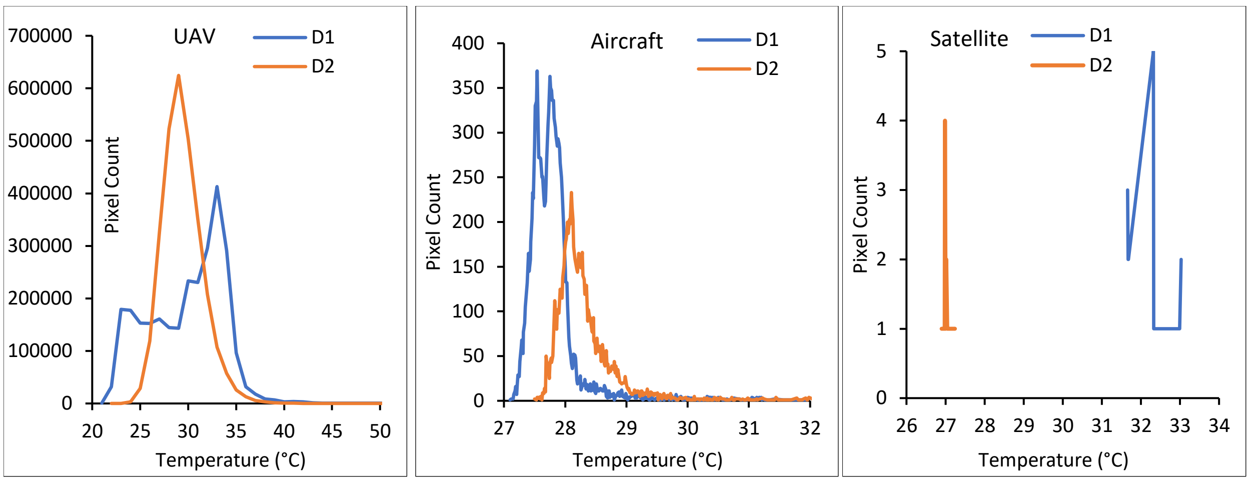

Figure 4.10 Temperature plots from spatial maps of season 2020: a) UAV b) aircraft and c) Satellite

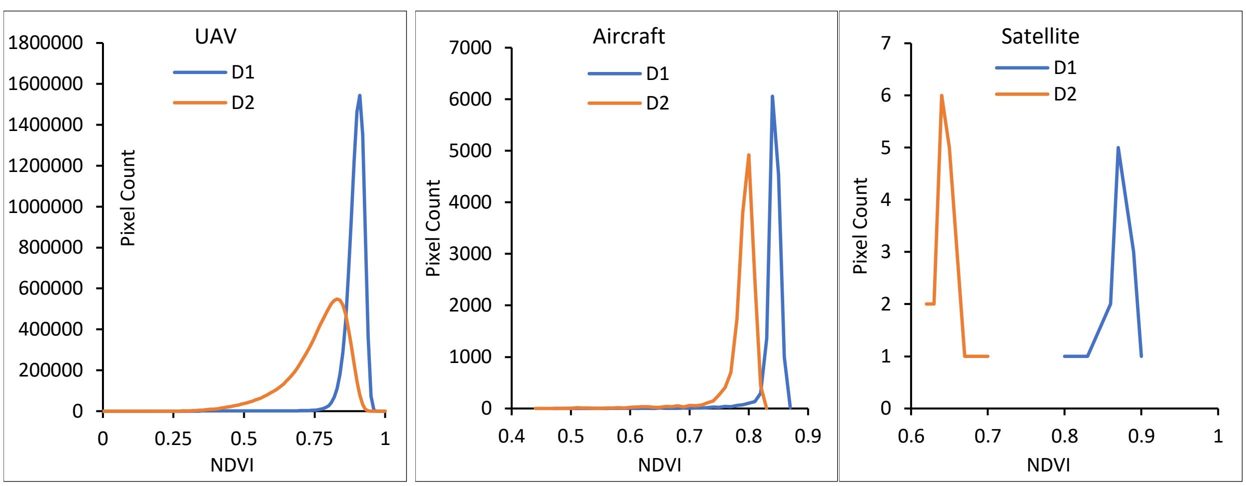

Figure 4.11 NDVI plots from spatial maps of season 2020: a) UAV b) aircraft and c) Satellite

of healthy plants throughout the field for the D1 dataset can also be noticed from NDVI distribution plots (Figure 4.11), where most NDVI values were greater than 0.8 for all three imaging platforms.

However, the D2 dataset exhibited a shift of the NDVI distribution curve towards lower values, which can be attributed to the presence of the stressed plants. The UAV imagery showed significant values between 0.4 to 0.75, demonstrating its ability to detect slight variations in crop health. On the other hand, the aircraft and satellite imagery exhibit NDVI values above 0.7, indicating limitations in their ability to detect small changes but still able to detect major changes in crop health. The temperature curves generated from the UAV-based imagery had a broad range of values spread across a wide span of 15 to 20 °C. This range includes high and low values attributed to bare soil or objects other than plants in the field. In contrast, the temperature curves generated from the aircraft-based imagery had values spread over 3 °C. The satellite-based imagery had an even narrower range of values, spread across a span of only 1 °C to 2 °C, indicating that the satellite-based imagery has its limitation in detecting variations in temperature within the crop. This comprehensive analysis demonstrates the capacity of different remote sensing platforms to assess the spatial variability in crop fields and identify specific areas that require additional attention. The higher spatial resolution and greater sensitivity of the UAV-based imagery outperformed the rest two platforms. Aircraft-based imagery was still able to detect significant changes, but satellite imagery was not suitable for assessing the spatial variability in small crop fields (like the one used in this study) for precision agriculture and irrigation management.

4.4.2 Fine-scale crop variability assessment

The capacity of three imaging platforms in crop variability assessment at a very fine scale was examined using an 82 meters wide (full width of the field) and 44 meters long section of the field covering a sub-section of an irrigation pivot. Imagery corresponding to dataset D4, was extracted over the boundary of this region (Figure 4.12). Visible marks generated from the irrigation pivot tracks moving in a North-South direction can be seen in UAV imagery. Fourteen

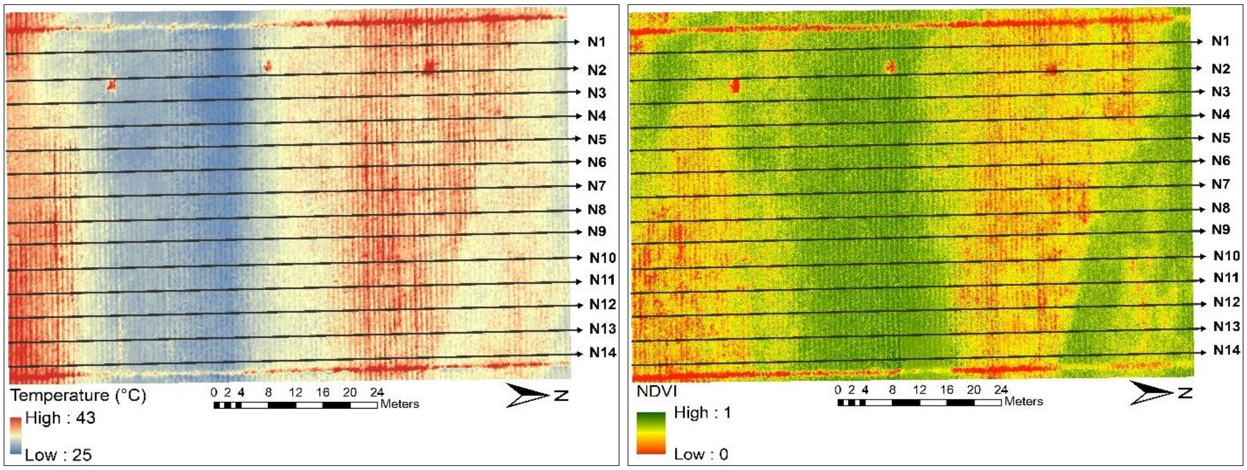

(a) UAV

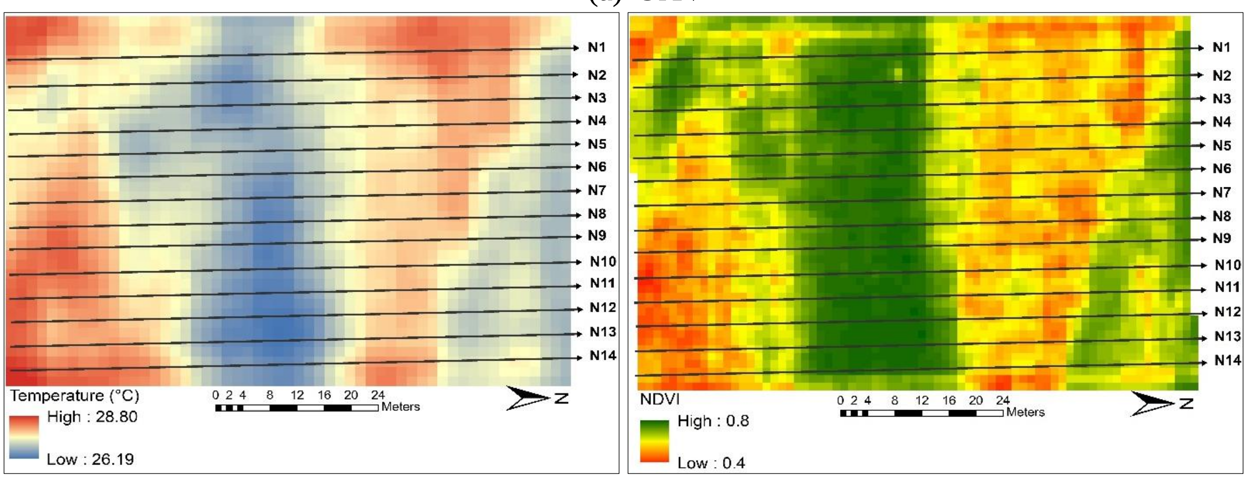

(b) Aircraft

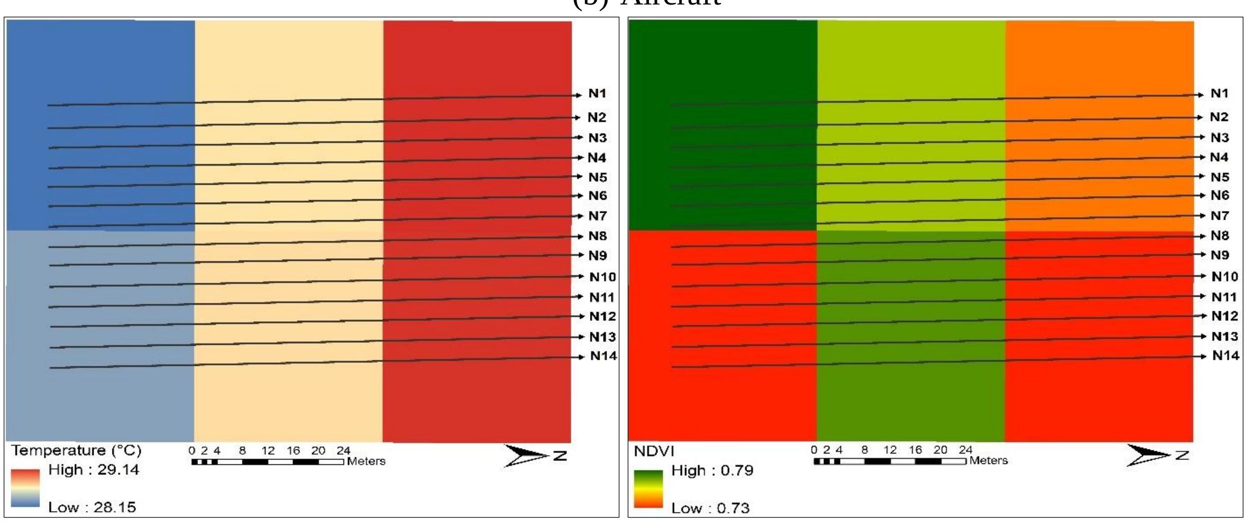

(c) Satellite

Figure 4.12 The temperature and NDVI maps of the selected region of the field with overlayed nozzle lines

lines representing the movement of the irrigation pivot's nozzles were overlaid on maps to visualize how crop parameters were changing at a very fine scale. N1 represents the first nozzle, and N14 represents the 14th nozzle of the pivot section. Descriptive statistics, such as mean value, standard

Table 4.2 Descriptive statistics for the selected small section of the field captured by different imaging platforms

Parameter	Platform	Pixel Count	Range (Min-max)	Mean	Std	Variety	Median
Temperature	UAV	684416	25-66	33.88	3.91	683	34
	Aircraft	2090	26.19-28.8	27.34	0.51	158	27.35
	Satellite	6	28.15-29.14	28.70	0.37	6	28.71
NDVI	UAV	2483285	0-1	0.76	0.12	93	0.78
	Aircraft	3581	0.42-0.81	0.65	0.10	40	0.64
	Satellite	6	0.73-0.79	0.76	0.02	5	0.74

deviation (std), range, and variety of NDVI and temperature values for the selected region, are provided in Table 4.2. The number of pixels used to cover the area by each imaging platform was also provided to interpret the level of detail offered by imagery. The UAV imagery used the maximum number of pixels, with 6,84,416 pixels for thermal and 24,83,285 pixels for multispectral imagery. The aircraft imagery took 2,090 pixels for thermal and 3,581 pixels for multispectral imagery to cover the same area. With a coarser spatial resolution, satellite imagery used only six full pixels to cover a larger area that included the target region. It is important to note that the greater the number of pixels used to image an area, the higher the level of details will be. The UAV imagery covered a wide range of temperatures from 25 to 66 °C, with 683 varieties of temperature values coming from different objects present in the field. The temperature values for the aircraft imagery ranged between 26.19 °C to 28.8 °C with 158 types in values, indicating a lower level of temperature variation. The satellite imagery displayed temperature values only from 28.15 °C to 29.14 °C with just six variations in temperature, which is inadequate for sensing precise

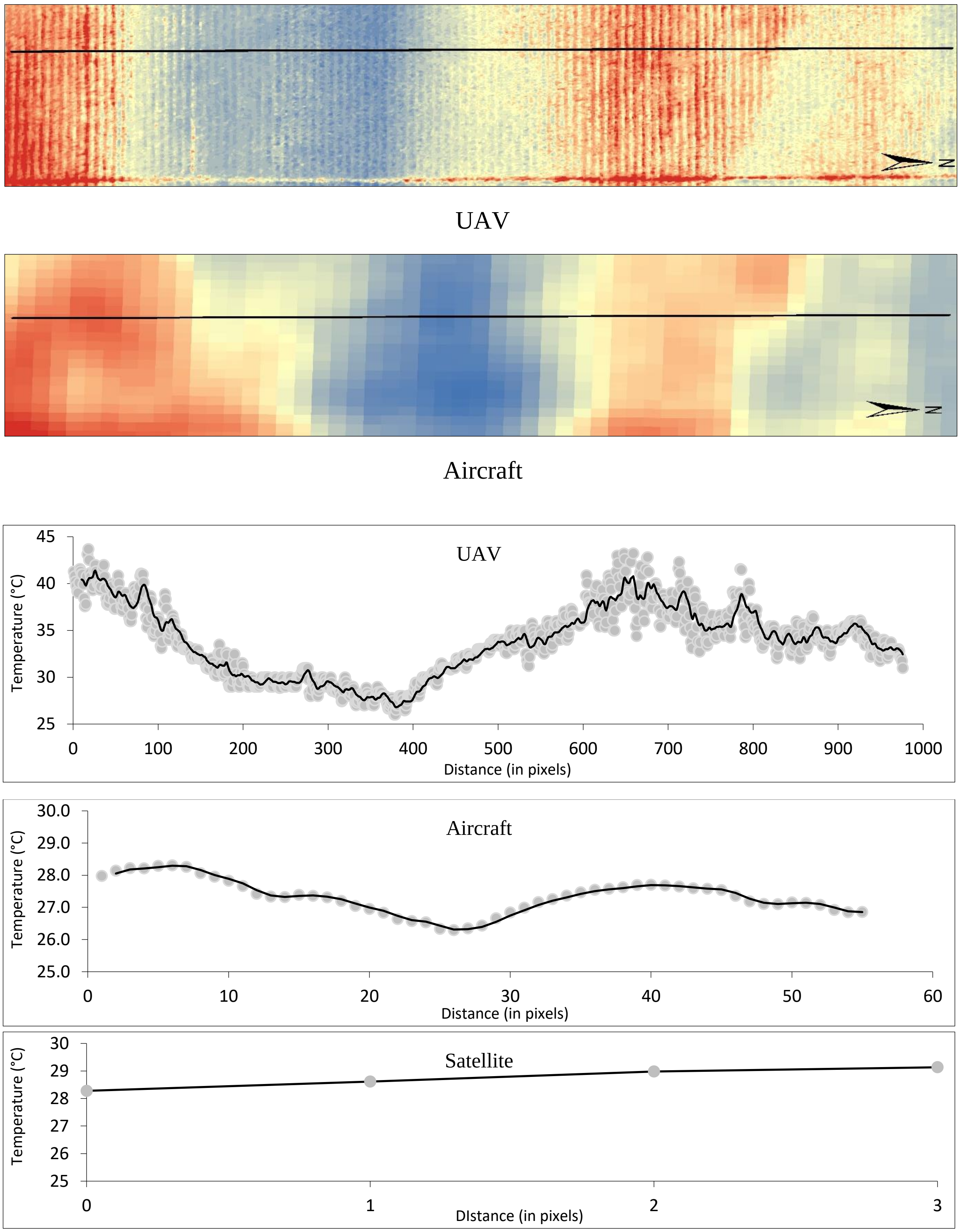

Figure 4.13 Temperature profile graphs from different imaging platforms

crop variability within a field. Similar observations were observed for NDVI, where the UAV provided the largest number of pixels and variety of values, followed by the aircraft and satellite.

A mix of cold and hot regions was noticed when moving from the south edge of the field to the north edge (Figure 4.12). This crop health variability was seen even between two side-by-side nozzles. A transect line parallel to nozzles lines was drawn over the area between nozzles N9 and N10, the black horizontal line in the maps from Figure 4.13. The line was located to pass through well and underperforming plants. Profile graphs showing values of the canopy temperature and distance from starting point of the line in terms of pixels for all imaging platforms were developed along the transect line using 3D-analyst tools from ArcMap. The 3D-analyst tools allow us to query attribute values from orthomosaic corresponding to the pixels along a line (transect line) or polygon. These profile graphs demonstrated the performance of the imaging platforms when transitioning from healthy plants to stressed plants.

The visual inspection across the transect line in Figure 4.13 revealed the presence of four major types of regions. The southern edge of the field was characterized by severely stressed plants, followed by an area of very healthy plants, then a region of stressed plants, and finally, a region of a mix of mildly stressed and healthy plants at the northern edge. The profile graph generated from the UAV imagery accurately illustrated these regions with low and high peaks, and small peaks represented the transitions between these regions. The aircraft imagery was able to detect major changes with smoother and broader peaks. This was due to the larger pixels of aircraft imagery, which recorded the mixed response from the bare soil between the crop rows and plants. The crop rows and gap between rows can be distinguished easily in the UAV imagery but were not separable in the aircraft imagery, resulting in mixed pixels of soil and crop. However, the satellite imagery was not able to differentiate these regions of significantly dissimilar crop health, with the entire transect line being represented by only four values that varied by only 1 °C. This analysis demonstrates that the UAV imaging platform provides the highest level of detail and variation, making it the most suitable platform for assessing crop variability at a very fine scale. The aircraft imagery also turned out as an appropriate choice for detecting significant crop health variations where very fine details are not required. Whereas providing some level of detail, the satellite platform offered limited precision and accuracy in crop variability assessment compared to the UAV and aircraft.

4.5 Conclusion

This study demonstrated the capacity of three remote sensing platforms: UAV, aircraft, and satellite, to detect the infield crop health variability. Spatial maps of canopy temperature and a well-established vegetative index (NDVI) were developed for a four-acre field over two years. UAV imagery outperformed the other two platforms in providing detailed imagery and sensing changes in crop health throughout the field. The UAV imagery provided the highest level of detail, with 6,84,416 pixels and 683 different canopy temperature values and 24,83,285 pixels with 93 different variations in NDVI values, to represent a sample area of dimension 82 m x 44 m. Whereas for the same area, aircraft thermal imagery provided comparatively fewer details with 2,090 pixels and 158 different canopy temperature values and 3,581 pixels with 40 different NDVI values. Satellite imagery was very limited by resolution and presented the same area with only 6 pixels and 5-6 variations in canopy temperature and NDVI values.

Moderate and low spatial resolution imagery from aircraft (1-1.5 m/pixel) and satellite (30 m/pixel) was unable to detect inter-row variability and outputs the average pixels of the crop canopy and inter-row space. Whereas high-resolution UAV imagery (1.5 cm/pixel – 6 cm/pixel) precisely distinguished inter-row gap from plants and provided crop-only pixels without mixing with background soil. Additionally, UAV imagery was very sensitive in sensing minute changes corresponding to the transition between healthy and stressed plants. UAV imagery precisely detected crop variability between two nozzles of an irrigation pivot, which is vital in designing an efficient and precise variable rate irrigation system. Aircraft imagery also successfully provided crop health variations between pivot nozzles but with less precision and sensitivity. Satellite imagery is limited in providing infield crop health variability to design site-specific irrigation, especially for small-scale farms. So, overall, UAV and aircraft imagery remains competitive in providing infield crop health variability for site-specific management in agriculture. UAV imagery is recommended when fine details are required, and aircraft imagery is useful where very fine details can be sacrificed to get better area coverage.

Chapter 5 - Conclusion and Future Work

5.1 Conclusion

The major outcomes of this study were:

1. The appropriate selection of camera focal length and flying altitude can yield consistent and accurate canopy temperature sensing. Canopy temperature maps of crops with a temperature error of less than 2°C from the actual canopy temperature are produced in this study. The reliability of these results is evidenced by consistency in temperature difference values over multiple locations for an individual flight and over a single location for multiple flights. It was also revealed that temperature values extracted from imagery representing crop rows and aisles were not significantly different at the full canopy cover stage (negligible difference of less than 0.5 °C). Hence, one can use temperature values extracted from crop rows or aisles when corn is healthy and at the full canopy cover stage without concern for significant canopy temperature errors.

   With the narrow-angle (large focal length) cameras flying at low altitudes on highly dense and uniform canopy cover, image stitching software was unable to find unique features between overlapping images. This raised complications in the alignment of images, resulting in unacceptable quality orthomosaics. So, users might consider caution when using a narrow-angle thermal camera at low altitudes to extract corn canopy temperatures. The thermal camera with a 13 mm focal length flying at an altitude of 50 m provided orthomosaics that qualified for all parameters needed to develop accurate orthomosaics and extract precise canopy temperature.

2. The capability of high-resolution airborne thermal imagery to detect crop water stress in a corn field comprising three irrigation levels was demonstrated. Location and climate-

specific non-water stress baselines for corn were developed and incorporated in crop water stress index (CWSI) map generation to consider the effect of instant local air temperature and relative humidity on canopy temperature. High-resolution precise crop water stress maps produced in this study were capable of inter-row and intra-row detection of water stress for corn, which can further be used in robust site-specific irrigation management. The vegetative indices significantly explained variation in crop water stress, with NDRE having the highest R^2 values, around 0.8, and NDVI having R^2 values of around 0.7. Crop water stress variations were also supported by field-measured leaf water potential; it significantly affected CWSI and showed a correlation with R^2 values from 0.2 to 0.6 for different datasets. NDRE turned out to be more sensitive to changes in chlorophyll content than NDVI due to the better distinguishing power of the Red-Edge band for chlorophyll content/photosynthesis activity than the red band.

3. The capacity of three remote sensing platforms: UAV, aircraft, and satellite, to detect the infield crop health variability was assessed. UAV imagery outperformed the other two platforms in providing detailed imagery and sensing changes in crop health throughout the field. The UAV imagery provided the highest level of detail, with the highest numbers of pixels and the most variations in canopy temperature and NDVI values. Aircraft imagery provided comparatively fewer details than UAV imagery but was still at an acceptable level of detail. Satellite imagery was limited by resolution and presented insufficient details and variations for detecting infield canopy temperature and NDVI variability.

Moderate and low spatial resolution imagery from aircraft (1-1.5 m/pixel) and satellite (30 m/pixel) was unable to detect inter-row variability and outputs the average pixels of the crop canopy and inter-row space. Whereas high-resolution UAV imagery (1.5

cm/pixel – 6 cm/pixel) precisely distinguished inter-row gap from plants and provided crop-only pixels without mixing with background soil. UAV imagery was the most sensitive and precise in detecting minute changes corresponding to the transition between healthy and stressed plants between two nozzles of an irrigation pivot. This is a vital input to design an efficient and precise variable rate irrigation system. Aircraft imagery also successfully detected these variations between pivot nozzles but with less precision and sensitivity. Satellite imagery was limited in providing infield crop health variability to design site-specific irrigation, especially for small-scale farms.

Overall, UAV and aircraft imagery remains competitive in providing infield crop health variability for site-specific management in agriculture. UAV imagery is recommended when fine details are required, and aircraft imagery is useful where very fine details can be sacrificed to get better area coverage.

In summary, thermal remote sensing with UAV (at low varying altitudes from 30 meters to 70 meters with low, medium, and wide field of view cameras), aircraft, and satellite was explored to quantify plant water stress for corn. It was interesting to see how the coarser spatial resolution thermal maps showed blurry differences or no difference between crop and soil backgrounds, whereas fine-resolution imagery successfully demonstrated distinct differences. High-resolution precise crop water stress maps (considering local environmental effects) produced in this study were capable of inter-row and intra-row detection of water stress for corn, which can further be used in robust site-specific irrigation management. The spatial resolution and spectral discrimination-based assessment provided a deep insight into selecting the appropriate remote sensing platform and altitude for producing high-quality thermal imagery and precise canopy temperature sensing.

5.2 Future work recommendations

Further investigations may consider modeling the amount of water required (in inches) for an agricultural field using crop water stress maps and ground-based soil moisture monitoring. Assessment of irrigation water used in crop water stress map-based site-specific irrigation in contrast to uniform irrigation can provide critical insights for better irrigation water management. A higher-resolution thermal camera development is also required, which can be used on manned planes to enhance operational efficiencies and capture higher spatial resolution imagery to develop and implement precision irrigation management decisions.

References

Alves, I., & Pereira, L. S. (2000). Non-water-stressed baselines for irrigation scheduling with infrared thermometers: A new approach. *Irrigation Science*, 19(2), 101–106. https://doi.org/10.1007/s002710050007

Anderson, S. L., Murray, S. C., Malambo, L., Ratcliff, C., Popescu, S., Cope, D., Chang, A., Jung, J., & Thomasson, J. A. (2019). Prediction of maize grain yield before maturity using improved temporal height estimates of unmanned aerial systems. *The Plant Phenome Journal*, 2(1), 1–15. https://doi.org/10.2135/tppj2019.02.0004

Awais, M., Li, W., Cheema, M. J. M., Hussain, S., Shaheen, A., Aslam, B., Liu, C., & Ali, A. (2022a). Assessment of optimal flying height and timing using high-resolution unmanned aerial vehicle images in precision agriculture. *International Journal of Environmental Science and Technology*, 19(4), 2703–2720. https://doi.org/10.1007/s13762-021-03195-4

Awais, M., Li, W., Hussain, S., Cheema, M. J. M., Li, W., Song, R., & Liu, C. (2022b). Comparative evaluation of land surface temperature images from unmanned aerial vehicle and satellite observation for agricultural areas using in situ data. *Agriculture*, 12(2), 184. https://doi.org/10.3390/agriculture12020184

Baluja, J., Diago, M. P., Balda, P., Zorer, R., Meggio F., Morales, F. & Tardaguila J. (2012). Assessment of vineyard water status variability by thermal and multispectral imagery using an unmanned aerial vehicle (UAV). *Irrigation Science* 30: 511-522.

Barzin, R., Pathak,R., Lotfi H., Varco, J. and Bora G. C. (2020). Use of UAS Multispectral Imagery at Different Physiological Stages for Yield Prediction and Input Resource Optimization in Corn. *Remote Sensing*: Vol 12, Issue 15, P 2392.

Bellvert, J., Marsal, J., Girona, J., & Zarco-Tejada, P. J. (2015). Seasonal evolution of crop water stress index in grapevine varieties determined with high-resolution remote sensing thermal imagery. *Irrigation Science*, 33(2), 81–93. https://doi.org/10.1007/s00271-014-0456-y

Bellvert, J., Zarco-Tejada, P. J., Girona, J., & Fereres, E. (2014). Mapping crop water stress index in a 'Pinot-noir' vineyard: Comparing ground measurements with thermal remote sensing imagery from an unmanned aerial vehicle. *Precision Agriculture*, 15(4), 361–376. https://doi.org/10.1007/s11119-013-9334-5

Berger, K., Verrelst, J., Féret, J.-B., Wang, Z., Wocher, M., Strathmann, M., Danner, M., Mauser, W., & Hank, T. (2020). Crop nitrogen monitoring: Recent progress and principal developments in the context of imaging spectroscopy missions. *Remote Sensing of Environment*, 242, 111758. https://doi.org/10.1016/j.rse.2020.111758

Berni, J. A. J., Zarco-Tejada, P. J., Sepulcre-Cantó, G., Fereres, E., & Villalobos, F. (2009a). Mapping canopy conductance and CWSI in olive orchards using high resolution thermal remote sensing imagery. *Remote Sensing of Environment*, 113(11), 2380–2388. https://doi.org/10.1016/j.rse.2009.06.018

Berni, J. A. J., Zarco-Tejada, P. J., Suarez, L., Fereres, E. (2009b). Thermal and Narrowband Multispectral Remote Sensing for Vegetation Monitoring From an Unmanned Aerial Vehicle. *IEEE Transactions on Geoscience and Remote Sensing*: 722-38.

Bian, J., Zhang, Z., Chen, J., Chen, H., Cui, C., Li, X., Chen, S., & Fu, Q. (2019). Simplified evaluation of cotton water stress using high resolution unmanned aerial vehicle thermal imagery. *Remote Sensing*, 11(3), 267.

Bosecker R. R. (1988). Sampling methods in agriculture; National agricultural Statistics Service., US Department of Agriculture. Washington, DC, USA.

Brewer, K., Clulow, A., Sibanda, M., Gokool, S., Odindi, J., Mutanga, O., Naiken, V., Chimonyo, V. G. P., & Mabhaudhi, T. (2022). Estimation of maize foliar temperature and stomatal conductance as indicators of water stress based on optical and thermal imagery acquired using an unmanned aerial vehicle (Uav) platform. *Drones*, 6(7), 169. https://doi.org/10.3390/drones6070169

Campos-Taberner, M., García-Haro, F., Busetto, L., Ranghetti, L., Martínez, B., Gilabert, M. A., Camps-Valls, G., Camacho, F., & Boschetti, M. (2018). A critical comparison of remote sensing leaf area index estimates over rice-cultivated areas: From sentinel-2 and landsat-7/8 to modis, geov1 and eumetsat polar system. *Remote Sensing*, 10(5), 763. https://doi.org/10.3390/rs10050763

Chen, J., Lin, L., & Lü, G. (2010). An index of soil drought intensity and degree: An application on corn and a comparison with CWSI. *Agricultural Water Management*, 97(6), 865–871. https://doi.org/10.1016/j.agwat.2010.01.017

Cohen, Y., Alchanatis, V., Meron, M., Saranga, Y., & Tsipris, J. (2005). Estimation of leaf water potential by thermal imagery and spatial analysis*. *Journal of Experimental Botany*, 56(417), 1843–1852. https://doi.org/10.1093/jxb/eri174

Cohen, Y., Alchanatis, V., Sela, E., Saranga, Y., Cohen, S., Meron, M., Bosak, A., Tsipris, J., Ostrovsky, V., Orolov, V., Levi, A., & Brikman, R. (2015). Crop water status estimation using thermography: Multi-year model development using ground-based thermal images. *Precision Agriculture*, 16(3), 311–329. https://doi.org/10.1007/s11119-014-9378-1

Comba, L., Biglia, A., Ricauda Aimonino, D., Tortia, C., Mania, E., Guidoni, S., & Gay, P. (2020). Leaf Area Index evaluation in vineyards using 3D point clouds from UAV imagery. *Precision Agriculture*, 21(4), 881–896. https://doi.org/10.1007/s11119-019-09699-x

Crusiol, L. G. T., Nanni, M. R., Furlanetto, R. H., Sibaldelli, R. N. R., Cezar, E., Mertz-Henning, L. M., Nepomuceno, A. L., Neumaier, N., & Farias, J. R. B. (2020). UAV-based thermal imaging in the assessment of water status of soybean plants. *International Journal of Remote Sensing*, 41(9), 3243–3265. https://doi.org/10.1080/01431161.2019.1673914

Deilami, K., Kamruzzaman, Md., & Liu, Y. (2018). Urban heat island effect: A systematic review of spatio-temporal factors, data, methods, and mitigation measures. *International Journal of Applied Earth Observation and Geoinformation*, 67, 30–42. https://doi.org/10.1016/j.jag.2017.12.009

Dwyer, J. L., Roy, D. P., Sauer, B., Jenkerson, C. B., Zhang, H. K., & Lymburner, L. (2018). Analysis ready data: Enabling analysis of the landsat archive. *Remote Sensing*, 10(9), 1363. https://doi.org/10.3390/rs10091363

Ehrler, W. L., Idso, S. B., Jackson, R. D., & Reginato, R. J. (1978). Wheat canopy temperature: Relation to plant water potential 1. *Agronomy Journal*, 70(2), 251–256. https://doi.org/10.2134/agronj1978.00021962007000020010x

Erdem, Y., Arin, L., Erdem, T., Polat, S., Deveci, M., Okursoy, H., & Gültaş, H. T. (2010). Crop water stress index for assessing irrigation scheduling of drip irrigated broccoli (Brassica oleracea L. var. Italica). *Agricultural Water Management*, 98(1), 148–156. https://doi.org/10.1016/j.agwat.2010.08.013

Farm and Ranch Irrigation Survey (FRIS) 2018. (2018). https://www.nass.usda.gov/Publications/AgCensus/2017/Online_Resources/Farm_and_Ranch_Irrigation_Survey/index.php

Fereres, E., & Evans, R. G. (2006). Irrigation of fruit trees and vines: An introduction. *Irrigation Science*, 24(2), 55–57. https://doi.org/10.1007/s00271-005-0019-3

G. Poley, L., & J. McDermid, G. (2020). A systematic review of the factors influencing the estimation of vegetation aboveground biomass using unmanned aerial systems. *Remote Sensing*, 12(7), 1052. https://doi.org/10.3390/rs12071052

Gadhwal, M., Sangha, H. S., Sharda, A., & Merwe, D. van der. (2022). Spatial corn canopy temperature extraction: How focal length and suas flying altitude influence thermal infrared sensing accuracy. *SSRN Electronic Journal*. https://doi.org/10.2139/ssrn.4166490

Gebbers, R., Adamchuk, V. (2010). "Precision Agriculture and Food Security. Science327(5967)." Science (New York, N.Y.): 828-31.

Gerhards, M., Schlerf, M., Mallick, K., & Udelhoven, T. (2019). Challenges and future perspectives of multi-/hyperspectral thermal infrared remote sensing for crop water-stress detection: A review. *Remote Sensing*, 11(10), 1240. https://doi.org/10.3390/rs11101240

Gevaert, C. M., & García-Haro, F. J. (2015). A comparison of STARFM and an unmixing-based algorithm for Landsat and MODIS data fusion. *Remote Sensing of Environment*, 156, 34–44. https://doi.org/10.1016/j.rse.2014.09.012

Gidey, E., Dikinya, O., Sebego, R., Segosebe, E., & Zenebe, A. (2018). Analysis of the long-term agricultural drought onset, cessation, duration, frequency, severity and spatial extent using Vegetation Health Index (Vhi) in Raya and its environs, Northern Ethiopia. *Environmental Systems Research*, 7(1), 13. https://doi.org/10.1186/s40068-018-0115-z

Giménez-Gallego, J., González-Teruel, J. D., Soto-Valles, F., Jiménez-Buendía, M., Navarro-Hellín, H., & Torres-Sánchez, R. (2021). Intelligent thermal image-based sensor for affordable measurement of crop canopy temperature. *Computers and Electronics in Agriculture*, 188, 106319.

Gómez-Candón, D., Virlet, N., Labbé, S., Jolivot, A., & Regnard, J.-L. (2016). Field phenotyping of water stress at tree scale by UAV-sensed imagery: New insights for thermal acquisition and calibration. *Precision Agriculture*, 17(6), 786–800. https://doi.org/10.1007/s11119-016-9449-6

Gonzalez-Dugo, V., Zarco-Tejada, P. J., & Fereres, E. (2014). Applicability and limitations of using the crop water stress index as an indicator of water deficits in citrus orchards. *Agricultural and Forest Meteorology*, 198–199, 94–104. https://doi.org/10.1016/j.agrformet.2014.08.003

Han, M., Zhang, H. H., DeJonge, K. C., Comas, L. H., Gleason, S. (2018). Comparison of three crop water stress index models with sap flow measurements in maize. *Agricultural Water Management* 203: 366–375.

Han, X., Thomasson, J. A., Bagnall, G. C., Pugh, N. A., Horne, D. W., Rooney, W. L., Jung, J., Chang, A., Malambo, L., Popescu, S. C., Gates, I. T., & Cope, D. A. (2018). Measurement and calibration of plant-height from fixed-wing uav images. *Sensors*, 18(12), 4092. https://doi.org/10.3390/s18124092

Han, X., Thomasson, J. A., Swaminathan, V., Wang, T., Siegfried, J., Raman, R., Rajan, N., & Neely, H. (2020). Field-based calibration of unmanned aerial vehicle thermal infrared imagery with temperature-controlled references. *Sensors*, 20(24), 7098. https://doi.org/10.3390/s20247098

Han, Y., Tarakey, B. A., Hong, S.-J., Kim, S.-Y., Kim, E., Lee, C.-H., & Kim, G. (2021). Calibration and image processing of aerial thermal image for uav application in crop water stress estimation. *Journal of Sensors*, 2021, 1–14. https://doi.org/10.1155/2021/5537795

Heilman, J. L., Kanemasu, E. T., Rosenberg, N. J., & Blad, B. L. (1976). Thermal scanner measurement of canopy temperatures to estimate evapotranspiration. *Remote Sensing of Environment*, 5, 137–145. https://doi.org/10.1016/0034-4257(76)90044-4

Hussain, S., Gao, K., Din, M., Gao, Y., Shi, Z., & Wang, S. (2020). Assessment of uav-onboard multispectral sensor for non-destructive site-specific rapeseed crop phenotype variable at different phenological stages and resolutions. *Remote Sensing*, 12(3), 397. https://doi.org/10.3390/rs12030397

Idso, S. B., Jackson, R. D., Pinter, P. J., Reginato, R. J., & Hatfield, J. L. (1981). Normalizing the stress-degree-day parameter for environmental variability. *Agricultural Meteorology*, 24, 45–55. https://doi.org/10.1016/0002-1571(81)90032-7

Irmak, S., Haman, D. Z., & Bastug, R. (2000). Determination of crop water stress index for irrigation timing and yield estimation of corn. *Agronomy Journal*, 92(6), 1221–1227. https://doi.org/10.2134/agronj2000.9261221x

Jackson, R. D., Idso, S. B., Reginato, R. J., & Pinter, P. J. (1981). Canopy temperature as a crop water stress indicator. *Water Resources Research*, 17(4), 1133–1138. https://doi.org/10.1029/WR017i004p01133

Jaganmohan, M., Knapp, S., Buchmann, C. M., & Schwarz, N. (2016). The bigger, the better? The influence of urban green space design on cooling effects for residential areas. *Journal of Environmental Quality*, 45(1), 134–145. https://doi.org/10.2134/jeq2015.01.0062

Jones, H. G. (1999). Use of infrared thermometry for estimation of stomatal conductance as a possible aid to irrigation scheduling. *Agricultural and Forest Meteorology*, 95(3), 139–149. https://doi.org/10.1016/S0168-1923(99)00030-1

Jones, H. G. (2002). Use of infrared thermography for monitoring stomatal closure in the field: Application to grapevine. *Journal of Experimental Botany*, 53(378), 2249–2260. https://doi.org/10.1093/jxb/erf083

Jones, H.G. (2014). Remote sensing of plant stresses and its use in irrigation management. In M. Stoll, J. Zinkernagel, & P. Braun (Eds.), VII International Symposium on Irrigation of Horticultural Crops (pp. 239-247). Geisenheim, Germany: Int Soc Horticultural Science.

Jones, J. W., Antle, J. M., Basso, B., Boote, K. J., Conant, R. T., Foster, I., Godfray, H. C. J., Herrero, M., Howitt, R. E., Janssen, S., Keating, B. A., Munoz-Carpena, R., Porter, C. H., Rosenzweig, C., & Wheeler, T. R. (2017). Brief history of agricultural systems modeling. *Agricultural Systems*, 155, 240–254. https://doi.org/10.1016/j.agsy.2016.05.014

Kang, D.-I., Moon, H.-G., Sung, S.-Y., & Cha, J.-G. (2018). Applicability of uav in urban thermal environment analysis. *Journal of the Korean Institute of Landscape Architecture*, 46(2), 52–61. https://doi.org/10.9715/KILA.2018.46.2.052

Kar, G., & Kumar, A. (2010). Energy balance and crop water stress in winter maize under phenology-based irrigation scheduling. *Irrigation Science*, 28(3), 211–220. https://doi.org/10.1007/s00271-009-0192-x

Khanal, S., Fulton J., & Shearer, S. (2017). An overview of current and potential applications of thermal remote sensing in precision agriculture. *Computers and Electronics in Agriculture*, 135, 22–32. https://doi.org/10.1016/j.compag.2017.01.011

Kraaijenbrink, P. D. A., Shea, J. M., Litt, M., Steiner, J. F., Treichler, D., Koch, I., & Immerzeel, W. W. (2018). Mapping surface temperatures on a debris-covered glacier with an unmanned aerial vehicle. *Frontiers in Earth Science*, 6, 64. https://doi.org/10.3389/feart.2018.00064

Krishna, G., Sahoo, R. N., Singh, P., Patra, H., Bajpai, V., Das, B., Kumar, S., Dhandapani, R., Vishwakarma, C., Pal, M., & Chinnusamy, V. (2021). Application of thermal imaging and hyperspectral remote sensing for crop water deficit stress monitoring. *Geocarto International*, 36(5), 481–498. https://doi.org/10.1080

Li, L., Nielsen, D. C., Yu, Q., Ma, L., & Ahuja, L. R. (2010). Evaluating the Crop Water Stress Index and its correlation with latent heat and CO2 fluxes over winter wheat and maize in the North China plain. *Agricultural Water Management*, 97(8), 1146–1155. https://doi.org/10.1016/j.agwat.2008.09.015

Li, M., Shamshiri, R. R., Weltzien, C., & Schirrmann, M. (2022). Crop monitoring using sentinel-2 and UAV multispectral imagery: A comparison case study in northeastern Germany. *Remote Sensing*, 14(17), 4426. https://doi.org/10.3390/rs14174426

Ludovisi, R., Tauro, F., Salvati, R., Khoury, S., Mugnozza Scarascia, G., & Harfouche, A. (2017). UAV-based thermal imaging for high-throughput field phenotyping of black poplar response to drought. *Frontiers in Plant Science*, 8, 1681. https://doi.org/10.3389/fpls.2017.01681

Mangus, D. L., Sharda, A., & Zhang, N. (2016). Development and evaluation of thermal infrared imaging system for high spatial and temporal resolution crop water stress monitoring of corn within a greenhouse. *Computers and Electronics in Agriculture*, 121, 149–159. https://doi.org/10.1016/j.compag.2015.12.007

Matese, A., Toscano, P., Di Gennaro, S., Genesio, L., Vaccari, F., Primicerio, J., Belli, C., Zaldei, A., Bianconi, R., & Gioli, B. (2015). Intercomparison of UAV, aircraft and satellite remote sensing platforms for precision viticulture. *Remote Sensing*, 7(3), 2971–2990. https://doi.org/10.3390/rs70302971

Meron, M., Sprintsin, M., Tsipris, J., Alchanatis, V., & Cohen, Y. (2013). Foliage temperature extraction from thermal imagery for crop water stress determination. *Precision Agriculture*, 14(5), 467–477.

Messina, G., Peña, J. M., Vizzari, M., & Modica, G. (2020). A comparison of UAV and satellites multispectral imagery in monitoring onion crop. An application in the 'Cipolla Rossa di Tropea' (Italy). *Remote Sensing*, 12(20), 3424. https://doi.org/10.3390/rs12203424

Metternicht, G. (2008). Remote sensing. In K. K. Kemp (Ed.), Encyclopedia of Geographic Information Science (pp. 365–368). Sage Publication.

Moller, M., Alchanatis, V., Cohen, Y., Meron, M., Tsipris, J., Naor, A., Ostrovsky, V., Sprintsin, M., & Cohen, S. (2006). Use of thermal and visible imagery for estimating crop water status of irrigated grapevine. *Journal of Experimental Botany*, 58(4), 827–838. https://doi.org/10.1093/jxb/erl115

Mulla, D. J. (2013). Twenty five years of remote sensing in precision agriculture: Key advances and remaining knowledge gaps.

Ndlovu, H. S., Odindi, J., Sibanda, M., Mutanga, O., Clulow, A., Chimonyo, V. G. P., & Mabhaudhi, T. (2021). A comparative estimation of maize leaf water content using machine learning techniques and unmanned aerial vehicle (Uav)-based proximal and remotely sensed data. *Remote Sensing*, 13(20), 4091. https://doi.org/10.3390/rs13204091

Ndre index: Vegetation analysis for mid and late season crops. (2019, September 25). https://eos.com/industries/agriculture/ndre/

Nebikera, S., Annena, A., Scherrerb, M., & Oesch, D. (2008). A light-weight multispectral sensor for micro UAV – opportunities for very high resolution airborne remote sensing. The International Archives of the Photogrammetry, Remote Sensing and Spatial Information Sciences.

Payero, J. O., & Irmak, S. (2006). Variable upper and lower crop water stress index baselines for corn and soybean. *Irrigation Science*, 25(1), 21–32. https://doi.org/10.1007/s00271-006-0031-2

Peñuelas, J., Filella, I., Biel, C., Serrano, L., & Savé, R. (1993). The reflectance at the 950–970 nm region as an indicator of plant water status. *International Journal of Remote Sensing*, 14(10), 1887–1905. https://doi.org/10.1080/01431169308954010

Pineda, M., Barón, M., & Pérez-Bueno, M.-L. (2020). Thermal imaging for plant stress detection and phenotyping. *Remote Sensing*, 13(1), 68. https://doi.org/10.3390/rs13010068

Pou, A., Diago, M. P., Medrano, H., Baluja, J., & Tardaguila, J. (2014). Validation of thermal indices for water status identification in grapevine. *Agricultural Water Management*, 134, 60–72. https://doi.org/10.1016/j.agwat.2013.11.010

Ren, J., Shao, Y., Wan, H., Xie, Y., & Campos, A. (2021). A two-step mapping of irrigated corn with multi-temporal MODIS and Landsat analysis ready data. *ISPRS Journal of*

Photogrammetry and Remote Sensing, 176, 69–82. https://doi.org/10.1016/j.isprsjprs.2021.04.007

Sagan, V., Maimaitijiang, M., Sidike, P., Eblimit, K., Peterson, K., Hartling, S., Esposito, F., Khanal, K., Newcomb, M., Pauli, D., Ward, R., Fritschi, F., Shakoor, N., & Mockler, T. (2019). Uav-based high resolution thermal imaging for vegetation monitoring, and plant phenotyping using ici 8640 p, flir vue pro r 640, and thermomap cameras. *Remote Sensing*, 11(3), 330.

Sangha, H. S., Sharda, A., Koch, L., Prabhakar, P., & Wang, G. (2020). Impact of camera focal length and sUAS flying altitude on spatial crop canopy temperature evaluation. *Computers and Electronics in Agriculture*, *172*, 105344. https://doi.org/10.1016/j.compag.2020.105344

Segarra, J., Buchaillot, M. L., Araus, J. L., & Kefauver, S. C. (2020). Remote sensing for precision agriculture: Sentinel-2 improved features and applications. *Agronomy*, 10(5), 641. https://doi.org/10.3390/agronomy10050641

Sepulcre-Cantó, G., Zarco-Tejada, P. J., Jiménez-Muñoz, J. C., Sobrino, J. A., Miguel, E. de, & Villalobos, F. J. (2006). Detection of water stress in an olive orchard with thermal remote sensing imagery. *Agricultural and Forest Meteorology*, 136(1–2), 31–44. https://doi.org/10.1016/j.agrformet.2006.01.008

Shi, Y., Thomasson, J. A., Murray, S. C., Pugh, N. A., Rooney, W. L., Shafian, S., Rajan, N., Rouze, G., Morgan, C. L. S., Neely, H. L., Rana, A., Bagavathiannan, M. V., Henrickson, J., Bowden, E., Valasek, J., Olsenholler, J., Bishop, M. P., Sheridan, R., Putman, E. B., … Yang, C. (2016). Unmanned aerial vehicles for high-throughput phenotyping and agronomic research. *PLOS ONE*, 11(7), e0159781. https://doi.org/10.1371/journal.pone.0159781

Sibanda, M., Onisimo, M., Dube, T., & Mabhaudhi, T. (2021). Quantitative assessment of grassland foliar moisture parameters as an inference on rangeland condition in the mesic rangelands of southern Africa. *International Journal of Remote Sensing*, 42(4), 1474–1491. https://doi.org/10.1080/01431161.2020.1832282

Taghvaeian, S., Chávez, J., & Hansen, N. (2012). Infrared thermometry to estimate crop water stress index and water use of irrigated maize in northeastern Colorado. *Remote Sensing*, 4(11), 3619–3637. https://doi.org/10.3390/rs4113619

Taghvaeian, S., Comas, L., DeJonge, K. C., & Trout, T. J. (2014). Conventional and simplified canopy temperature indices predict water stress in sunflower. *Agricultural Water Management*, 144, 69–80. https://doi.org/10.1016/j.agwat.2014.06.003

Ten Harkel, J., Bartholomeus, H., & Kooistra, L. (2019). Biomass and crop height estimation of different crops using UAV-based lidar. *Remote Sensing*, 12(1), 17. https://doi.org/10.3390/rs12010017

Thomson, S. J., Ouellet-Plamondon, C. M., DeFauw, S. L., Huang, Y., Fisher, D. K., & English, P. J. (2012). Potential and challenges in use of thermal imaging for humid region irrigation system management. *Journal of Agricultural Science*, 4

Turner, D., Lucieer, A., Malenovský, Z., King, D. H., Robinson, S. A. (2014). Spatial Co-Registration of Ultra-High Resolution Visible, Multispectral and Thermal Images Acquired with a Micro-UAV over Antarctic Moss Beds. *Remote Sensing*, 6(5), 4003-4024. https://doi.org/10.3390/rs6054003

Turner, N., & Long, M. (1980). Errors arising from rapid water loss in the measurement of leaf water potential by the pressure chamber technique. *Functional Plant Biology*, 7(5), 527. https://doi.org/10.1071/PP9800527

U.S. Geological Survey. (2018). U.S. Landsat Analysis Ready Data: U.S. Geological Survey Fact Sheet 2018–3053, 2 p. https://doi.org/10.3133/fs20183053

Wanjura, D. F., Upchurch, D. R., & Mahan, J. R. (2006). Behavior of temperature-based water stress indicators in BIOTIC-controlled irrigation. *Irrigation Science,* 24(4), 223-232. https://doi.org/10.1007/s00271-005-0021-9

Webster, C., Westoby, M., Rutter, N., & Jonas, T. (2018). Three-dimensional thermal characterization of forest canopies using UAV photogrammetry. *Remote Sensing of Environment*, 209, 835-847. https://doi.org/10.1016/j.rse.2017.09.033

White, J. W., Andrade-Sanchez, P., Gore, M. A., Bronson, K. F., Coffelt, T. A., Conley, M. M., Feldmann, K. A., French, A. N., Heun, J. T., Hunsaker, D. J., Jenks, M. A., Kimball, B. A., Roth, R. L., Strand, R. J., Thorp, K. R., Wall, G. W., & Wang, G. (2012). Field-based phenomics for plant genetics research. *Field Crops Research*, 133, 101-112. https://doi.org/10.1016/j.fcr.2012.04.003

Xu, C., Qu, J. J., Hao, X., Cosh, M. H., Zhu, Z., & Gutenberg, L. (2020). Monitoring crop water content for corn and soybean fields through data fusion of MODIS and Landsat measurements in Iowa. *Agricultural Water Management*, 227, 105844. https://doi.org/10.1016/j.agwat.2019.105844

Yang, C., He, X., Yu, L., Yang, J., Yan, F., Bu, K., Chang, L., & Zhang, S. (2017). The cooling effect of urban parks and its monthly variations in a snow climate city. *Remote Sensing*, 9(10), 1066. https://doi.org/10.3390/rs9101066

Zarco-Tejada, P. J., González-Dugo, V., Williams, L. E., Suárez, L., Berni, J. A. J., Goldhamer, D., & Fereres, E. (2013a). A PRI-based water stress index combining structural and chlorophyll effects: Assessment using diurnal narrow-band airborne imagery and the CWSI thermal index. *Remote Sensing of Environment*, 138, 38–50. https://doi.org/10.1016/j.rse.2013.07.024

Zarco-Tejada, P. J., Suarez, L., & Gonzalez-Dugo, V. (2013b). Spatial resolution effects on chlorophyll fluorescence retrieval in a heterogeneous canopy using hyperspectral imagery and radiative transfer simulation. *IEEE Geoscience and Remote Sensing Letters*, 10(4), 937–941. https://doi.org/10.1109/LGRS.2013.2252877

Zhang, L., Niu, Y., Zhang, H., Han, W., Li, G., Tang, J., & Peng, X. (2019a). Maize canopy temperature extracted from UAV thermal and RGB imagery and its application in water stress monitoring. *Frontiers in Plant Science*, 10, 1270. https://doi.org/10.3389/fpls.2019.01270

Zhang, L., Zhang, H., Niu, Y., & Han, W. (2019b). Mapping maize water stress based on UAV multispectral remote sensing. *Remote Sensing*, 11(6), 605. https://doi.org/10.3390/rs11060605

Zhang, Y., Han, W., Zhang, H., Niu, X., & Shao, G. (2023). Evaluating maize evapotranspiration using high-resolution UAV-based imagery and FAO-56 dual crop coefficient approach. *Agricultural Water Management*, 275, 108004. https://doi.org/10.1016/j.agwat.2022.108004

Zhang, Z., Bian, J., Han, W., Fu, Q., Chen, S., & Cui, T. (2018). Diagnosis of cotton water stress using unmanned aerial vehicle thermal infrared remote sensing after removing soil. *Transactions of the Chinese Society for Agricultural Machinery*, 49(10), 250-260.

Zhou, Z., Majeed, Y., Diverres Naranjo, G., & Gambacorta, E. M. T. (2021). Assessment for crop water stress with infrared thermal imagery in precision agriculture: A review and future prospects for deep learning applications. *Computers and Electronics in Agriculture*, 182, 106019. https://doi.org/10.1016/j.compag.2020.106019

Zhu, Z. (2019). Science of landsat analysis ready data. *Remote Sensing*, 11(18), 2166. https://doi.org/10.3390/rs11182166

Zia, S., Romano, G., Spreer, W., Sanchez, C., Cairns, J., Araus, J. L., & Müller, J. (2013). Infrared thermal imaging as a rapid tool for identifying water-stress tolerant maize genotypes of different phenology. *Journal of Agronomy and Crop Science*, 199(2), 75-84. https://doi.org/10.1111/j.1439-037X.2012.00537.x

Ziliani, M., Parkes, S., Hoteit, I., & McCabe, M. (2018). Intra-season crop height variability at commercial farm scales using a fixed-wing UAV. *Remote Sensing*, 10(12), 2007. https://doi.org/10.3390/rs10122007

Appendix A - UAV and Imaging Sensors

UAV

Model	Dji Matrice 100	
Weight (with TB48D battery)	2431 g	
Max. Takeoff Weight	3600 g	
Battery Compartment Weight	160 g	
Max. Speed of Ascent	5 m/s	
Max. Speed of Descent	4 m/s	
Max. Wind Resistance	10 m/s	
Max. Speed	22 m/s (ATTI mode, no payload, no wind) 17 m/s (GPS mode, no payload, no wind)	
Hovering Time (with TB48D battery)	No payload: 28 min; 500g payload: 20 min;1kg payload: 16 min	
Hovering Time (with two TB48D battery)	No payload: 40 min	
Battery	Name	Intelligent Flight Battery
	Model	TB48D
	Capacity	5700 mAh
	Voltage	22.8 V
	Type	LiPo 6S
	Energy	129.96 Wh
	Net Weight	676 g
	Charging Temperature	0°C to 40°C
	Max. Charging Power	180 W

Thermal camera: Flir vue pro

CONNECT IONS & COMMUNICATIONS	
Analog Video Output	Yes
ELECTRICAL	
Input Voltage	4.8-6.0 VDC
Power Dissipation [peak]	2.1 W (3.9 W)
ENVIRONMENTAL & APPROVALS	
Operating Temperature Range -	20°C to +50°C
Operational Altitude	+40,000 feet
IMAGING & OPT ICAL	
Color Palettes	Yes – Adjustable in App and via PWM
Frame Rate	30 Hz (NTSC); 25 Hz (PAL)
HDMI Output	1280x720 @ 50hz, 60hz
Image Optimization	Yes
Invertable Image	Yes - Adjustable in App
IR Camera Resolution	640 x 512
Lens	13 mm; 25° × 19°
Lens Options [FOV for NTSC Analog Output]	13 mm; 24° × 18°
Scene Presets & Image Processing	Yes - Adjustable in App
Spectral Band	7.5 - 13.5 µm
Thermal Imager	Uncooled VOx Microbolometer
MECHANICAL	
Precision Mounting Holes	Two M2x0.4, One 1/4-20 threaded hole on top
Size	2.26" x 1.75" (including lens)
Weight	3.25 - 4 oz (Con�guration Dependant)
Zoom	Yes – Adjustable in App and via PWM
OPT IONAL POWER & HDMI VIDEO MODULE	
Input Power Range	5 VDC – 28 VDC
Reverse Polarity Protection	Yes
RADIOMETRY	
Radiometric Accuracy	+/-5°C or 5% of reading

Multispectral camera: Micasense Red Edge-M

Weight:	231.9 g (8.18 oz.) (includes DLS 2 and cables)
Dimensions:	8.7cm x 5.9cm x 4.54cm (3.4in x 2.3in x 1.8in)
External Power:	4.2 V DC - 15.8 V DC 4 W nominal, 8 W peak
Spectral Bands:	Blue, green, red, red edge, near-IR (global shutter, narrowband)
Wavelength (nm):	Blue (475 nm center ± 20 nm), green (560 nm ± 20 nm), red (668 nm center ± 10 nm), red edge (717 nm ± 10 nm), near-IR (840 nm ± 40 nm)
RGB Color Output:	Global shutter, aligned with all bands
Ground Sample Distance (GSD):	8 cm per pixel (per band) at 120 m (~400 ft) AGL
Capture Rate:	1 capture per second (all bands), 12-bit RAW
Interfaces:	Serial, 10/100/1000 ethernet, removable Wi-Fi, external trigger, GPS, SDHC
Field of View:	47.2° HFOV
Triggering Options:	Timer mode, overlap mode, external trigger mode (PWM, GPIO, serial, and Ethernet options), manual capture mode